



Max-Planck-Institut für Intelligente Systeme
(ehemals Max-Planck-Institut für Metallforschung)
Stuttgart

**Nitriding of iron-based binary and ternary alloys:
microstructural development during nitride
precipitation**

Sai Ramudu Meka

Dissertation
an der
Universität Stuttgart

Bericht Nr. 239
November 2011

**Nitriding of iron-based binary and ternary alloys:
microstructural development during nitride precipitation**

von der Fakultät Chemie der Universität Stuttgart
zur Erlangung der Würde eines Doktors der
Naturwissenschaften (Dr. rer. nat.) genehmigte Abhandlung

vorgelegt von

Sai Ramudu Meka

aus Kuntoji (Gangavathi)/ Indien

Hauptberichter: Prof. Dr. Ir. E. J. Mittemeijer

Mitberichter: Prof. Dr. J. Bill

Prüfungsvorsitzender: Prof. Dr. E. Roduner

Tag der Einreichung: 01.09.2011

Tag der mündlichen Prüfung: 17.11.2011

MAX-PLANCK-INSTITUT FÜR INTELLIGENTE SYSTEME, STUTTGART
(ehemals MAX-PLANCK-INSTITUT FÜR METALLFORSCHUNG)
INSTITUT FÜR MATERIALWISSENSCHAFT DER UNIVERSITÄT STUTTGART

Contents

1 Introduction	7
1.1 Gaseous nitriding - thermodynamics	8
1.2 Microstructure of nitrided zone	9
1.3 Alloying element nitrides in the ferrite matrix.....	11
1.4 Excess nitrogen	13
1.5 Development of iron-nitride compound layers on pure iron.....	14
1.6 Development of iron-nitride compound layers on iron-based alloys.....	15
1.7 Pore formation in the nitrided zone: metastable nature of the Fe-N phases	16
1.8 Nitriding of iron-based ternary alloys.....	17
1.9 Scope of this thesis.....	17
1.10 Methodology.....	18
1.11 Outline of the thesis.....	18
2 The emergence and disappearance of a high density of microcracks in nitrided Fe-4.65at.%Al alloy	21
2.1 Introduction.....	22
2.2 Experimental.....	22
2.3 Results and discussion	23
2.3.1 X-ray diffraction: AlN phase identification	23
2.3.2 Microstructure of nitrided Fe-4.65at.%Al alloy.....	24
2.4 Conclusions.....	31
3 Unusual nucleation and growth of γ' iron nitride upon nitriding Fe-4.75at.%Al alloy	33
3.1 Introduction.....	34
3.2 Experimental.....	34
3.2.1 Specimen preparation.....	34
3.2.2 Nitriding	35
3.3 Microstructural characterization	37
3.3.1 Light optical and scanning electron microscopy.....	37

3.3.2	Transmission electron microscopy.....	37
3.3.3	Electron probe micro analysis.....	38
3.3.4	X-ray diffraction.....	39
3.4	Results and discussion.....	39
3.4.1	Unusual morphology of γ' iron nitride in the surface region.....	39
3.4.2	Nano-sized γ' precipitates in diffusion zone.....	40
3.4.3	Nano-sized cubic AlN precipitates in diffusion zone.....	43
3.4.4	Unexpected formation of ϵ -iron nitride.....	45
3.4.5	Diffraction-line broadening.....	48
3.4.6	Role of AlN precipitation.....	49
3.4.7	The negligible solubility of Al in γ'	51
3.5	General discussion: mechanism of γ' formation in Fe-Al alloy.....	55
3.6	Conclusions.....	57
4	Unusual precipitation of amorphous silicon nitride upon nitriding Fe-2at.%Si alloy	59
4.1	Introduction.....	60
4.2	Experimental details.....	61
4.2.1	Specimen preparation.....	61
4.2.2	Nitriding and denitriding.....	61
4.3	Microstructural characterization.....	62
4.3.1	Light microscopy and scanning electron microscopy.....	62
4.3.2	Transmission electron microscopy.....	62
4.3.3	Quantitative analysis of composition and nitrogen uptake.....	63
4.3.4	X-ray diffraction.....	63
4.3.5	Microhardness measurement.....	64
4.4	Morphology: light optical and scanning electron microscopy.....	64
4.5	Amorphous nature of the silicon-nitride precipitates.....	67
4.6	Ideally weak nitriding kinetics; hardness and nitrogen-concentration depth profiles.....	71
4.7	Nitrogen solubility of ferrite matrix and composition of the amorphous nitride precipitates.....	75
4.8	Initial stage of nitride precipitation and “self-catalysis”: non-monotonous hardness change and increasing nitrogen-uptake rate with nitriding time.....	77
4.9	Technological application of silicon-nitride precipitation in ferrite.....	79
4.10	Conclusions.....	80

5 Nitride formation and excess nitrogen uptake upon nitriding ferritic Fe-Ti-Cr alloys	83
5.1 Introduction.....	84
5.2 Experimental.....	85
5.2.1 Specimen preparation.....	85
5.2.2 Nitriding.....	86
5.2.3 X-ray diffraction.....	87
5.2.4 Microhardness measurement.....	87
5.2.5 Transmission electron microscopy.....	88
5.2.6 Electron probe microanalysis.....	88
5.3 Results and evaluation.....	89
5.3.1 The nitrided microstructure.....	89
5.3.2 Quantitative analysis of excess nitrogen uptake.....	94
5.4 General discussion: the role of the Ti/Cr atomic ratio.....	101
5.5 Conclusions.....	103
6 Summary	105
7 Zusammenfassung in deutscher Sprache	111
References	117
List of Publications	123
Acknowledgements	125
Curriculum Vitae	127

Chapter 1

Introduction

For better life and serviceability, many engineering components should be provided with improved properties in the surface adjacent region of the component, as this is usually the location of most severe loading. Thus a hard case on a soft core can induce pronouncedly improved mechanical performance. The outer hard case enhances the wear and fatigue resistance while the soft core “bulk” retains the toughness to bear the impact loads. Hard cases can be produced on many steel components for example by thermochemical diffusion treatments such as nitriding, carburizing, nitrocarburizing and carbonitriding, which are widely employed in the industry. Although these processes have been well established in industrial practice, fundamental understanding of the underlying micro-mechanisms is fragmentary which is due to the presence of a large number of alloying elements in commercial steels, which leads to complex interactions between inwardly diffusing species (N and C) and alloying elements. Fundamental studies have been carried out on simple model systems, such as pure iron [1-4], iron based binary [5-7] and ternary [8-10] alloys to understand the underlying phase transformations, which lead to the modification of the substrate microstructure upon thermochemical treatment.

Nitriding is the most widely employed thermochemical surface treatment to enhance the mechanical (fatigue and wear) and chemical (corrosion) properties of ferritic steel components. At the usual nitriding temperatures (450°C-580°C; below the Ac1 temperature of steel) no phase transformations, such as austenite-ferrite and austenite-martensite, can occur in the bulk of the steel components. Due to the absence of these bulk phase transformations, which involve large volume changes, good dimensional tolerance can be achieved, upon nitriding, which avoids the need of post-machining and/or post-heat treatments. This is a distinct advantage of the nitriding process over other surface heat treatments, like, carburizing and carbo-nitriding. Several nitriding methods are available such as gas nitriding, salt bath nitriding, plasma nitriding and laser nitriding. Among these nitriding methods, gaseous nitriding is the only method which can be thermodynamically controlled due to the possibility of precise control of the chemical potential of nitrogen in the gas atmosphere (see further).

1.1 Gaseous nitriding - thermodynamics

Gaseous nitriding is usually carried out in ammonia/hydrogen gas mixtures. The following two (hypothetical) reactions can occur during nitriding of solid substrate (iron/steel) in an ammonia/hydrogen gas mixture [11-12],



The sum of the above hypothetical reactions gives the following overall reaction,



where [N] represents the nitrogen dissolved interstitially in the ferrite or iron nitrides. Assuming local equilibrium between gas atmosphere and solid iron at the surface of the specimen/component (equation 3), the fugacity, f_{N_2} , of the hypothetical molecular nitrogen gas (N_2) in equilibrium with the solid substrate as shown in reactions (1) and (2) can be calculated from reaction (2) as,

$$f_{N_2}^{1/2} = K^{(2)} \frac{P_{NH_3}}{P_{H_2}^{3/2}} \quad (4)$$

where P_{NH_3} and P_{H_2} are the partial pressures of ammonia and hydrogen in the gas mixture, respectively, as pertaining to the overall reaction (3) and $K^{(2)}$ is the equilibrium constant for reaction (2). At the usual nitriding temperatures (450°C-580°C), the virtual nitrogen gas pressures (fugacities) can attain values of several thousand atmospheres [11]. Hence, it is impossible to achieve significant nitriding (i.e. producing an iron-nitrogen solid solution or iron nitrides) by employing nitrogen gas at atmospheric pressure. Thermodynamic equilibrium between ammonia/hydrogen gas mixture and solid iron substrate (at its surface) according to reaction (3) implies that the chemical potentials of nitrogen in the gas and solid phases are equal. In order to achieve such equilibria (reaction (3)) the thermal decomposition of ammonia within the gas mixture (reaction (2)) and the recombination of nitrogen atoms at the specimen surface to form molecular nitrogen gas (reaction (1)) should be negligible [12-13]. Slow thermal decomposition of ammonia within the gas phase, by maintaining sufficiently high gas flow rates during the nitriding treatment, ensures the establishment of local equilibrium at gas/solid

interface for a chemical potential of nitrogen as given by the composition of the ammonia/hydrogen gas mixture at the entrance of the furnace [12].

Adopting the same reference state for nitrogen in both gas and solid phases, the nitrogen activity, a_N , in the solid at the solid/gas interface is given by,

$$a_N = \frac{f_{N_2}^{1/2}}{P_{N_2}^{o1/2}} \quad (5)$$

where $P_{N_2}^o$ is the pressure of molecular nitrogen gas in the reference state (which is usually the atmospheric pressure).

Upon substituting equation (4) in equation (5), it follows

$$a_N = \frac{K^{(2)}}{P_{N_2}^{o1/2}} \frac{P_{NH_3}}{P_{H_2}^{3/2}} = \frac{K^{(2)}}{P_{N_2}^{o1/2}} r_N \quad (6)$$

where $r_N \left(= \frac{P_{NH_3}}{P_{H_2}^{3/2}} \right)$ is called the “nitriding potential”. Hence, at a given temperature, the chemical potential of nitrogen (the activity of nitrogen) depends on the applied nitriding potential. Thus any phase of the Fe-N system (Fig. 1.1) can be produced at the iron surface by choosing appropriate values for the temperature and the nitriding potential. Accordingly, the phase-stability fields of the Fe-N system can be represented in a temperature vs. nitriding potential diagram, which is known as the Lehrer diagram [14]. The original Lehrer diagram was later extended by incorporating the isoconcentration lines [15] which show the expected nitrogen contents in the respective phases for different nitriding conditions (Fig. 1.2).

With the help of calibrated mass flow controllers the partial pressures of ammonia and hydrogen in the (furnace) gas mixture can be set to establish a certain nitriding potential in the gas phase. This unique feature of the gas nitriding method allows controlled nitriding which in turn leads to a specific microstructural development. This is essential to obtain optimal properties for nitrided components.

1.2 Microstructure of nitrided zone

The microstructure of the nitrided zone which develops upon nitriding pure iron (or iron-based alloy), below the eutectoid temperature (592°C for pure iron-nitrogen) using a nitriding potential which stabilizes the $\epsilon\text{-Fe}_3\text{N}_{1+y}$ at the iron surface (cf. Fig. 1.2) is shown schematically in Fig. 1.3. The nitrided zone can be subdivided into (i) the surface adjacent iron-nitride compound layer

which contains ε -Fe₃N_{1+y} (hcp arrangement of Fe atoms with ordered occupation of N at octahedral interstitial sites; hereon referred as ε) and γ' -Fe₄N_{1-x} (fcc arrangement of Fe atoms with ordered occupation of N at octahedral interstitial sites; hereon referred as γ') sub layers, and (ii) the diffusion zone underneath the compound layer where nitrogen is either dissolved interstitially in the octahedral interstitial sites of bcc ferrite matrix or precipitated (upon cooling and possibly subsequent aging) as γ' and α'' -Fe₁₆N₂ (bct arrangement of iron atoms with ordered occupation of N at octahedral interstitial sites) nitrides.

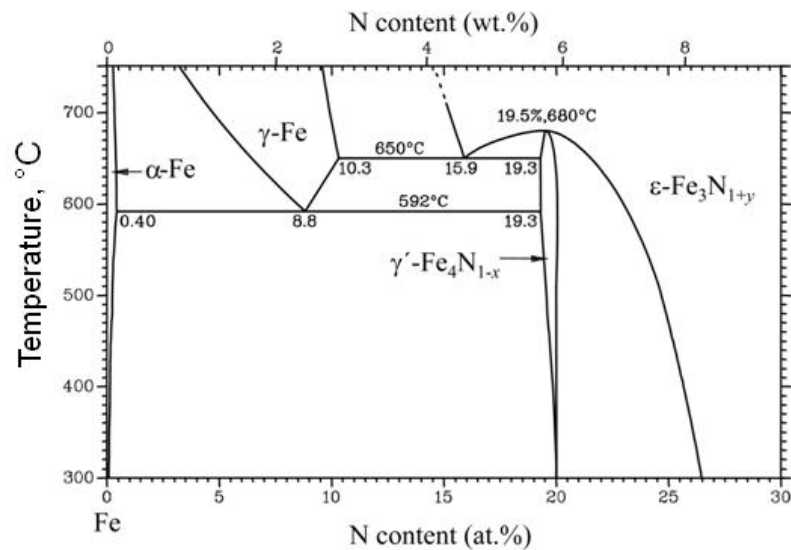


Fig. 1.1: Metastable Fe-N phase diagram redrawn according to Ref. [16]

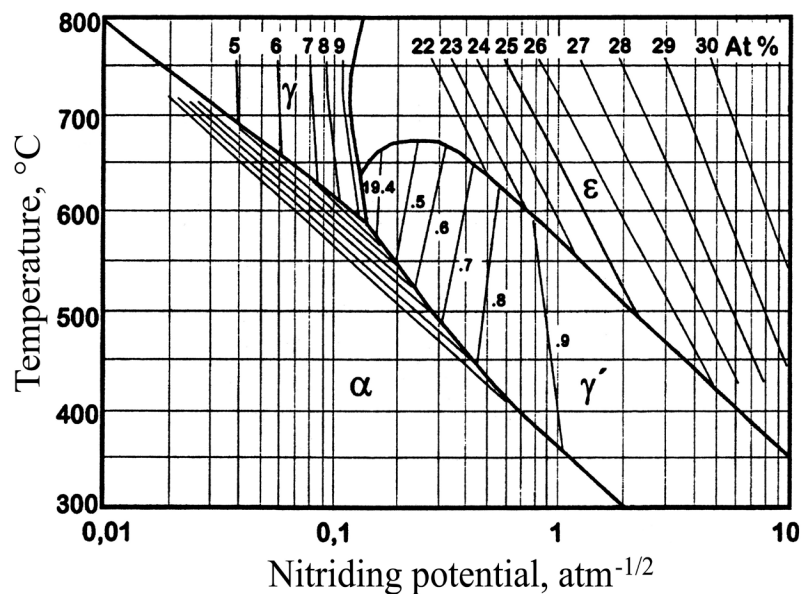


Fig. 1.2: Lehrer diagram [14] with included isoconcentration lines [15] which show the expected nitrogen contents in the respective Fe-N phases for different nitriding conditions.

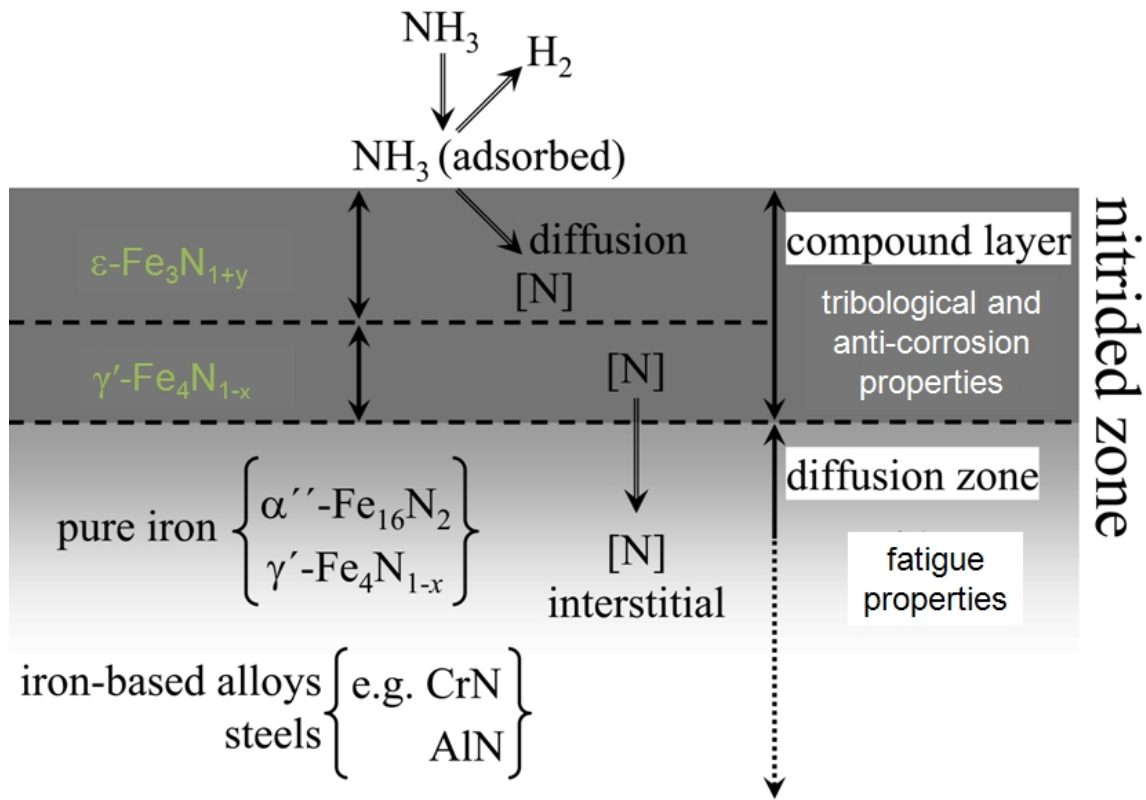


Fig. 1.3: Schematic illustration of the microstructure of the nitrified region which develops upon nitriding iron or iron-based alloy. Surface adjacent iron-nitride “compound layer” consists of ϵ and γ' sub layers, and the “diffusion zone” beneath the compound layer where nitrogen dissolves interstitially and may also contain precipitates of iron nitrides or alloying element nitrides.

In the case of iron-based alloys containing nitride forming alloying elements ($\text{Me} = \text{Cr}, \text{Al}, \text{V}, \text{Ti}$), the alloying elements will get incorporated into the compound layer either as ternary Fe-Me-N compounds or as alloying element nitride particles encompassed by the iron-nitride layers. In the diffusion zone, the alloying elements having stronger affinity towards nitrogen react with interstitially dissolved nitrogen and precipitate as alloying element nitride. The outer iron-nitride compound layer is also called “white layer”, due to its appearance in light optical micrographs after etching with “Nital”.

1.3 Alloying element nitrides in the ferrite matrix

Iron-based materials can be alloyed with one or more of the elements, such as $\text{Al}, \text{Cr}, \text{V}$ and Ti , which have a strong affinity for nitrogen. The large thermodynamic driving force available for the precipitation of alloying element nitrides (Table 1.1), explains the formation of nano-sized alloying element nitride precipitates in the ferrite matrix of the diffusion zone. For experiments

intended to study in particular these nitride-precipitation processes, the nitriding parameters (temperature and nitriding potential) should be chosen such that the formation of (metastable) iron nitrides do not occur (i.e. T and r_N should lie within the α -region of the Lehrer diagram; Fig. 1.2). Such nitriding treatments, where iron nitride formation at the surface is avoided, are termed “internal nitriding”. As the diffusion zone is responsible for the increase of the fatigue strength, in applications where enhancement of fatigue strength is the major criteria (for example springs), it is essential to avoid the development of outer brittle iron-nitride compound layers.

The ease with which an alloying element nitride can nucleate in ferrite depends on (i) the available thermodynamic driving force (ΔG_f° ; 3rd column in Table 1.1), (ii) the amount of volume misfit which occurs when dissolved alloying element in ferrite precipitates as alloying element nitride (see column 4 in Table 1.1) and (iii) the possibility of establishing a low energy (semi) coherent interface between alloying element nitride precipitate and ferrite matrix.

The cubic nitrides (TiN, CrN and VN) can establish a low energy (semi) coherent interface with the ferrite matrix by precipitating along the $\{100\}$ planes of the ferrite matrix, according to Bain orientation relationship between (fcc) precipitate and the (bcc) matrix [5, 7]. Although the cubic (NaCl type) VN and CrN have relatively low negative values of ΔG_f° (as compared to TiN), their precipitation inside the ferrite matrix is relatively easy because of a relatively low volume misfit with the ferrite matrix (Table 1.1). The large thermodynamic driving force (ΔG_f°) for TiN precipitation causes its relatively easy precipitation, even though it has a relatively large volume misfit with the ferrite matrix as compared to CrN and VN (Table 1.1).

The precipitation of hexagonal AlN inside the ferrite matrix is difficult because of its large volume misfit and the impossibility of achieving a low energy interface with the ferrite matrix. Due to this nucleation difficulty, AlN also prefers to precipitate in a metastable cubic (NaCl type) crystal structure, which has a relatively small volume misfit (Table 1.1) and which can establish a low energy (semi) coherent interface with the ferrite matrix [17]. Similar to hexagonal AlN, the precipitation of hexagonal Si_3N_4 is very difficult due to its very large volume misfit with the ferrite matrix (Table 1.1). In order to establish a low energy interface with the ferrite matrix, Si_3N_4 prefers to precipitate in a metastable amorphous state due to the lower energy of the amorphous/crystalline interface as compared to the crystalline/crystalline interface [18-19]. Due to this discussed homogeneous nucleation difficulty, both AlN and Si_3N_4 precipitate preferably on defects (dislocations) [20-21] which act as heterogeneous nucleation sites. No information is available in the literature on the possible precipitation of Ge_3N_4 in ferrite.

Precipitation of Ge_3N_4 inside the ferrite matrix is expected to be extremely difficult due to its extremely large volume misfit with the ferrite matrix and a smaller chemical driving force than for Si_3N_4 (Table 1.1).

In the literature, the precipitation of cubic nitrides CrN, TiN and VN in ferrite has been investigated extensively, in contrast with the precipitation of the hexagonal nitrides AlN and Si_3N_4 . Against this background this thesis presents investigations of the precipitation of the hexagonal nitrides, AlN and Si_3N_4 .

Table 1.1: Standard Gibbs energy of formation for reaction with one mole of N_2 for selected binary nitrides (Me_xN_y) and the volume misfit with the ferrite matrix when the dissolved alloying element (Me) precipitates as alloying element nitride [22-23].

Nitride Me_xN_y	Crystal system	ΔG_f° (298 K) (kJ/mol)	vol. misfit (%) $\left(\left(\frac{\frac{M_{\text{Me}_x\text{N}_y}}{x} - \frac{\text{at. wt}_{\text{Fe}}}{\rho_{\text{Fe}}}}{\frac{\text{at. wt}_{\text{Fe}}}{\rho_{\text{Fe}}}} \right) * 100 \right)^\#$
$\beta\text{-Ge}_3\text{N}_4$	hexagonal	-153	144
$\beta\text{-Si}_3\text{N}_4$	hexagonal	-358	106
AlN	hexagonal	-574	77
AlN	cubic	-	43
TiN	cubic	-618	64
VN	cubic	-381	50
CrN	cubic	-185	52
$\gamma'\text{-Fe}_4\text{N}$	cubic	+7 ¹	16

[#] where M , ρ and at. wt are molecular mass, density and atomic mass, respectively

1.4 Excess nitrogen

The total amount of nitrogen, $[N]_{total}$, taken up by the Fe-Me alloys upon nitriding has been often found to be larger than the theoretically expected nitrogen content denoted as “normal nitrogen” ($[N]_{normal}$) which is the sum of (i) the amount of nitrogen necessary to precipitate the total amount of alloying element as the stoichiometric alloying element nitride ($[N]_{MeN}$) and (ii)

¹ The metastable iron nitrides have a strong thermodynamic tendency to dissociate into iron and molecular nitrogen gas. Iron nitrides can only be stabilized by equilibrating with ammonia/hydrogen gas mixtures which is equivalent to equilibrating with molecular nitrogen gas at several thousand atmospheres of pressure [11-12] (see section 1.1).

the equilibrium nitrogen solubility of unstrained pure ferrite ($[N_{\alpha}^{\circ}]$) i.e., $[N]_{normal} = [N]_{MeN} + [N]_{\alpha}^{\circ}$. The nitrogen content taken up above the normal nitrogen content is called “excess nitrogen” ($[N]_{exe}$), i.e. $[N]_{exe} \equiv [N]_{total} - [N]_{normal}$. This excess nitrogen can be present at several locations in the nitrated Fe-Me alloy [24];

- (i) adsorbed at the interface between alloying element nitride and ferrite matrix; $[N]_{interface}$;
- (ii) additional nitrogen can interstitially dissolve in the ferrite matrix due to the hydrostatic elastic strain component induced in the ferrite matrix as a result of the misfit between the alloying element nitride and the ferrite matrix; $[N]_{strain}$
- (iii) nitrogen associated with dislocations; $[N]_{dist}$.

Excess nitrogen which cannot take part in the interstitial diffusion process ($[N]_{interface} + [N]_{dist}$), contributing to growth of the nitrated zone, is called “immobile excess nitrogen”, whereas the excess nitrogen which can take part in the interstitial diffusion process ($[N]_{strain}$) is called “mobile excess nitrogen” [25]. Quantitative knowledge about the different forms of excess nitrogen is essential to predict/model the growth kinetics of the diffusion zone [6, 25]. The determination of nitrogen absorption isotherms provides quantitative values for the different types of excess nitrogen [6-8, 26-28].

1.5 Development of iron-nitride compound layers on pure iron

The finite rates of competing surface reactions such as ammonia dissociation, nitrogen diffusion into the solid substrate and the association of surface adsorbed nitrogen atoms and their subsequent desorption as N_2 molecules, causes the surface nitrogen concentration to increase with time, until the realization of a stationary state or the local thermodynamic equilibrium [2, 12-13] (i.e. attaining the equilibrium nitrogen solubility of ferrite (at the surface), as expected according to the employed temperature and nitriding potential). To achieve local thermodynamic equilibrium (instead of a stationary state), the desorption rate of nitrogen gas from the surface by the association of the surface adsorbed nitrogen atoms, must be neglectable [2, 12-13]. Once the solubility limit of the ferrite matrix (maximum solubility is 0.4 at.% at 592°C) has been surpassed, γ' iron nitride nuclei can occur on the surface. The lateral growth of these nuclei eventually leads to the development of a closed γ' layer. The finite time needed to surpass the nitrogen solubility of the ferrite results in an incubation time for the nucleation of γ' . If the

nitriding potential in the gas atmosphere is high enough, before the closed γ' layer develops, ε iron nitride nucleates on top of the γ' nuclei and the lateral growth of such twin nuclei eventually leads to the development of closed ε/γ' sub layers (cf. Fig. 1.4) [29]. The ferrite matrix beneath/adjacent to the compound layer maintains local thermodynamic equilibrium with the iron-nitrides, according to the Fe-N phase diagram.

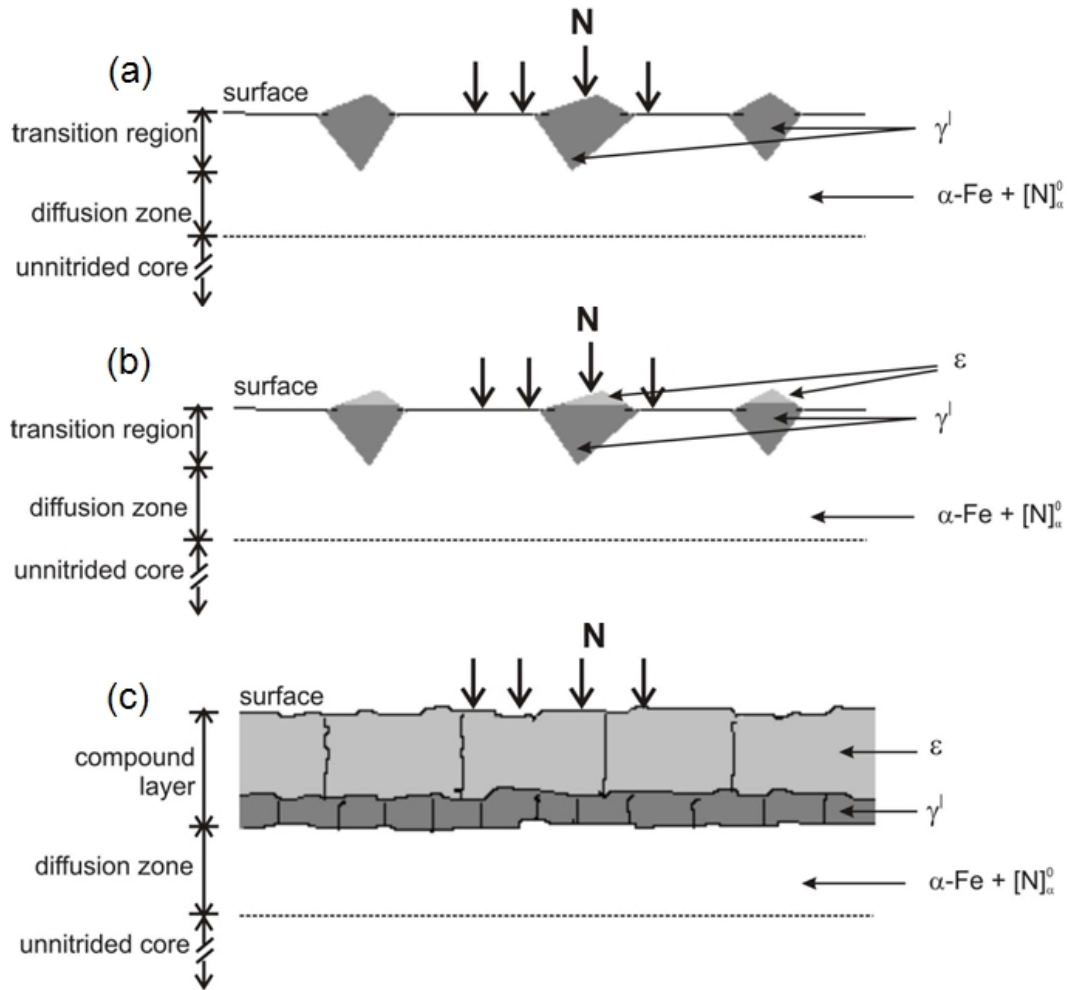


Fig. 1.4: Schematic illustration of the development of iron-nitride compound layers upon nitriding pure iron [29]. γ' nuclei develop at the surface after the nitrogen solubility limit of the ferrite surpasses (a). If the nitriding potential is high enough ε nucleates on top of the γ' nuclei (b) and the lateral growth of such ε/γ' twin nuclei results in the formation of closed surface iron-nitride layers (c).

1.6 Development of iron-nitride compound layers on iron-based alloys

The presence of substitutionally dissolved alloying elements (Cr, V, Ti, Al and Si) in ferrite influences the nucleation and growth of iron-nitride compound layers. In the case of alloying elements having relatively stronger affinity for nitrogen (as compared to the affinity for nitrogen of iron), alloying element nitride can precipitate in the ferrite matrix: the inwardly diffusing

nitrogen atoms react with the alloying elements to form alloying element nitrides. Then the nitrogen solubility limit of the ferrite matrix can be surpassed only after complete precipitation of alloying element as nitride has been realized. Thus the incubation time for iron-nitride nucleation on the surface will be larger as compared to that of nitriding of pure iron. The later growing iron-nitride compound layer encompasses the alloying element nitride precipitates already developed inside the ferrite matrix [29-30].

In the case of alloying elements which have a (limited) solubility in iron nitrides and which are difficult to precipitate as alloying element nitrides in the ferrite matrix (cf. section 1.3), several competing reactions can be considered: (i) iron-nitride nucleation can become suppressed until all alloying element has precipitated as alloying element nitride (ii) iron nitrides can be forced to nucleate and grow under para-equilibrium conditions and (iii) pore formation due to N_2 gas formation can occur (cf. section 1.7).

In this thesis the role of Al, for which precipitation as nitride in ferrite is known to be difficult (cf. section 1.3), on the nucleation and growth of iron-nitride compound layers has been investigated.

1.7 Pore formation in the nitrified zone: metastable nature of the Fe-N phases

During nitriding, only the Fe-N phase at the surface of the specimen/component (Fe-N ferrite, γ' and ϵ iron nitrides) which is in direct contact with the ammonia/hydrogen gas mixture can be thermodynamically stable if local thermodynamic equilibrium prevails. The Fe-N phases in the deeper regions of the nitrified zone, which are not in direct contact with the gas atmosphere, are thermodynamically unstable: a strong (thermodynamic) tendency exists for the Fe-N phases, which are not in direct contact with the gas atmosphere, to dissociate into iron and molecular nitrogen (N_2) gas so that the overall Gibbs energy of the system decreases [11]. This can lead to the nucleation and growth of molecular nitrogen gas filled pores in the nitrified zone, especially at easy nucleation sites such as grain boundaries (Fig. 1.5). Strong tendency for the pore formation exists in the Fe-N phase near to the surface (usually ϵ iron-nitride) where the activity of nitrogen is highest. At the initial stages of nitriding, the composition gradient driven diffusion of nitrogen atoms to the deeper regions of the iron-based substrate dominates, over the association of dissolved nitrogen atoms to nitrogen gas molecules leading to pore formation. Hence, after short nitriding times the nitrified zone can be pore free. However, upon prolonged

nitriding every Fe-N phase can in principle become porous as there exist a thermodynamic driving force for the process of pore formation.

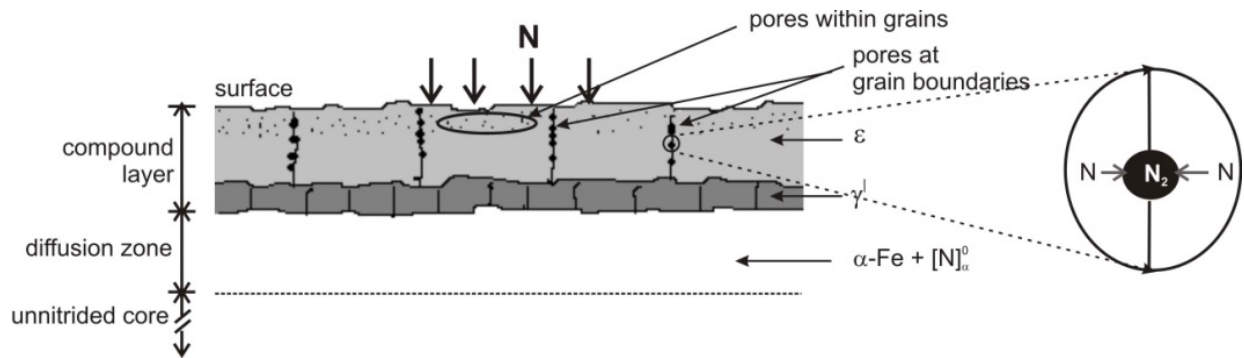


Fig. 1.5: Schematic illustration of the development of pores in the iron-nitride compound layers [29].

1.8 Nitriding of iron-based ternary alloys

In the field of nitriding, most of the fundamental studies were focused on the iron-based model binary alloys. In order to understand the nitriding behaviour in a multi component (steel) alloy it is essential to understand the more complex interactions occurring upon nitriding ternary alloys. To this end some investigations were carried out on iron-based ternary alloys such as Fe-Cr-C [31-32], Fe-Cr-Al [8-10], Fe-Si-Al [33] and Fe-Mn-Si [34]. Recently, metastable, ternary nitrides precipitation was observed, instead of precipitation of the thermodynamically stable binary nitrides [8-9]. In this thesis, ternary Fe-Ti-Cr alloys were nitrided to investigate the crystal structure and morphology of the inner nitrides and their influence on the excess nitrogen uptake.

1.9 Scope of this thesis

This thesis is devoted to achieve fundamental understanding on the microstructural mechanisms involved in the precipitation of nitrides upon nitriding of iron-based alloys. The attention has been especially focused on the following aspects;

- (i) The mechanism of AlN precipitation in the ferrite matrix of Fe-4.65at.%Al alloy and its influence on the associated microstructural development.
- (ii) The role of substitutionally dissolved Al on the nucleation and growth of iron-nitrides upon nitriding ferritic Fe-4.75at.%Al alloy.
- (iii) The structure, morphology and kinetics of Si_3N_4 precipitation in the ferrite matrix of a Fe-2at.%Si alloy.

- (iv) Interaction of N, Cr and Ti upon nitriding ternary Fe-Cr-Ti alloys of variable Cr/Ti ratio.

1.10 Methodology

For the gaseous nitriding treatment (cf. section 1.1) high purity ammonia (99.998 vol.%) and hydrogen (99.999 vol.%) gases were used. A total gas flow rate of 500 ml/min was employed which corresponds with a linear gas velocity of 13.5 mm/s at room temperature, for the 28 mm diameter quartz-tube furnace used in this work. Maintaining a high linear gas velocity minimizes the possibility of change of the chemical composition of the gas mixture due to the dissociation of ammonia. Partial pressures of ammonia and hydrogen in the gas mixture were controlled by using the calibrated mass flow controllers through which gases are allowed to enter the furnace at a predetermined flow rates. For microstructural characterization light microscopy, hardness measurements, scanning and transmission electron microscopy, X-ray diffraction and electron-probe microanalysis were employed. For the investigations focusing on quantitative analysis of the amount of nitrogen taken up, weight measurements, before and after the nitriding treatment, were performed using a high accuracy microbalance.

1.11 Outline of the thesis

The peculiar phenomenon of the emergence and disappearance of a high density of microcracks and the occurrence of AlN precipitation free zones around the ferrite grain boundaries, upon nitriding ferritic Fe-4.65at.%Al alloy is dealt with in chapter 2. The mechanism underlying these peculiar phenomena is explained as a consequence of competition between the association of interstitial dissolved nitrogen atoms to nitrogen-gas molecules, leading to pores at the grain boundaries, and the precipitation of the equilibrium, hexagonal, wurtzite type, AlN.

The role of substitutionally dissolved Al on the nucleation and growth of γ' iron-nitride, upon nitriding ferritic Fe-4.75at.%Al alloy is discussed in chapter 3. As compared to the nitriding of pure iron, where a layer of γ' develops at the surface, an unusual morphology of γ' plates developed at the surface, which plates deeply penetrate the substrate. Additionally an unexpected formation of ϵ iron-nitride was observed. On the basis of a series of dedicated nitriding experiments it was shown that the unusual microstructural development is a

consequence of the negligible solubility of Al in γ' and the obstructed precipitation of the thermodynamically stable, hexagonal (wurtzite-type) AlN in ferrite.

The structure, morphology and kinetics of silicon-nitride precipitation in ferritic Fe-2at.%Si alloy are the themes of chapter 4. Ideally *weak* nitriding kinetics in *thick* specimens, the development of amorphous instead of crystalline silicon nitride, and a non-monotonous change of hardness with nitriding time were observed. These peculiar phenomena were successfully explained considering the large volume misfit between silicon nitride and ferrite and the lower energy of the amorphous/crystalline interface as compared to the crystalline/crystalline interface.

Finally, in chapter 5, the investigations on the ternary Fe-Ti-Cr alloys are reported, thereby focusing on the crystal structure and morphology of the nitride precipitates and the uptake of excess nitrogen. Three ternary Fe-Ti-Cr alloys, each having a total alloying element (Ti+Cr) content of 0.3 at.%, but a varying Ti/Cr atomic ratio, have been investigated. Instead of the precipitation of the thermodynamically stable cubic (NaCl type) TiN and CrN, precipitation of metastable, cubic (NaCl type), ternary nitride, $Ti_{1-x}Cr_xN$ occurred. Analysis of the different types of excess nitrogen showed a distinct dependency of the amount of excess nitrogen on the Ti/Cr atomic ratio in the ternary Fe-Ti-Cr alloys. The observed phenomena were explained in terms of the volume misfit for the metastable ternary nitride decreasing with Ti/Cr atomic ratio and the higher chemical affinity of Ti for N than of Cr for N.

Chapter 2

The emergence and disappearance of a high density of microcracks in nitrided Fe-4.65at.%Al alloy

S. Meka, S.S. Hosmani, A.R. Clauss and E.J. Mittemeijer

Abstract

Nitriding of recrystallised and cold-rolled Fe-4.65at.%Al alloy at 550°C in an ammonia–hydrogen gas mixture of nitriding potential $0.104 \text{ atm}^{-1/2}$ indicated that nucleation of the thermodynamically (most) stable hexagonal (wurzite) AlN in the ferrite matrix of recrystallised specimen is difficult. The competition between the precipitation of nitrogen gas (dissociation of nitrogen supersaturated ferrite into pure ferrite and nitrogen gas) at the grain boundaries and the precipitation of hexagonal (wurzite) AlN led, via the coalescence of pores filled with nitrogen gas, to the emergence of microcracks along the grain boundaries and the formation of nitride-precipitate free zones near the grain boundaries of the recrystallised specimens. Upon continued nitriding the initially partially nitrided grains became fully nitrided and the microcracks disappeared.

2.1 Introduction

Many nitriding steels (used in applications like gears, pump-parts, crankshafts etc.) contain aluminium as one of the alloying elements because of its strong affinity to nitrogen leading, upon nitriding, to the precipitation of AlN precipitates causing pronounced hardening [35]. Nitriding of iron-based aluminium alloys has been studied in several investigations [17, 21, 26-27, 36-38]. The nitride AlN can have different crystal structures (cubic NaCl type, cubic zincblende type, hexagonal wurzite type), unlike the nitrides CrN (cubic NaCl type) and VN (cubic NaCl type) [39]. The thermodynamically most stable crystallographic form of AlN under the usual nitriding conditions is the hexagonal crystal structure type. This stable hexagonal AlN has been observed, indeed, in nitrided Fe–Al alloys [17, 27]. However, in nitrided Fe–Al alloys AlN can also occur in the cubic (NaCl type) modification, in particular in nitrided cold-rolled (deformed) Fe–Al alloys [17, 40]. The formation of the cubic zincblende type AlN has never been observed in nitrided Fe–Al alloys. In the past, most investigations had focused on the kinetics of AlN precipitation (in the ferrite matrix) [17, 21, 27, 38], the crystal structure of AlN [17, 27, 40] and the occurrence of ‘excess nitrogen’ (i.e. the presence of more nitrogen than necessary for precipitation of all aluminium as nitride and equilibrium saturation with nitrogen of the ferrite matrix (cf. section 1.4 of chapter 1)) in nitrided Fe–Al alloys containing a small amount (about 2 at.%) of aluminium [17, 21, 26-27, 36-38]. Little attention has been focused on the morphology of the nitrided zone (“diffusion zone”). In this chapter a peculiar observation, involving the massive development of microcracks and their subsequent disappearance in the nitrided microstructure of a relatively high Al content Fe-4.65at.%Al alloy, is presented and discussed.

2.2 Experimental

Fe-4.65at.%Al alloy castings (cylindrical shape: diameter 10 mm; length 100 mm) were prepared from pure elements, Fe (purity: 99.98 wt.%) and Al (purity: 99.999 wt.%), in an inductive furnace under argon gas atmosphere. The amounts of aluminium and impurities, like oxygen, nitrogen, carbon and sulphur, in the alloy casts produced were determined by chemical analysis (for details see section 3.2.1 of chapter 3). The alloy composition thus determined is given in Table 2.1. The alloys were cold rolled into sheets of a thickness of about 1 mm. These sheets were cut into rectangle specimens of lateral dimensions 16 mm × 20 mm. The specimens were annealed in argon gas for 1 h at 850°C to get a recrystallised microstructure. Next, the specimens

were ground, polished (last step: 1 μm diamond paste) and subsequently cleaned with ethanol in an ultrasonic cleaner.

Table 2.1: Amounts of aluminium and light element impurities for the alloy used in this work.

Al (wt.%)	Al (at.%)	O ($\mu\text{g/g}$)	N ($\mu\text{g/g}$)	C ($\mu\text{g/g}$)	S ($\mu\text{g/g}$)
2.3 ± 0.02	4.65 ± 0.02	21 ± 3	< 5	13 ± 2	< 5

Nitriding was performed in a laboratory-built nitriding furnace (as described in section 3.2.2 of chapter 3) at 550 °C for 12 h in an ammonia/hydrogen gas mixture with a gas flow of 455 ml/min of H_2 and 45 ml/min of NH_3 . Hence, the nitriding potential, r_N [11-12], equalled $0.104 \text{ atm}^{-1/2}$; under these conditions iron nitrides cannot develop. After nitriding some of the specimens were further nitrided at the same temperature and nitriding potential for 24 h. Cross-sections of both types of such nitrided specimens were analysed by optical microscopy, microhardness measurements and electron probe microanalysis (EPMA) according to procedures described in detail in section 3.3 of chapter 3.

It was found (see section 2.3) that a nitriding time of 12 h, as applied to the first series of specimens (see above), is too small to achieve an up to saturation level nitrided zone. To apply X-ray diffraction (for phase analysis) to fully nitrided alloy material, one specimen was nitrided for 65 h at 550°C and at $r_N = 0.104 \text{ atm}^{-1/2}$. X-ray diffractometry was performed using a Philips X'Pert diffractometer with a graphite monochromator in the diffracted beam using Co- $K\alpha$ radiation and employing the Bragg–Brentano geometry. The diffraction angle (2θ) range scanned was 30 – 90°, with a step size of 0.05° (counting time of 80 s per step). The X-ray diffractograms were recorded from specimen surfaces as obtained after nitriding. To identify the phases from the positions of the diffraction peaks, the data from the JCPDS data base [41] were used.

2.3 Results and discussion

2.3.1 X-ray diffraction: AlN phase identification

An X-ray diffractogram recorded from the specimen surface of Fe-4.65at.%Al alloy nitrided for 65 h at 550°C and at $r_N = 0.104 \text{ atm}^{-1/2}$ is shown in Fig. 2.1. The possible positions of AlN reflections (according to the JCPDS data base [41]) have also been indicated in Fig. 2.1. The presence of hexagonal wurzite AlN phase (see locations marked as HCP1 and HCP2 in Fig. 2.1) is evident.

Diffraction peaks at the possible positions of the cubic (NaCl type) AlN do not occur distinctly (Fig. 2.1). The small intensity hump on the tail at the high angle side of the α -Fe 110 reflection may be due to the presence of some coherent, cubic (NaCl type) AlN which leads to a local strong tetragonal distortion of the ferrite matrix (cf. Ref. [7]). It is concluded that the AlN precipitates are, at least predominantly, of the hexagonal, wurzite type crystal structure. The presence of a minor amount of cubic, rock-salt type AlN precipitates cannot be excluded. These results agree well with those obtained previously for a nitrated, relatively low Al content Fe-2at.%Al alloy [17].

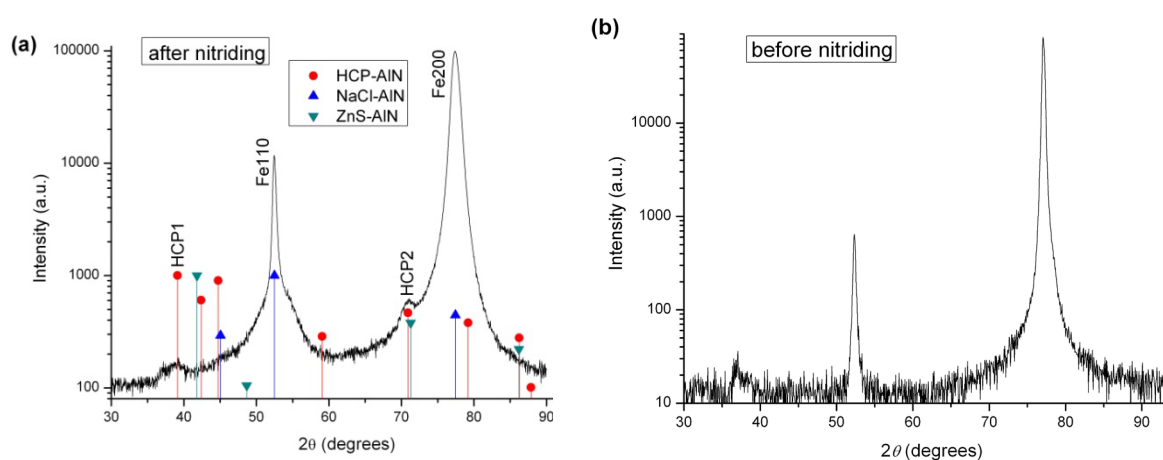


Fig. 2.1: (a) X-ray diffractogram (Co-K α radiation) recorded from the specimen surface of Fe-4.65at.%Al alloy nitrated for 65 h at 550°C and at $r_N = 0.104 \text{ atm}^{-1/2}$. The possible positions of hexagonal (wurzite type) and cubic (zincblende type and NaCl type) AlN reflections (according to Ref. [41]) have been indicated; the lengths of the line segments at these locations correspond to the relative intensities for these reflections as expected for the texture-less case. (b) X-ray diffractogram (Co-K α) recorded from the specimen surface of unnitrided Fe-4.65at.%Al alloy. The small diffraction peak at about 37° 2θ in (a) is also present in the X-ray diffractogram recorded from the surface of the unnitrided specimen (see (b)) and is ascribed to the presence of some surface oxide.

2.3.2 Microstructure of nitrated Fe-4.65at.%Al alloy

Optical micrographs of the *unetched* cross-sections of Fe-4.65at.%Al specimens nitrated for 12 h at 550°C and at $r_N = 0.104 \text{ atm}^{-1/2}$ are shown in Figs. 2.2a and b; the optical micrographs of the *unetched* cross-section of Fe-4.65at.%Al specimens nitrated further for 24 h at 550°C and at $r_N = 0.104 \text{ atm}^{-1/2}$ are shown in Figs. 2.2c and d. These micrographs reveal the presence of multiple “open grain boundaries”, further denoted as “microcracks”, in the nitrated microstructure. For the specimen nitrated for 12 h, the microcracks occur at relatively small depth beneath the

surface (see Figs. 2.2a and b). For the specimen further nitrided for 24 h, the microcracks occur at distinctly larger depth beneath the surface (see Figs. 2.2c and d).

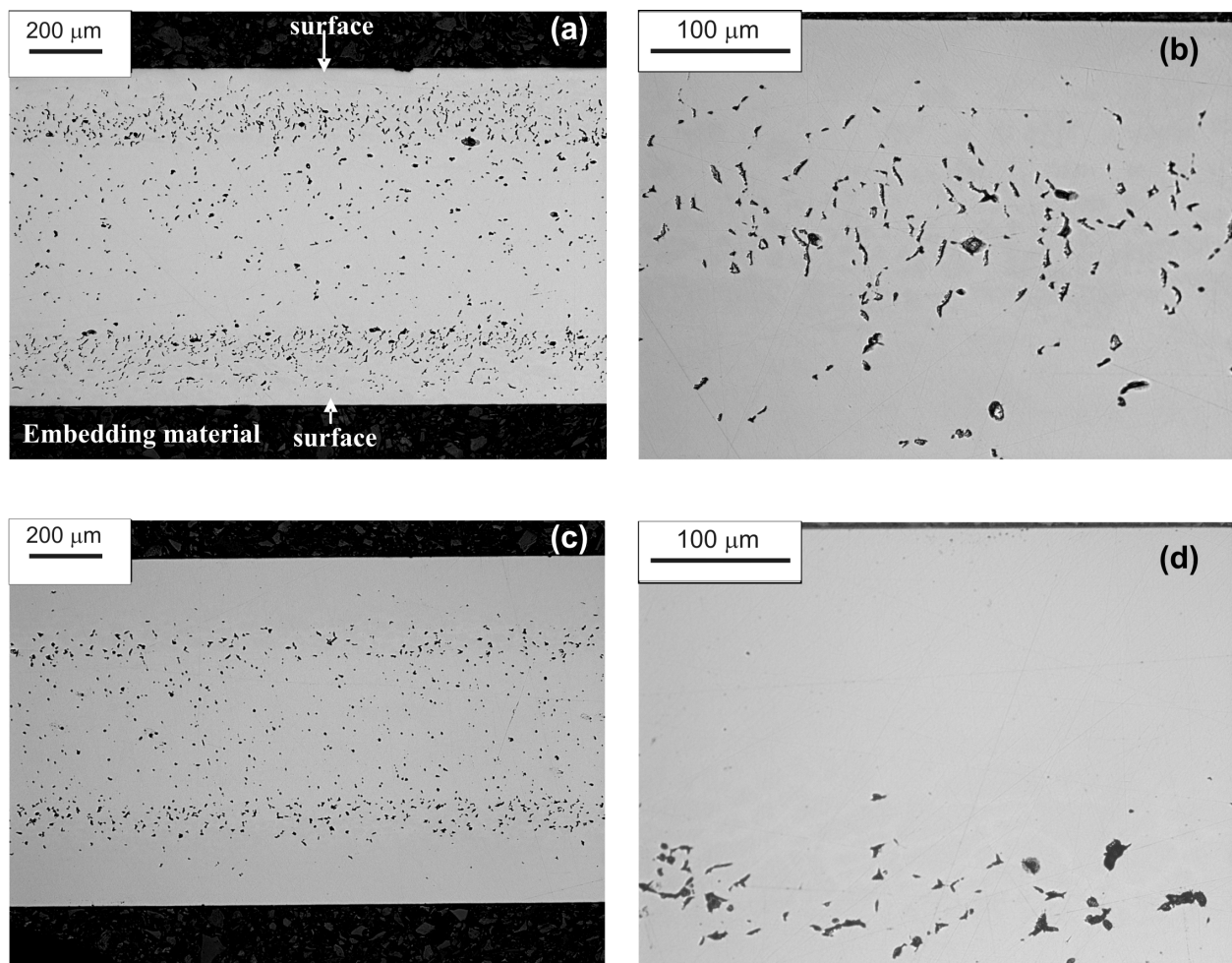


Fig. 2.2: Optical micrographs of the unetched cross-section of the Fe-4.65at.%Al specimens nitrided at 550°C and at $r_N = 0.104 \text{ atm}^{-1/2}$ for (a), (b) 12 h and (c), (d) 12 + 24 h (same specimen). Micrographs shown in (b) and (d) are enlarged parts of the cross-sections adjacent to the specimen surface.

Optical micrographs of the *etched* cross-sections and the corresponding nitrogen and aluminium concentration–depth profiles (EPMA results) for the specimen nitrided for 12 h and for the specimen nitrided further for 24 h are shown in Figs. 2.3 and 2.4, respectively. For the specimen nitrided for 12 h, each grain within a very small region near to the surface has been fully nitrided. The region underneath has only been partially nitrided (Fig. 2.3): see the fluctuations (ups and downs) in the nitrogen concentration–depth profile and the varying etching contrast in the optical micrograph: a high nitrogen content at the centre of the grain and almost no nitrogen near and at the grain boundaries; the Al concentration is practically constant, i.e. no

depletion of Al near (and at) grain boundaries occurs (see Fig. 2.3b). The hardness at the centre of the grain is higher than near to the grain boundary (Fig. 2.5). Thus, the nitrogen (and aluminium) concentration–depth profiles and the optical micrographs (Fig. 2.3) and the microhardness variation (Fig. 2.5) indicate that ups in the nitrogen concentration are associated with the occurrence of dark regions at the centre of the grains. Evidently, the centres of the grains are the nitrated regions of the grains and the surrounding regions adjacent to the grain boundaries are (nitride-) precipitate free zones (PFZs). Similar results have been obtained for the specimens nitrated for 12 + 24 h (Fig. 2.4); in this case the surface adjacent region of fully nitrated grains (up to saturation level; no PFZs adjacent to grain boundaries) is thicker.

It follows from the results shown in Figs. 2.2 – 2.5 that the microcracks occur in the region where only partially nitrated grains are present, whereas the microcrack-free region near the surface coincides with the region where fully nitrated grains are present.

The striking observation made here is that evidently microcracks are formed at an initial stage of nitriding, i.e. at locations where only partially nitrated (in the centre of) grains occur and that upon further nitriding, leading to fully nitrated grains at the location concerned, these microcracks become closed (disappear); new microcracks appear at deeper locations where (again) partially nitrated grains occur first.

The possible mechanism of formation and elimination of microcracks could be as follows. During nitriding of Fe-4.65at.%Al, nitrogen from the ammonia/hydrogen gas mixture diffuses into the specimen. Nucleation of the thermodynamically (most) stable hexagonal (wurzite) AlN in the ferrite matrix can be difficult due to its relatively high volume misfit with the ferrite matrix [38]. It has been shown elsewhere [38] that in recrystallised Fe-based Fe–Al alloys AlN precipitation is rate controlled by both nucleation and growth: the process starts with saturation of the ferrite matrix followed by a slowly beginning hexagonal AlN precipitation [21]; the maximum nitride precipitation rate occurs for a progressed stage of nitriding. It can thus be

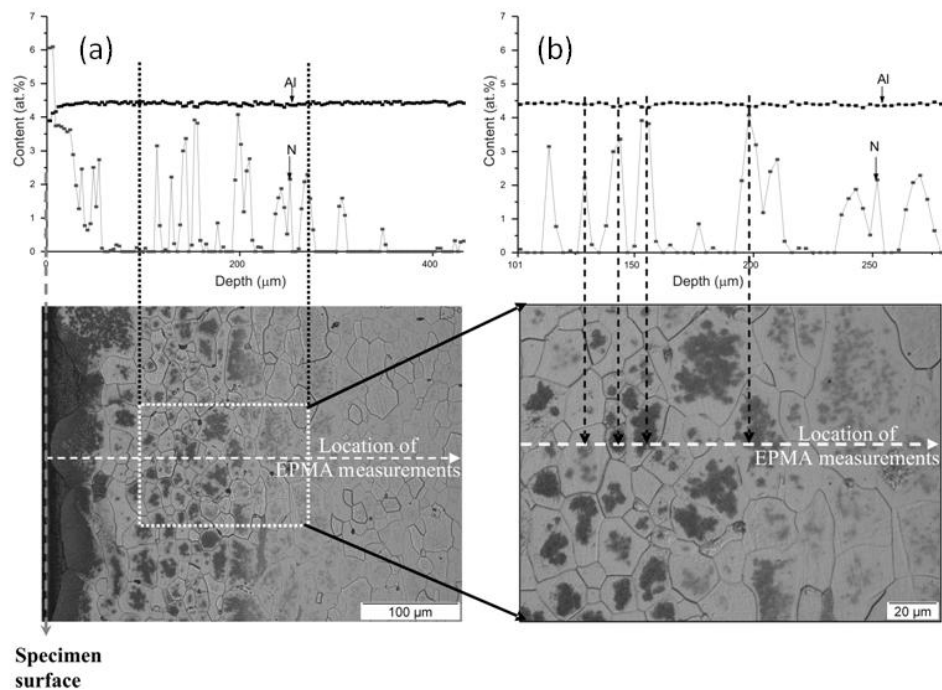


Fig. 2.3: (a) Elemental (N and Al) concentration–depth profiles (EPMA results) together with the optical micrograph of the cross-section analysed (which was etched after the EPMA measurements) showing the location of the EPMA measurements (dashed horizontal line), for the Fe-4.65at.%Al specimen nitrided for 12 h at 550°C and at $r_N = 0.104 \text{ atm}^{-1/2}$. (b) Similar to (a) but for enlarged portion of (a) as indicated by the dashed rectangle in (a).

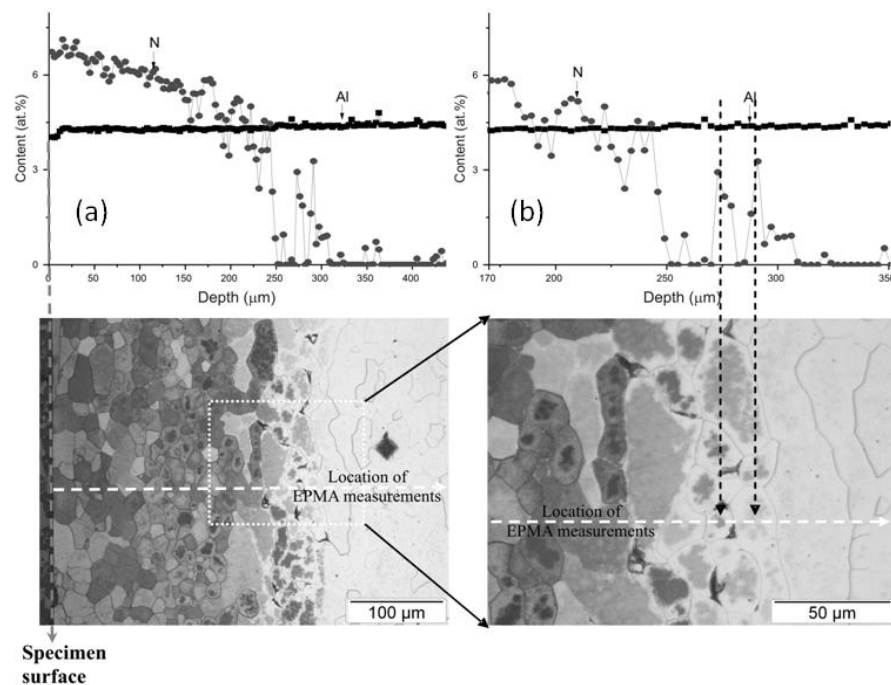


Fig. 2.4: (a) Elemental (N and Al) concentration–depth profiles (EPMA results) together with the optical micrograph of the cross-section analysed showing the location of the EPMA measurements (dashed horizontal line), for the Fe-4.65at.%Al specimen nitrided for 12 + 24 h at 550°C and at $r_N = 0.104 \text{ atm}^{-1/2}$. (b) Similar to (a) but for enlarged portion of (a) as indicated by the dashed rectangle in (a).

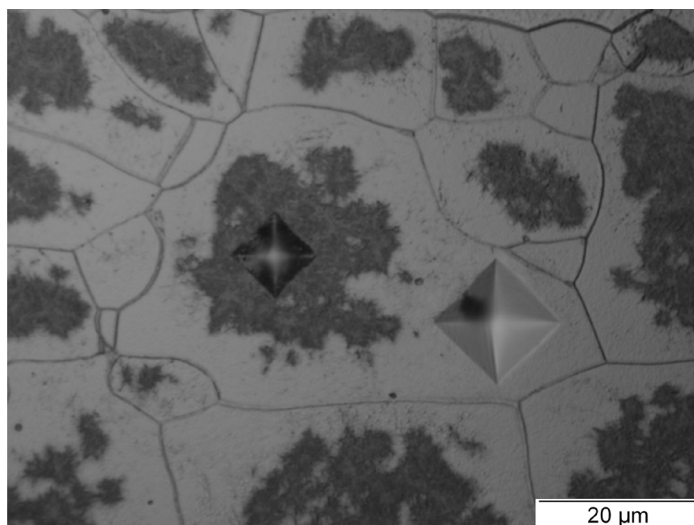


Fig. 2.5: Optical micrograph showing two hardness indentations (micro-Vickers hardness testing performed with the same load, 25 g, and for the same loading time, 10 s) in one grain of Fe-4.65at.%Al specimen nitrided at 550°C and 0.104 atm^{-1/2} for 12 h: dark region at centre of the grain exhibits a much smaller indentation (i.e., possesses a much larger hardness) than white region near to grain boundaries.

suggested that, upon initial saturation of the ferrite grain with nitrogen, a competition occurs between the (slowly starting) hexagonal AlN precipitation and the recombination of nitrogen at grain boundaries to N₂ (gas). Note that nitrogen–ferrite and iron nitrides, not in direct contact with a nitriding medium (i.e. beneath the surface of the specimen), and at normal temperatures and pressures, are always unstable thermodynamically with respect to the dissociation into pure ferrite and nitrogen gas (cf. section 1.7 of chapter 1), which explains the occurrence of porosity (at grain boundaries) in, e.g., (all) iron nitrides prepared by gas nitriding. Hence, before hexagonal AlN precipitation can occur near grain boundaries, all nitrogen close to the grain boundaries has diffused to the grain boundaries and has precipitated there as N₂ (a grain boundary provides (kinetically) an easy site for such precipitation). Only in the centre of the grain can the precipitation of hexagonal AlN occur before (all) dissolved nitrogen has diffused away to the grain boundaries. The precipitation of nitrogen as N₂ at grain boundaries explains the formation of “open grain boundaries” developing upon coalescence of N₂ filled voids along the grain boundaries. These “open grain boundaries” are called “microcracks”. Upon continued nitriding the depletion of nitrogen close to the grain boundaries can be compensated for and as a result fully nitrided grains occur. Due to the tendency for an increase in volume of (fully) nitrided grains, compressive residual stress is generated in the nitrided zone (because of the counteraction of the unnitrided core [42]), which induces closure of the microcracks.

It follows from the above reasoning that, if it is possible to speed up sufficiently the precipitation rate of AlN, then the development of microcracks (due to N₂ precipitation) can be avoided. From the earlier work [21, 37-38] it follows that by employing cold-rolled, instead of recrystallised, relatively low Al content Fe-2at.%Al alloy, then upon nitriding an immediate and fast precipitation of cubic, rocksalt AlN takes place (occurrence of this modification in this case can be explained thermodynamically [38]). So it may be suggested to nitride a deformed (cold rolled) specimen of the current Fe-4.65at.%Al alloy to see if microcrack formation can be avoided.

To this end in this project a cold-rolled Fe-4.65at.%Al specimen was nitrided identically to the corresponding recrystallised specimens. An X-ray diffractogram recorded from the cold-rolled specimen surface of Fe-4.65at.%Al alloy nitrided for 65 h at 550°C and at $r_N = 0.104 \text{ atm}^{-1/2}$ is shown in Fig. 2.6. The possible positions of AlN reflections (according to the JCPDS data base [41]) have also been indicated in Fig. 2.6. The X-ray diffraction result for the nitrided cold-rolled Fe-4.65at.%Al alloy is similar to that observed for the nitrided recrystallised Fe-4.65at.%Al alloy (section 2.3.1) and strikingly different from the results observed in the earlier work on nitrided relatively low Al content Fe-2at.%Al alloy: the presence of hexagonal wurzite AlN phase (see locations marked as HCP1 and HCP2 in Fig. 2.6) is evident and the presence of a minor amount of cubic, rock-salt type AlN precipitates cannot be excluded (the extension of the tail at the high angle side of the α -Fe 110 reflection: see Fig. 2.6 and discussion in section 2.3.1). Apparently the larger driving force (higher supersaturation) in the Fe-4.65at.%Al alloy upon nitriding, as compared to the Fe-2at.%Al alloy, promotes the (kinetically more difficult but thermodynamically more stable [17]) precipitation of hexagonal AlN.

Indeed, the optical micrograph of the nitrided cold-rolled specimen shown in Fig. 2.7a (unetched cross-section) does not show any microcracks, in contrast to the corresponding nitrided recrystallised specimen (Fig. 2.7b), thereby supporting the above hypothesis. As a subtle point it is noted that if the nitriding time is prolonged, then recrystallisation in the unnitrided core of the cold-rolled specimen can occur. Continued nitriding then implies that recrystallised material in the originally fully cold-rolled specimen is nitrided and, (as can be expected, at this late stage) microcracks also occur in the originally fully cold-rolled specimen (see regions indicated by arrows in the optical micrographs of *unetched* and *etched* cross-sections: Fig. 2.8). Moreover, the etching contrast within the grains in the partially recrystallised regions clearly shows that the central portion of the grains is nitrided and that PFZs are present along the grain

boundaries, as observed for the originally recrystallised specimens (see the grains indicated by arrows in Fig. 2.8c for the cold-rolled specimen nitrided for 48 h).

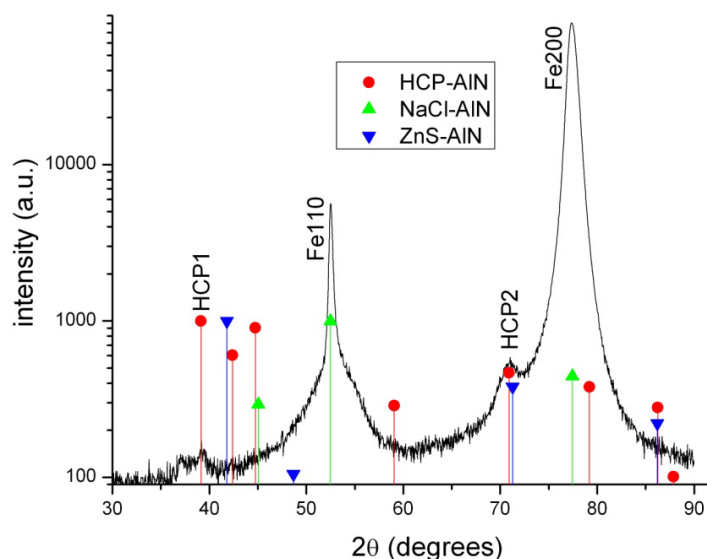


Fig. 2.6: X-ray diffractogram (Co-K α radiation) recorded from the cold-rolled specimen surface of Fe-4.65at.%Al alloy nitrided for 65 h at 550°C and at $r_N = 0.104 \text{ atm}^{-1/2}$. The possible positions of hexagonal (wurzite type) and cubic (zincblende type and NaCl type) AlN reflections (according to Ref. [41]) have also been indicated; the lengths of the line pieces at these locations correspond to the relative intensities for these reflections as expected for the texture-less case.

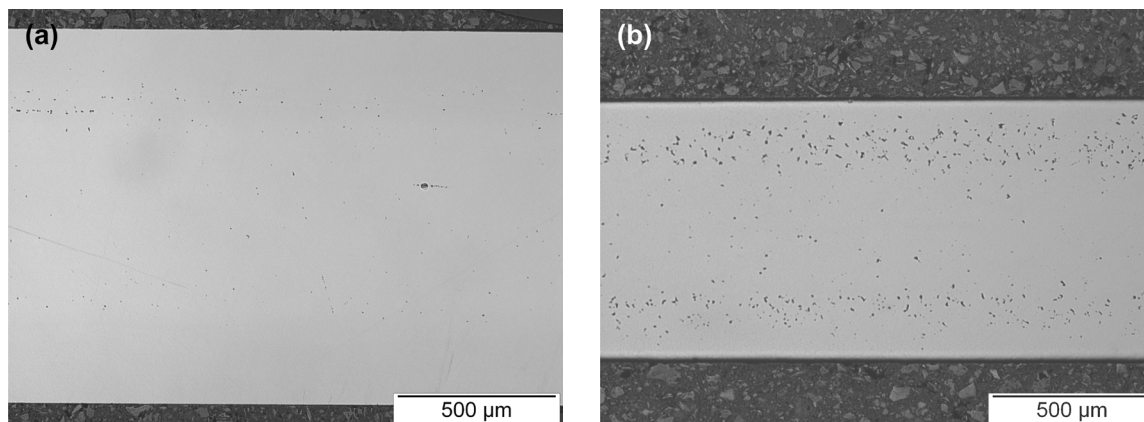


Fig. 2.7: Optical micrograph of the unetched cross-section of (a) cold-rolled and (b) recrystallised Fe-4.65at.%Al specimen nitrided for 15 h at 550°C and at $r_N = 0.104 \text{ atm}^{-1/2}$.

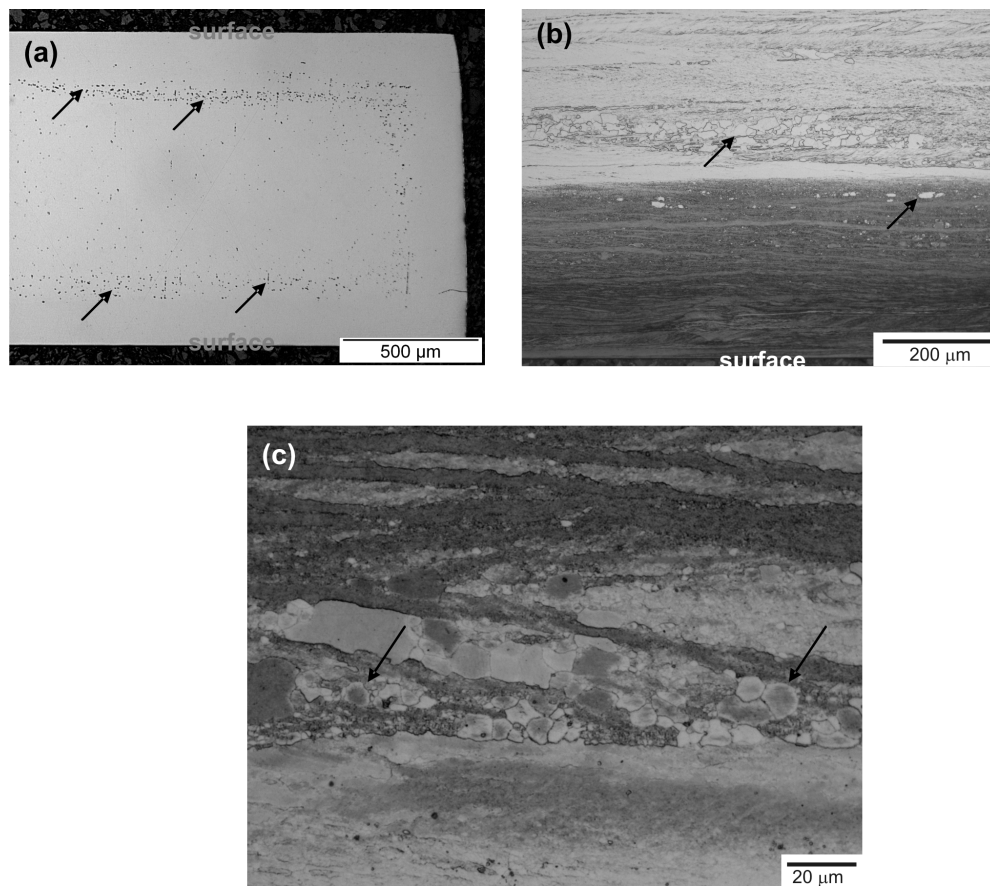


Fig. 2.8: Optical micrographs of (a) unetched and (b) etched cross-section of cold-rolled Fe-4.65at.%Al specimen nitrided for 26 h at 550°C and at $r_N = 0.104 \text{ atm}^{-1/2}$. (c) Optical micrograph of etched cross-section of cold-rolled Fe-4.65at.%Al specimen nitrided for 48 h at 550°C and at $r_N = 0.104 \text{ atm}^{-1/2}$ showing partially recrystallised region at distinct depth (about 400 μm) beneath the surface where the etching contrast indicates that the central part of the grains is nitrided and that precipitate free zones (PFZs) are present along the grain boundaries (see, for example, grains indicated by black arrows (also in micrograph (b)); see also Fig. 2.3b).

2.4 Conclusions

1. Nitriding of Fe-4.65at.%Al leads to the emergence of a high density of microcracks along the original grain boundaries in the ferrite matrix.
2. The microcracks result from the recombination of nitrogen, originally dissolved in the region adjacent to the grain boundaries, to nitrogen gas at the grain boundaries. This diffusion of nitrogen to the grain boundaries and its recombination competes with the relatively slow precipitation of (hexagonal, wurzite type) AlN in the ferritic grains. As a consequence in the centre of the nitrided ferrite grains AlN precipitates occur and precipitate free zones (PFZs) are present along the open grain boundaries (microcracks).

3. Upon continued nitriding, the inward diffusing nitrogen leads to full nitriding of the initially partially nitrated grains and the microcracks are closed under influence of the developing compressive residual stress in the nitrated zone.
4. Accelerating the AlN precipitation process avoids appreciable nitrogen gas development at grain boundaries, as all dissolved nitrogen is rapidly incorporated in AlN precipitates. Thus microcracks cannot develop. Such AlN precipitation rate enhancement is achieved by deformation (cold-rolling) of the Fe-4.65at.%Al specimens.

Unusual nucleation and growth of γ' iron nitride upon nitriding Fe-4.75at.%Al alloy

S. Meka, E. Bischoff, R.E. Schacherl and E.J. Mittemeijer

Abstract

The influence of substitutionally dissolved Al in ferritic Fe-4.75at.%Al alloy on the nucleation and growth of γ' iron nitride ($\text{Fe}_4\text{N}_{1-x}$) was investigated upon nitriding in NH_3/H_2 gas mixtures. The nitrided specimens were characterized employing light microscopy, scanning electron microscopy, transmission electron microscopy, electron probe micro analysis and X-ray diffraction. As compared to the nitriding of pure ferrite ($\alpha\text{-Fe}$), where a layer of γ' develops at the surface, upon nitriding ferritic Fe-4.75at.%Al an unusual morphology of γ' plates develops at the surface, which plates deeply penetrate the substrate. In the diffusion zone, nanosized precipitates of γ' and of metastable, cubic (NaCl-type) AlN occur, having, with the ferrite matrix, a Nishiyama – Wassermann orientation relationship and a Bain orientation relationship, respectively. The γ' plates contain a high density of stacking faults and fine ϵ iron-nitride ($\text{Fe}_2\text{N}_{1-z}$) precipitates, although the formation of ϵ iron nitride is not expected for the employed nitriding parameters. On the basis of dedicated nitriding experiments it could be shown that the unusual microstructural development is a consequence of the negligible solubility of Al in γ' and the obstructed precipitation of the thermodynamically stable, hexagonal (wurtzite-type) AlN in ferrite.

3.1 Introduction

Nitriding of iron-based alloys (steels) is a widely employed thermochemical surface heat treatment to enhance the mechanical and/or chemical properties of ferritic steel components [16, 35, 43-45]. In industrial nitriding processes, the formation of an iron-nitride compound layer at the surface of the nitrided component, also known as “white layer” due to its appearance after etching with “Nital”, is usually not avoidable. The compound layer can have the γ' -Fe₄N_{1-x} (fcc sublattice of Fe) and ϵ -Fe₂N_{1-z} (hcp sublattice of Fe atoms) iron nitrides as main constituents. Such compound layers can have useful anticorrosion properties and can be wear resistant, but also can be brittle which is detrimental. The formation of compound layers on ferritic Fe and Fe-C alloys has been investigated extensively (e.g. see references [1, 46-47]). However, not much is known about the microstructure and growth kinetics of the compound layer on Fe-Me alloys, where Me has affinity for nitrogen. One of the questions to be addressed is whether the alloying elements dissolve in the iron nitride, i.e. occur as a ternary Fe-Me-N compound, or whether they occur as alloying element nitride particles encompassed by the iron nitride.

Precipitation of AlN in ferritic iron-based Fe-Al alloys upon nitriding has been a focal point of research [17, 21, 26-27, 36-38, 48-49]. Little is known, however, about the influence of the substitutionally dissolved Al on the nucleation and growth of the iron nitride: in references [50] and [51] it has been suggested that ferrite-grain boundaries play a decisive role in the development of whisker-like, Al containing γ' iron nitride and that no AlN precipitation in the ferrite matrix would occur. The results presented in this chapter contradict such conclusions. The work presented in this chapter provides a comprehensive investigation of the influence of substitutionally dissolved Al in ferrite on the nucleation and growth of γ' iron nitride.

3.2 Experimental

3.2.1 Specimen preparation

An Fe-4.75at.%Al alloy cast rod having dimensions of 10 mm diameter and 100 mm length was produced by induction melting of elemental granules of iron (purity: 99.98 wt.%) and pieces of aluminium (purity: 99.999 wt.%) under a protective argon atmosphere. The amounts of aluminium and light element impurities in the produced cast were analyzed. The aluminium content was determined by inductively coupled plasma – optical emission spectroscopy (ICP-OES), the nitrogen and oxygen contents were measured applying carrier hot gas extraction and

the sulphur and carbon contents were determined by the combustion method. The thus obtained results of the chemical analysis are shown in Table 3.1.

Table 3.1: Amounts of aluminium and light element impurities for the alloy used in this work

Al (wt.%)	Al (at.%)	O ($\mu\text{g/g}$)	N ($\mu\text{g/g}$)	C ($\mu\text{g/g}$)	S ($\mu\text{g/g}$)
2.35 ± 0.02	4.75 ± 0.02	28 ± 3	< 6	12 ± 2	< 5

The cast rod was cut into pieces, which were cold rolled to produce sheets having a thickness of approximately 1 mm. From these sheets, rectangular specimens with lateral dimensions 10 mm x 15 mm were cut. The specimen surface was ground and polished (final stage 1 μm diamond paste). Such prepared specimens were put into a quartz tube which was evacuated, filled with argon gas and encapsulated. Then the encapsulated specimens were recrystallised at 850°C for 1.5 h. Thereafter the specimens were ultrasonically cleaned in ethanol and subsequently subjected to the nitriding treatment.

To be able to compare the γ' formation in ferrite with and without dissolved Al, pure iron specimens were prepared for nitriding in the same way as described above for the Fe-4.75at.%Al specimens.

Single-crystalline specimens of Fe-4.75at.%Al alloy were obtained by employing the zone melting technique. These specimens were used to find out the possible influence of grain boundaries on the microstructural development upon nitriding.

3.2.2 Nitriding

The specimens were nitrided in a laboratory scale, vertical quartz tube furnace having an inner diameter of 28 mm, equipped with a facility to suspend the specimen in the middle of the furnace, and a water quenching flask, to quench the specimens after completing the nitriding treatment. The furnace temperature was controlled within $\pm 1^\circ\text{C}$ variation and the flow rates of ammonia and hydrogen gases were controlled by MKS mass flow controllers. For the nitriding treatment high purity ammonia (99.99%) and hydrogen (99.999%) gases were used. Before starting, the furnace was purged with nitrogen gas to remove all the oxygen and other adsorbed gases from the furnace walls. After setting the flow rates of ammonia gas (195 ml/min) and hydrogen gas (305 ml/min), the specimen was moved to middle of the uniform temperature zone (550°C) of the furnace. The total gas flow rate of 500 ml/min resulted in a linear gas velocity of 13.5 mm/s, at room temperature, for the quartz-tube furnace used. At this linear gas velocity, a change of the chemical composition of the gas mixture due to dissociation of ammonia can be

neglected. These nitriding conditions correspond with a nitriding potential (cf. [11]), r_N , of $0.82 \text{ atm}^{-1/2}$. For the applied temperature and r_N , γ' iron-nitride formation is expected to occur at the surface of the iron specimen, according to the Lehrer diagram (cf. Fig. 3.1 [14]). Some of the specimens were nitrided employing different nitriding parameters (temperature and nitriding potential) which will be indicated explicitly in this chapter. The nitriding parameters employed in this work for the different nitriding experiments have been listed in Table 3.2 and have also been indicated in the Lehrer diagram (Fig. 3.1).

After completing the nitriding treatment, the specimens were quenched into the water filled quenching flask. In order to minimize the risk of specimen-surface oxidation upon water quenching, before quenching, the water in the quenching flask was purged with nitrogen gas for about 20 min, to remove/minimize the amount of dissolved oxygen in water.

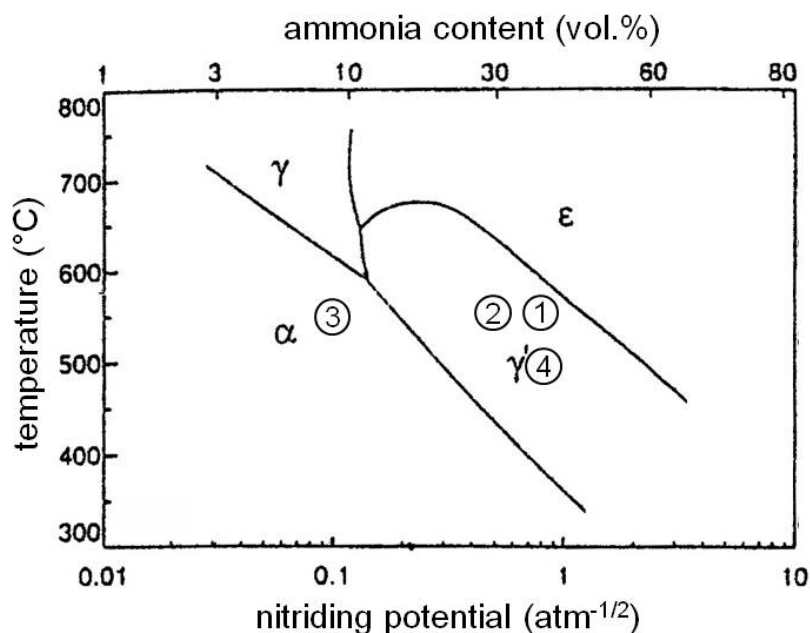


Fig. 3.1: Lehrer diagram (cf. Refs. [11] and [14]) in which the nitriding conditions employed in this work have been indicated with the experiment number as given in column 1 of Table 3.2.

Table 3.2: Nitriding conditions employed for various experiments carried out in this work. The experimental conditions (as indicated by the number in the first column of this table) have also been indicated in the Lehrer diagram shown in Fig.3.1.

experiment	temperature (°C)	NH ₃ flow rate (ml/min)	H ₂ flow rate (ml/min)	nitriding potential (atm ^{-1/2})
1	550	195	305	0.82
2	550	150	350	0.51
3	550	45	455	0.10
4	500	195	305	0.82

3.3 Microstructural characterization

3.3.1 Light optical and scanning electron microscopy

For investigating the microstructure of the nitrided specimens, the nitrided specimens were cut perpendicular to the nitrided surface and embedded in Struers PolyFast. Before embedding, some of the specimen surfaces were covered with a protective electroplated Ni layer by using a Watts bath [52] in order to avoid curvature and damaging of the surface during metallographic preparations. The temperature rise of the specimens during Ni plating (90°C for 8 min) and hot embedding (180°C for 5 min) can lead to the precipitation of metastable α'' -Fe₁₆N₂ from the nitrogen supersaturated ferrite matrix [53-54] (note that the results from XRD and TEM have been obtained from as quenched specimens (i.e. without embedding and Ni plating)). Embedded specimens were prepared for metallographic examination by grinding and polishing (final stage 1 μ m diamond paste) followed by etching with 2 vol.% Nital. Light microscopy investigations were performed on the etched cross-sections of the nitrided specimens using a Zeiss Axiophot microscope equipped with a digital camera (Olympus Color View IIIu). Scanning electron microscopy (SEM) was performed on the nitrided cross-sections using a Jeol JSM-6300F equipped with a field emission gun, applying an accelerating voltage of 3 kV and a working distance of 15 mm.

3.3.2 Transmission electron microscopy (TEM)

To characterize the fine precipitates which developed in the diffusion zone, electron transparent TEM specimens were prepared from selected regions of the nitrided case, by controlled removal

of material by mechanically grinding and dimpling from both sides (faces) of the nitrided specimen. In order to minimize the problems associated with the astigmatism in the electron microscope, caused by the ferromagnetic nature of the specimens, the mass was reduced by using only small pieces (instead of self supporting 3 mm diameter discs) on a special 3 mm diameter disk shaped titanium sample carrier (Bal-Tec). The specimen together with the Ti sample holder was subjected to grinding, polishing and dimpling operations followed by final Ar ion milling (employing a Gatan PIPS-691 apparatus operating at an accelerating voltage of 3–4 kV, a current of 10-12 μA , a milling time of 4-10 h and an angle of ion incidence equal to 8°). During ion milling the specimen stage was cooled by liquid nitrogen.

TEM investigations were performed using a Philips CM 200 microscope operating at 200 kV, equipped with an energy-dispersive X-ray detection system (EDX). The bright field (BF), dark field (DF) images, and the selected area diffraction patterns (SADPs) were recorded using a Gatan CCD camera which is attached to the microscope. The different phases were characterized on the basis of the measured lattice spacings from the SADPs by comparing these with the lattice spacings as expected according to the data available in the ICDD data base [41] (α -Fe: $a = 2.866 \text{ \AA}$, AlN (rock-salt type): $a = 4.071 \text{ \AA}$, AlN (wurtzite type): $a = 3.111 \text{ \AA}$ and $c = 4.978 \text{ \AA}$, γ' iron nitride: $a = 3.797 \text{ \AA}$ and ϵ iron nitride (containing 26.90 at.% of nitrogen [55]): $a = 4.7161 \text{ \AA}$ and $c = 4.3879 \text{ \AA}$; note that these lattice- parameter values pertain to the unit cell adopted for the commonly observed superstructure for ϵ (long range ordering of nitrogen); it holds $a = 3^{1/2}a_{hcp}$ and $c = c_{hcp}$ where a_{hcp} and c_{hcp} refer to the unit cell of the hcp arrangement of Fe atoms).

3.3.3 Electron probe micro analysis (EPMA)

For the determination of elemental (Fe, Al and N) concentrations in the nitrided zone EPMA was performed on the polished cross-sections of nitrided specimens employing a Cameca SX100 microprobe. Measurements were performed using an accelerating voltage of 15 kV and a current of 100 nA. For obtaining the contents of Fe, Al and N at each measured point, the intensities of the characteristic Fe-K β , Al-K α and N-K α radiations were measured and divided by the corresponding intensities measured from internal standard specimens (pure iron, pure aluminium and γ' iron nitride (for nitrogen)). The elemental concentrations were calculated from these intensity ratios applying the $\phi(\rho z)$ approach [56].

3.3.4 X-ray diffraction (XRD)

The XRD measurements were performed using a PANalytical X'pert Multipurpose Diffractometer which was equipped with a graphite monochromator in the diffracted beam, employing Co-K α radiation and Bragg- Brentano geometry. During the measurements, the specimen was rotated around its surface normal to get better crystallite statistics. The peak parameters (full width at half maximum (FWHM) and integral breadth (β)) were determined from the measured diffraction patterns by fitting pseudo – Voigt functions to the measured reflections using the Philips ProFit Ver.1c software.

3.4 Results and discussion

3.4.1 Unusual morphology of γ' iron nitride in the surface region

Light optical micrographs recorded from the cross sections of Fe-4.75at.%Al and pure iron specimens, nitrided for 20 h at 550°C employing a nitriding potential of 0.82 atm^{-1/2}, are shown in Figs. 3.2 a and b, respectively. As compared to the layer-type growth of iron nitride in case of nitrided pure iron (see Fig. 3.2b), an unusual morphology of iron-nitride plates had developed at the surface, which plates deeply penetrated (up to about 400 μ m from the specimen surface) the diffusion zone of the nitrided Fe-4.75at.%Al alloy substrate (see Fig. 3.2a). X-ray diffraction analyses show that the iron nitrides formed are predominantly γ' iron nitride, together with some ϵ iron nitride, which latter nitride is not expected to form for the employed nitriding conditions (cf. section 3.4.4 and Fig. 3.8). Such an unusual morphology of γ' -layer formation has not been observed upon nitriding other binary alloys like Fe-Cr [30], Fe-V [57] and Fe-Ti [58-59].

To find out the possible influence of ferrite-grain boundaries on the development of the unusual plate-like morphology of γ' in Fe-Al alloy, identical experiments were performed on a *single crystal*, Fe-4.75at.% Al alloy. Similar to the polycrystalline specimens, the nitrided single-crystalline specimens also show the development of the unusual plate-like morphology of γ' at the surface with deep penetration of the diffusion zone (see Fig. 3.3 and compare with Fig. 3.2a). This indicates that grain boundaries in the ferritic matrix are not responsible for the unusual morphology of γ' formation in Fe-Al alloys, which is in contradiction with the proposal made in Ref. [51].

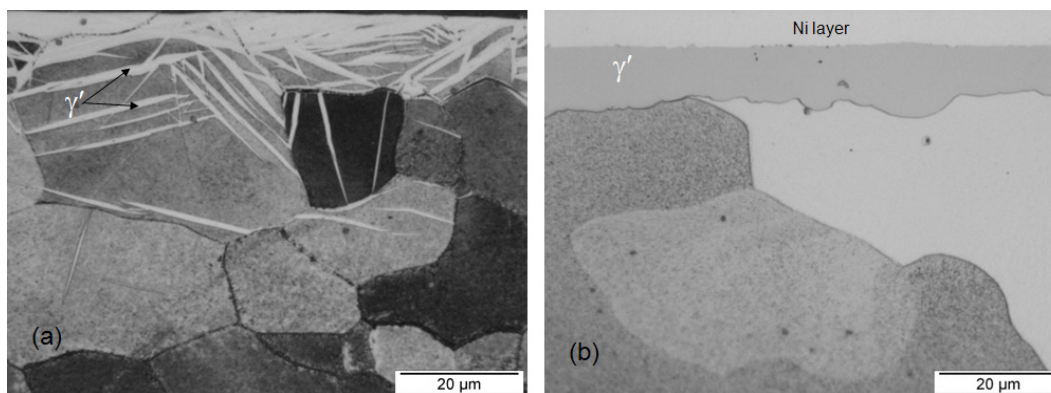


Fig. 3.2: Light optical micrographs recorded from the cross-section of nitrided (550°C , 20 h, $r_{\text{N}} = 0.82 \text{ atm}^{-1/2}$) specimens. (a) Fe-4.75at.%Al alloy specimen showing unusual plate-type morphology of γ' precipitates (b) Pure α -Fe specimen showing closed layer-type γ' iron-nitride formation.

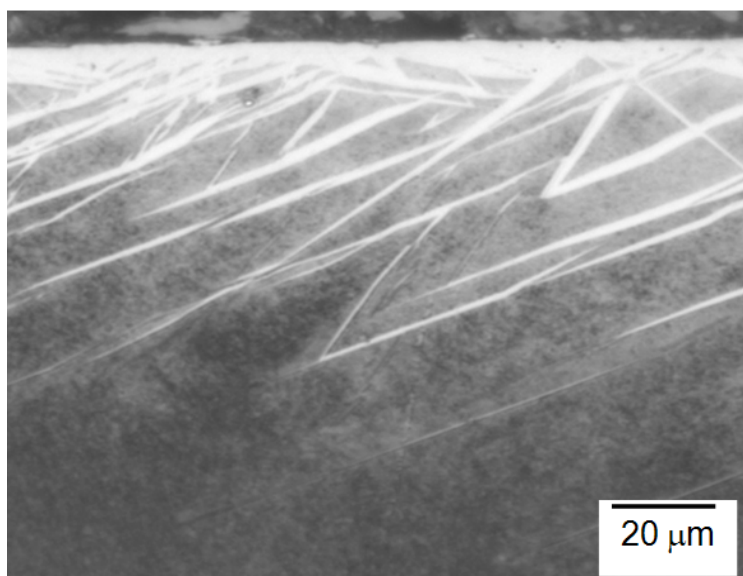


Fig. 3.3: Light optical micrograph recorded from the cross-section of a nitrided (550°C , 20 h, $r_{\text{N}} = 0.82 \text{ atm}^{-1/2}$) *single-crystalline* Fe-4.75at.%Al alloy specimen, showing the plate-like, unusual morphology of γ' , as also observed for the nitrided *polycrystalline* Fe-4.75at.%Al alloy specimens (cf. Fig. 3.2a).

3.4.2 Nano-sized γ' precipitates in diffusion zone

A result of an EPMA elemental line scan made parallel to the specimen surface, crossing some thick γ' plates, is shown in Fig. 3.4, superimposed on the corresponding backscatter electron (BSE) image. Peaks in the nitrogen content are observed at locations where γ' plates occur in the microstructure; the γ' plates appear relatively dark in the BSE image because they contain a significant amount of the light element nitrogen.

The nitrogen content of the ferrite matrix between the γ' plates (diffusion zone) is about 8.5 at.% (Fig. 3.4), which is significantly higher than the nitrogen taken up by the same alloy specimen (5.59 at.%), after homogeneously through nitriding (i.e. all Al has precipitated as AlN) at a much lower nitriding potential, r_N , of $0.104 \text{ atm}^{-1/2}$ such that no iron nitrides develop, as determined by a separate experiment performed in this project (experiment 3 in Table 3.2 and Fig. 3.1). This large amount of nitrogen in the diffusion zone is consistent with, in addition to the AlN precipitates, the presence of (fine) γ' precipitates in the diffusion zone (see further).

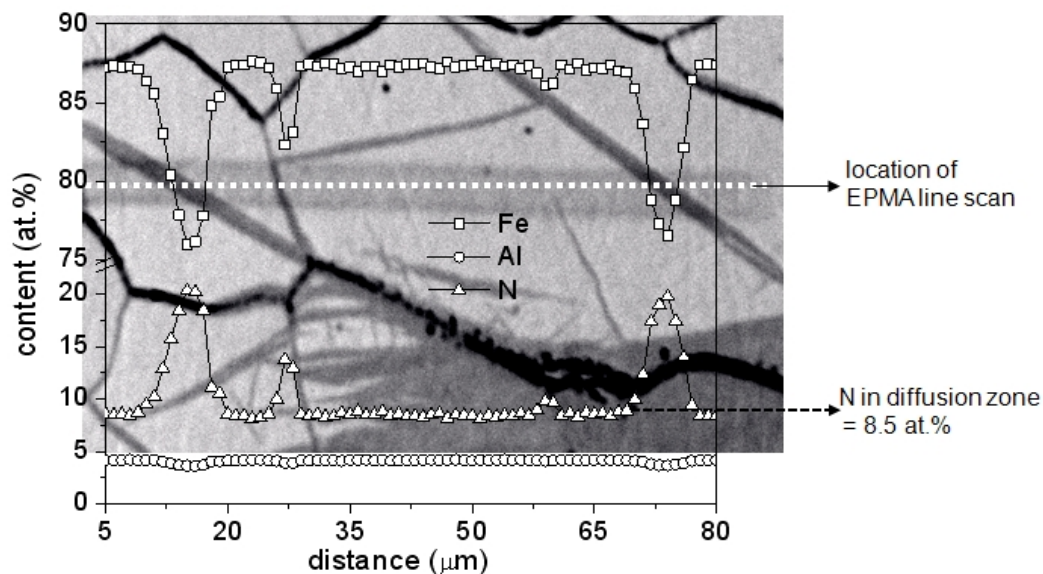


Fig. 3.4: Backscattered electron (BSE) image showing the location of the EPMA elemental line scan (shown with white dotted line) crossing the γ' plates, together with the elemental concentrations for the nitrided (550°C , 20 h, $r_N = 0.82 \text{ atm}^{-1/2}$) Fe-4.75at.%Al alloy. The EPMA line scan was made parallel to the surface at a depth of about $40 \mu\text{m}$. In the BSE image, γ' appears dark due to the high nitrogen content (about 20 at.%). Peaks in the nitrogen content correspond with the EPMA line scan crossing a γ' precipitate (plate).

High magnification SEM micrographs recorded from the cross section of a nitrided Fe-4.75at.%Al alloy specimen (Fig. 3.5) show ultra fine precipitate platelets of AlN (cf. section 3.4.3), γ' (cf. Fig. 3.6) and possibly also of $\alpha''\text{-Fe}_{16}\text{N}_2$ (cf. section 3.3.1) in the diffusion zone surrounding the thick γ' precipitates (see Fig. 3.5b) and also fine γ' precipitates growing from an existing thick γ' plate (shown with white arrows in Fig. 3.5b). In the deeper region of the diffusion zone, growth of fine γ' precipitates from the ferrite-grain boundary had occurred (see Fig. 3.5c).

TEM investigations provided the direct (diffraction) evidence for the development of nano-sized γ' precipitate platelets in the diffusion zone (Fig. 3.6), according to a Nishiyama [60] – Wassermann [61] (N-W) orientation relationship (OR) with the ferrite matrix; $(110)_{\alpha\text{-Fe}} //$

(1-11) γ' and $[001]_{\alpha\text{-Fe}} // [10-1]_{\gamma'}$. Such an OR has also been reported in Ref. [62] for furnace cooled hypoeutectoid Fe-N alloy. In contrast with these results a Pitsch OR (also called inverse N-W OR) was observed in Ref. [63]: $(-101)_{\alpha\text{-Fe}} // (001)_{\gamma'}$ and $[111]_{\alpha\text{-Fe}} // [110]_{\gamma'}$. The latter observation may be due to a different route for γ' precipitation followed in Ref. [63], where γ' precipitated at much lower temperatures ($T < 350^\circ\text{C}$) than in the present work ($T > 500^\circ\text{C}$) via intermediate precipitation of metastable $\alpha''\text{-Fe}_{16}\text{N}_2$.

In the DF image the γ' platelets appear fragmented which suggests the presence of bent/distorted regions in the platelets, which is attributed to the large volume misfit (about 16%) between γ' and ferrite (see also section 3.4.3).

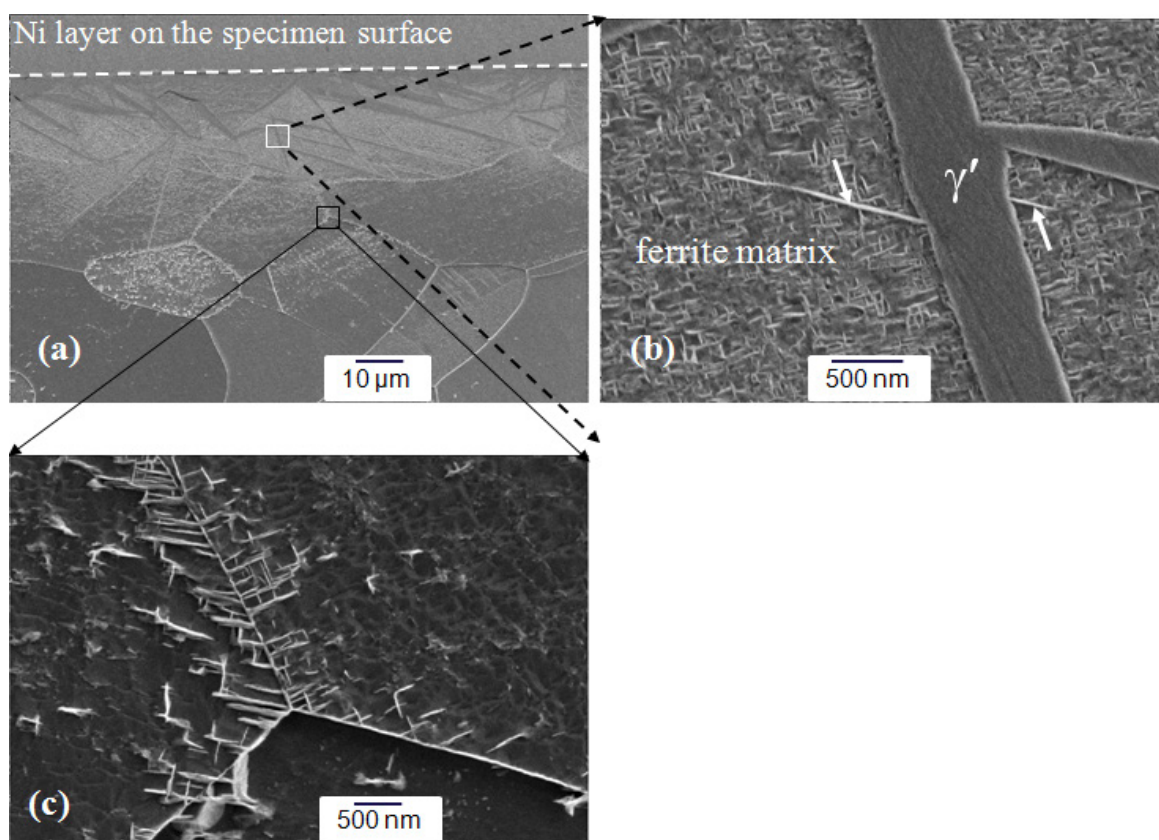


Fig. 3.5: SEM micrographs recorded from the etched cross-section of nitrided (550°C , 4 h, $r_N = 0.82 \text{ atm}^{-1/2}$) Fe-4.75at%Al alloy specimen. Micrographs shown in (b) and (c) are recorded at higher magnification from the regions shown with white and black rectangles in (a). In addition to thick γ' plates, very fine platelets of AlN in the ferrite matrix (cf. section 3.4.3) and fine γ' needles growing from the existing γ' plate (shown with white arrows in (c)) and the grain boundaries can be seen (b).

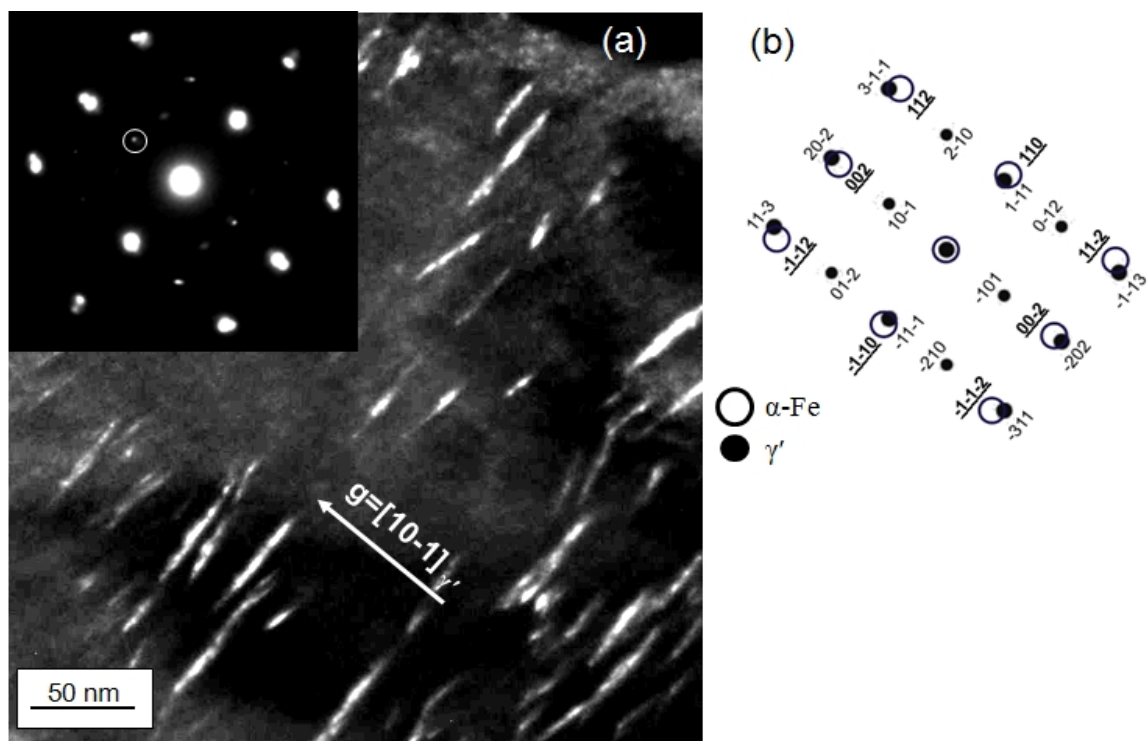


Fig. 3.6: (a) Dark field (DF) TEM image and corresponding selected area diffraction pattern (SADP; zone axis: $[1-10]_{\alpha\text{-Fe}}$ and $[121]_{\gamma'}$) from nitrided (550°C , 20 h, $r_N = 0.82 \text{ atm}^{-1/2}$) Fe-4.75at%Al alloy specimen ($\sim 30 \mu\text{m}$ below the surface); the DF image has been obtained from a 10-1 spot of γ' iron nitride (shown with white circle in the SADP; the direction of the diffraction vector, \mathbf{g} , has been indicated). Very fine platelets (thickness= 2-5 nm and length=10-60 nm) of γ' iron nitride can be observed. Note the variation in brightness along the length of the platelets (see text). Key diagram for the SADP in (a) is shown in (b); in (b) indices for $\alpha\text{-Fe}$ and γ' are indicated with and without underline, respectively. The SADP reveals the Nishiyama -Wassermann orientation relationship between γ' and ferrite; $(110)_{\alpha\text{-Fe}} // (1-11)_{\gamma'}$ and $[001]_{\alpha\text{-Fe}} // [10-1]_{\gamma'}$.

3.4.3 Nano-sized cubic AlN precipitates in diffusion zone

The TEM investigation revealed, next to the nanosized γ' platelets, the occurrence of nanosized (thickness of 2-4 nm) metastable, cubic NaCl-type AlN precipitates in the diffusion zone (Fig. 3.7), exhibiting a Bain OR [64] with the ferrite matrix: $(001)_{\alpha\text{-Fe}} // (001)_{\text{AlN}}$ and $[110]_{\alpha\text{-Fe}} // [100]_{\text{AlN}}$. Similar to the γ' platelets, some regions along the length of the AlN platelets do not show bright contrast in the DF image (Fig. 3.7), which is ascribed to the presence of distorted regions in the platelets. The occurrence of such distorted regions is typical for cubic, NaCl-type nitride (VN [7], CrN [5]) platelets inside the ferrite matrix.

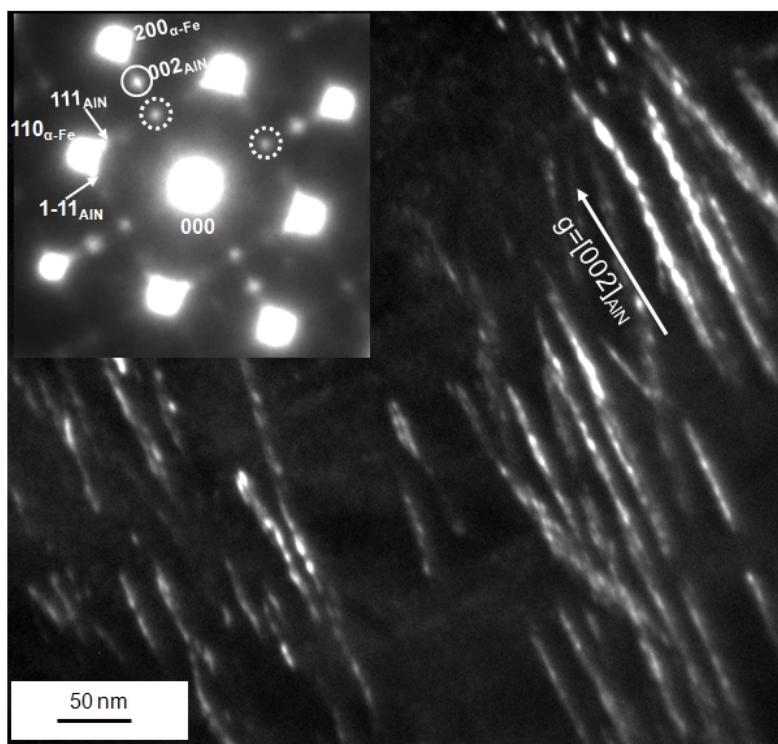


Fig. 3.7: DF-TEM image and corresponding SADP (zone axis: $[001]_{\alpha\text{-Fe}}$) from nitrided (550°C , 20 h, $r_N = 0.82 \text{ atm}^{1/2}$) Fe-4.75at%Al alloy specimen ($\sim 30 \mu\text{m}$ below the surface); the DF image is obtained from a 002 spot of cubic NaCl-type AlN (shown with white circle in the SADP; the direction of the diffraction vector, \mathbf{g} , has been indicated). Very fine platelets (thickness of 3-6 nm) of cubic NaCl-type AlN can be observed. The diffraction spots shown with white dashed circle pertain to 220 reflections of iron oxide, Fe_3O_4 , which develops on the surface of the foil during TEM foil preparation. Note the variation in the brightness along the length of the platelets (see text). In the SADP, the location of the 002 and 111 diffraction spots of cubic, NaCl type AlN reveals the presence of the Bain OR between cubic AlN and ferrite; $(001)_{\alpha\text{-Fe}} // (001)_{\text{AlN}}$ and $[110]_{\alpha\text{-Fe}} // [100]_{\text{AlN}}$.

No evidence was obtained for the presence of the thermodynamically stable, hexagonal wurtzite type modification of the AlN precipitates, whereas TEM investigations performed in this project on the same Fe-4.75at.%Al alloy specimens nitrided at the same temperature (550°C) but at a much reduced nitriding potential ($0.104 \text{ atm}^{-1/2}$, as compared to the present $0.82 \text{ atm}^{-1/2}$; indicated as “3” in Fig. 3.1 and Table 3.2) such that no iron nitrides can form, revealed the formation of the thermodynamically stable hexagonal AlN precipitates, in addition to the metastable, cubic NaCl-type AlN precipitates (cf. section 2.3.1 of chapter 2). The absence of the hexagonal modification of AlN, in case of the alloy nitrided such that γ' iron nitride developed, is attributed to the dislocations generated in the diffusion zone around the γ' plates as a consequence of the large volume misfit between γ' and ferrite: γ' develops before AlN

precipitates (see section 3.4.7) and, as shown in Refs. [21] and [38], dislocations facilitate the precipitation of the metastable, cubic, NaCl type AlN over the precipitation of the thermodynamically stable hexagonal, wurtzite type AlN.

3.4.4 Unexpected formation of ϵ -iron nitride

X-ray diffractograms recorded from the surface of nitrided Fe-4.75at.%Al alloy and from the surface of pure iron specimens show the formation of γ' iron nitride upon nitriding (Fig. 3.8; indexing of ϵ reflections adopting the unit cell of the superstructure (cf. section 3.3.2)). Additionally, the X-ray diffractograms reveal the formation of ϵ iron nitride in nitrided Fe-4.75at.%Al alloy (Fig. 3.8a). This is unexpected as ϵ cannot be formed on pure iron nitrided under identical conditions (cf. Lehrer diagram [14]; indicated as “1” in Fig. 3.1 and Table 3.2) in agreement with the experimental results shown in Fig. 3.8b; indeed such ϵ formation was not observed upon nitriding Fe-Cr [30] and Fe-V [57] alloys under similar conditions. It may be suggested that this unexpected ϵ formation in Fe-4.75at.%Al alloy specimens is due to a shift of the γ'/ϵ phase boundary in the Lehrer diagram [14] due to the (initial) presence of substitutionally dissolved Al. However even upon nitriding a Fe-4.75at.%Al alloy specimen at 550°C with a reduced, nitriding potential, r_N , of $0.51 \text{ atm}^{-1/2}$, i.e. well within the γ' region of the Lehrer diagram (indicated as “2” in Fig. 3.1 and Table 3.2), ϵ formation is observed (Fig. 3.9).

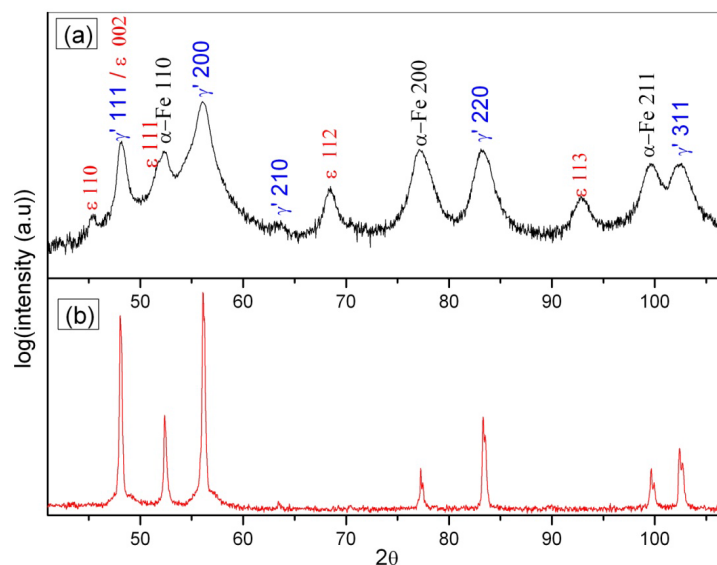


Fig. 3.8: X-ray diffractograms recorded from the surface of the nitrided (550°C, 20 h, $r_N = 0.82 \text{ atm}^{-1/2}$) specimens. (a) Nitrided Fe-4.75at.%Al alloy: Unexpected formation of ϵ and, as compared to the nitrided iron specimen strongly broadened γ' and α -Fe peaks (indexing of ϵ reflections adopting the unit cell of the superstructure (cf. section 3.3.2)). (b) Nitrided pure Fe: No ϵ formation and much less broadened γ' and α -Fe peaks.

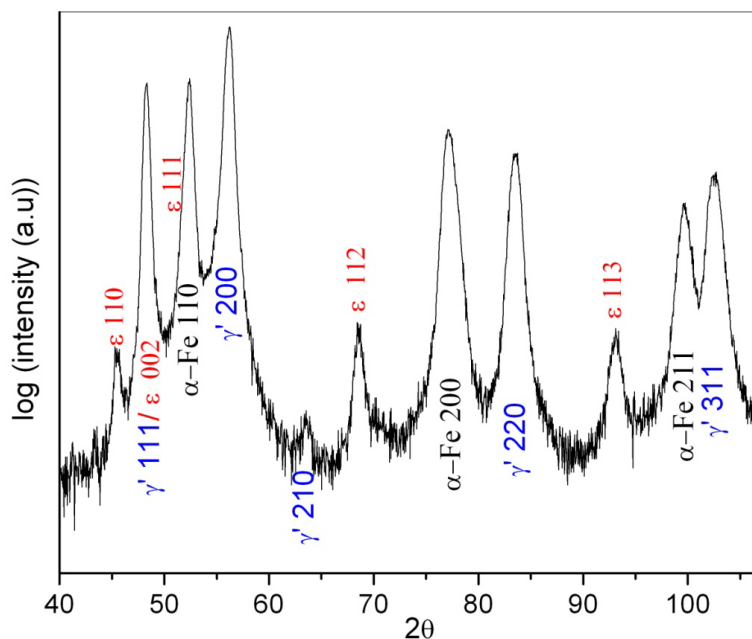


Fig. 3.9: X-ray diffractogram recorded from the surface of nitrided (550°C, 65 h, $r_N = 0.51 \text{ atm}^{-1/2}$) Fe-4.75at.%Al alloy specimen (indexing of ϵ reflections adopting the unit cell of the superstructure (cf. section 3.3.2)). Formation of ϵ occurred although the nitriding conditions are well within the γ' region of the Lehrer diagram (cf. Fig. 3.1).

TEM investigations performed on the surface adjacent γ' plates (i.e. the “older”, first formed γ') indicate the presence of nanosized, platelet-type, ϵ phase regions inside the γ' matrix (Fig. 3.10) with the following OR between ϵ and γ' ; $(11-1)_{\gamma'} // (001)_{\epsilon}$ and $[1-10]_{\gamma'} // [1-10]_{\epsilon}$; i.e. adopting for ϵ the unit cell pertaining to the commonly observed superstructure. If for ϵ the unit cell pertaining to the hcp arrangement of iron atoms is adopted (cf. section 3.3.2), the same OR reads as $(11-1)_{\gamma'} // (001)_{\epsilon}$ and $[1-10]_{\gamma'} // [110]_{\epsilon}$. This OR for ϵ/γ' agrees with the previously reported OR for ϵ/γ' in nitride-compound layers formed on plasma nitrided steel [65].

TEM investigations performed on the γ' phase (plates) in deeper regions of the diffusion zone (30 μm below the surface: i.e. the “younger”, later formed γ') showed no ϵ -phase regions in the γ' plates but the presence of a high density of stacking faults on (111) planes (Fig. 3.11a) as indicated by extensive streaking in the SADP through 111 reflections of γ' parallel to $\langle 111 \rangle_{\gamma'}$ directions (Fig. 3.11b). These observations suggest that the ϵ platelets form in highly faulted γ' phase [66]. Note that, considering the fcc and hcp Fe atom arrangements in γ' and ϵ , respectively, an ordered glide of Shockley partial dislocations along close-packed Fe lattice planes suffices to bring about the fcc \rightarrow hcp transition. Such Shockley partial dislocation glide would lead to the occurrence of an OR as reported here.

No evidence for the presence of AlN inside the γ' iron nitride was found. It will be shown in section 3.4.7 that the formation of the ϵ phase can be promoted by a higher solubility of Al in ϵ than in γ' .

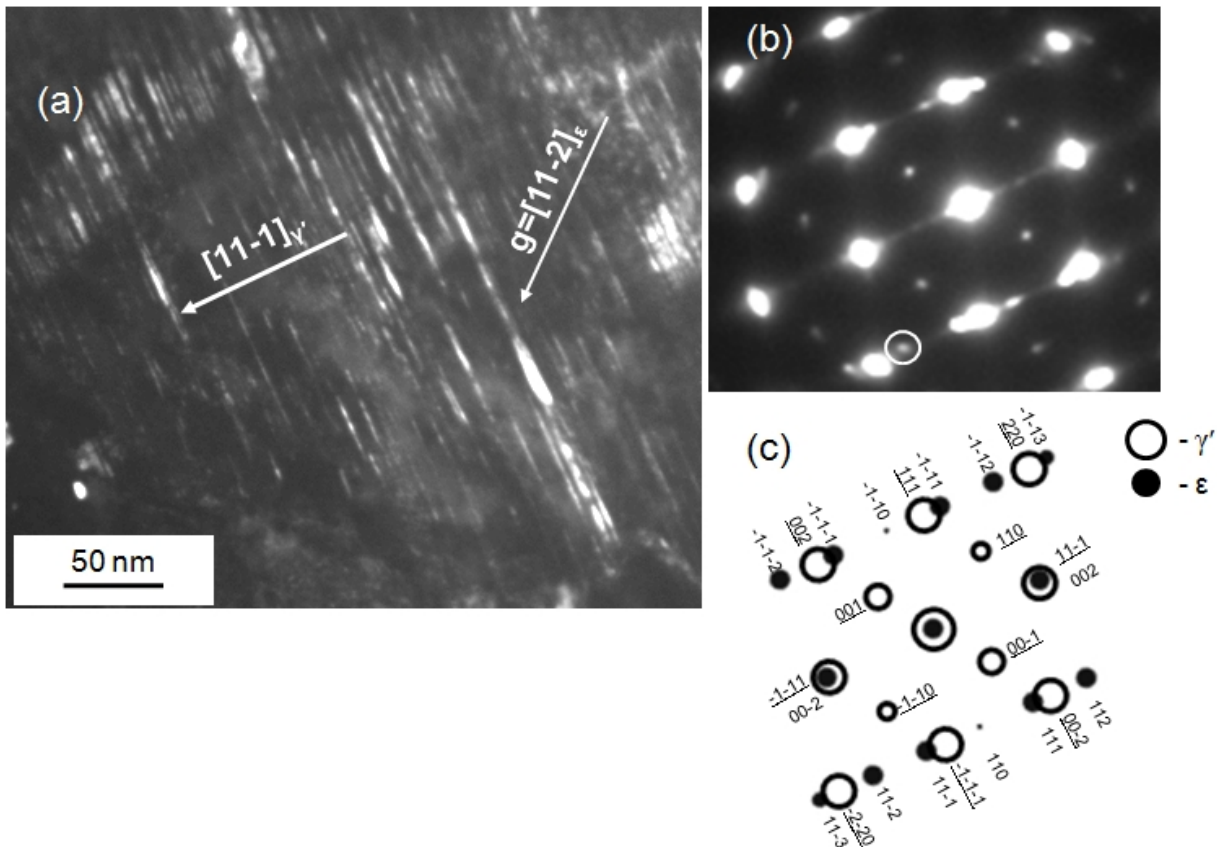


Fig. 3.10: (a) DF-TEM image and corresponding SADP (b) (zone axis: $[1-10]_{\gamma'}$ and $[1-10]_{\epsilon}$) from the near surface region ($\sim 3 \mu\text{m}$ from surface) of nitrided (550°C , 20 h, $r_N = 0.82 \text{ atm}^{-1/2}$) Fe-4.75at%Al alloy specimen showing ϵ iron-nitride platelets along the (111) planes of γ' matrix; the DF image is obtained from a 11-2 spot of ϵ iron nitride (shown with white circle in the SADP; the direction perpendicular to the (111) lattice planes of γ' and the direction of the diffraction vector, \mathbf{g} , have been indicated in the DF). The schematic diffraction pattern is shown in (c); in (c) the indices for γ' and ϵ have been indicated with and without underline, respectively. The SADP indicates the following OR between ϵ and γ' ; $(11-1)_{\gamma'} // (001)_{\epsilon}$ and $[1-10]_{\gamma'} // [1-10]_{\epsilon}$. (indexing of ϵ reflections adopting the unit cell of the superstructure (cf. section 3.3.2)).

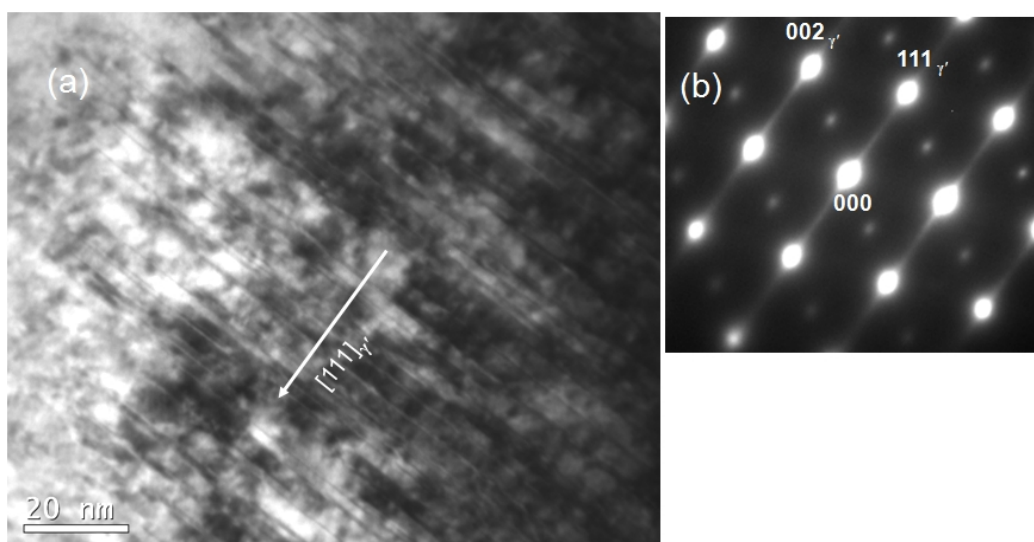


Fig. 3.11: Bright field (BF) TEM image and corresponding SADP (b) (zone axis: $[-110]_{\gamma'}$) from a deeper region ($\sim 30 \mu\text{m}$ below the surface) of nitrided (550°C , 20 h, $r_N = 0.82 \text{ atm}^{-1/2}$) Fe-4.75at%Al alloy specimen. The high density of 111 stacking faults in γ' leads to extensive streaking through 111 reflections of γ' (the direction perpendicular to the (111) lattice planes has been indicated in the BF).

3.4.5 Diffraction-line broadening

Both the γ' and α -Fe X-ray diffraction peaks recorded from nitrided Fe-4.75at.%Al alloy are much more broadened than the corresponding diffraction peaks recorded from nitrided pure iron (Fig. 3.8). The FWHM and β values for the γ' and α -Fe reflections have been gathered in Table 3.3. For the nitrided Fe-4.75at.%Al alloy, (i) the very strong γ' peak broadening can be attributed to the high density of stacking faults in γ' , the nano-sized nature of the γ' precipitates in the ferrite matrix and the large volume misfit (16 %) between the γ' nitride and the ferrite matrix and (ii) the very strong broadening of the ferrite peaks is due to the microstrain introduced into the ferrite matrix by the misfitting nano-sized AlN (section 3.4.3) and γ' platelets (section 3.4.2) (cf. Ref. [67]). Further, the ferrite 200 peak from nitrided Fe-4.75at.%Al alloy is relatively strongly broadened compared to the ferrite 110 and 211 peaks, recognizing the dependence of strain broadening on the length of the diffraction vector [68] (cf. Table 3.3). This is a consequence of the formation of semicoherent, metastable, cubic, NaCl type AlN platelets along (100) planes of the ferrite matrix and the tetragonal nature of the misfit-strain fields [7].

Table 3.3: Full width at half maximum (FWHM) and integral breadth (β) values for γ' and α -Fe diffraction peaks recorded from the surface of a nitrided (550°C, 20 h, $r_N = 0.82 \text{ atm}^{-1/2}$) Fe-4.75at.%Al alloy specimen, a nitrided pure iron specimen and, a doubly nitrided (550°C, 26 h, $r_N = 0.104 \text{ atm}^{-1/2}$ (α -region of Lehrer diagram) + 550°C, 20 h, $r_N = 0.82 \text{ atm}^{-1/2}$ (γ' -region of Lehrer diagram)) Fe-4.75at.%Al alloy specimen.

peak (hkl)	nitrided (550°C, 20 h, $r_N = 0.82 \text{ atm}^{-1/2}$)				doubly nitrided (550°C, 26 h, $r_N = 0.104 \text{ atm}^{-1/2}$) + (550°C, 20 h, $r_N = 0.82 \text{ atm}^{-1/2}$)	
	Fe-4.75at.%Al		pure iron		Fe-4.75at.%Al	
	FWHM (°2 θ)	β (°2 θ)	FWHM (°2 θ)	β (°2 θ)	FWHM (°2 θ)	β (°2 θ)
γ' -111	0.71	0.99	0.11	0.14	0.40	0.54
γ' -200	1.12	1.75	0.11	0.14	0.49	0.65
γ' -220	1.46	1.94	0.18	0.23	0.75	0.99
γ' -311	1.76	2.33	0.23	0.31	0.93	1.14
α -110	0.75	1.24	0.13	0.21	0.45	0.63
α -200	1.50	2.06	0.12	0.21	0.95	1.20
α -211	1.52	2.04	0.17	0.29	0.93	1.24

3.4.6 Role of AlN precipitation

In order to expose the influence of AlN precipitates on the morphology of the γ' precipitates, the following two-step nitriding experiment was performed. A Fe-4.75at.%Al alloy specimen was nitrided for 26 h at 550°C employing a nitriding potential of $0.104 \text{ atm}^{-1/2}$. At these nitriding conditions no iron-nitride formation occurs on the specimen surface, but Al can precipitate within the ferrite matrix as AlN (indicated as “3” in Fig. 3.1 and Table 3.2). The EPMA nitrogen concentration-depth profile measured on the cross-section of this nitrided specimen (Fig. 3.12) indicates that, from the specimen surface, up to the depth of about 100 μm , the nitrogen content in the specimen is well above the “normal” nitrogen content of the alloy (= sum of (i) the nitrogen associated with stoichiometric AlN precipitates, when all Al in the specimen has precipitated as AlN, and (ii) the equilibrium nitrogen solubility of the remaining unstrained ferrite matrix) indicating that, in this depth region, all Al has precipitated as AlN

(Fig. 3.12)². This nitrated specimen was nitrated again for 20 h at 550°C, now employing a nitrating potential of 0.82 atm^{-1/2} (indicated as “1” in Fig. 3.1 and Table 3.2), such that γ' formation can occur in the Fe-4.75at.%Al alloy where all Al has already precipitated as AlN, i.e. no Al is present in dissolved state. The light optical micrograph recorded from the cross-section of such a “doubly nitrated” (first in the α region of the Lehrer diagram and then in the γ' region of the Lehrer diagram) specimen shows the usual layer-type growth of γ' , i.e. as observed for nitrating pure iron (compare Fig. 3.13 with Fig. 3.2b). Moreover, the XRD pattern recorded from the surface of the “doubly nitrated” specimen indicated no ϵ formation (Fig. 3.14) and much less diffraction-line broadening (cf. Figs. 3.8a and 3.14 and see Table 3.3); the presence of (misfitting) nanosized γ' (in addition to AlN) precipitates in the diffusion zone of singly nitrated (550°C, 20 h $r_N = 0.82$ atm^{-1/2}; γ' region of Lehrer diagram) Fe-4.75at.%Al (cf. section 3.4.2) led to distinctly more broadening of the ferrite peaks, as compared to that of doubly nitrated Fe-4.75at.%Al (Table 3.3).

The results obtained for the “doubly nitrated” specimen show that the (initial) presence of substitutionally dissolved Al in the ferrite matrix is responsible for the formation of the unusual plate-like γ' morphology and the appearance of the ϵ phase.

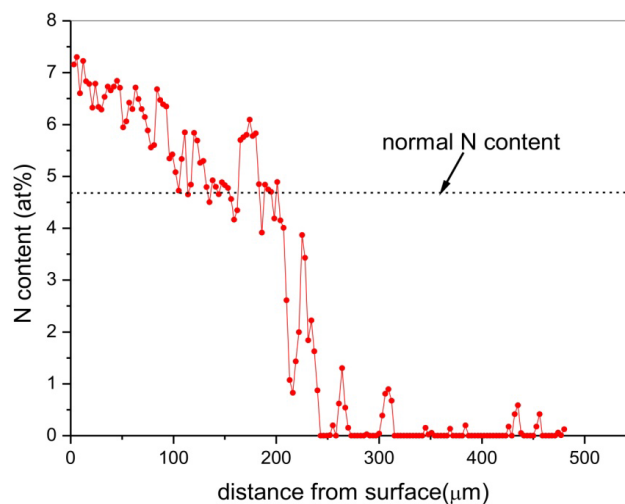


Fig. 3.12: EPMA nitrogen concentration depth profile for the Fe-4.75at.%Al alloy specimen nitrated for 26 h at 550°C and $r_N = 0.104$ atm^{-1/2}. The level indicated by black dotted line is the so-called “normal” nitrogen content (see text).

² The surplus nitrogen (above the normal nitrogen level) is so called “excess” nitrogen which is taken up as (i) additionally dissolved N in the ferrite matrix due to the hydrostatic component of the misfit-strain field around the nitride precipitates, and (ii) adsorbed N at the nitride-precipitate/ferrite-matrix interface (cf. section 1.4 of chapter 1).

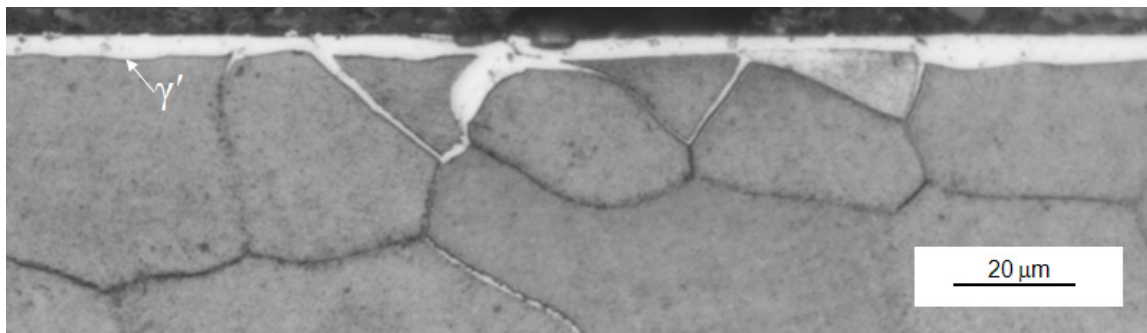


Fig. 3.13: Light optical micrograph recorded from the cross-section of doubly nitrided (550°C , 26 h, $r_{\text{N}} = 0.104 \text{ atm}^{1/2}$ (α -region of Lehrer diagram) + 550°C , 20 h, $r_{\text{N}} = 0.82 \text{ atm}^{1/2}$ (γ' -region of Lehrer diagram)) Fe-4.75at.%Al alloy specimen showing the layer-type growth of γ' as usually occurring upon nitriding pure iron (see Fig. 3.2b).

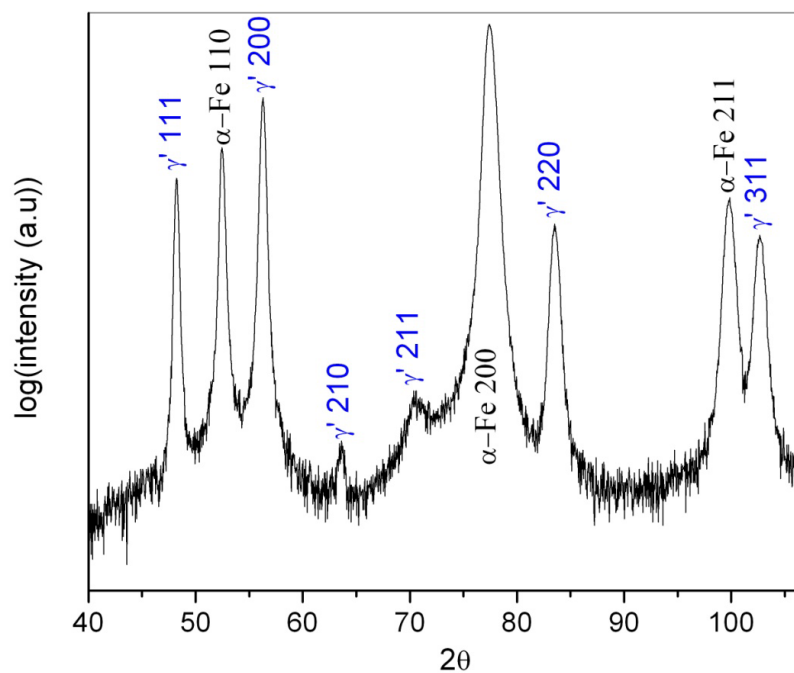


Fig. 3.14: X-ray diffractogram recorded from the surface of doubly nitrided (550°C , 26 h, $r_{\text{N}} = 0.104 \text{ atm}^{1/2}$ (α -region of Lehrer diagram) + 550°C , 20 h, $r_{\text{N}} = 0.82 \text{ atm}^{1/2}$ (γ' -region of Lehrer diagram)) Fe-4.75at.%Al alloy specimen showing absence of ϵ formation and less broadened γ' and α -Fe diffraction peaks (as compared to Fig. 3.8a; cf. Table 3.3).

3.4.7 The negligible solubility of Al in γ'

In order to observe the precipitation sequence of AlN and γ' , a Fe-4.75at.%Al alloy specimen was nitrided for a short time (10 min) at 550°C employing a nitriding potential of $0.82 \text{ atm}^{1/2}$. A light optical micrograph with the superimposed concentration profile determined by an EPMA line scan crossing iron-nitride precipitates is shown in Fig. 3.15. It shows that, before the surface

is fully covered with a nitride layer, nitride, nucleated on the specimen surface, grows into the ferrite matrix, leading to the plate-type nitride precipitate morphology. The EPMA line scan shows that the ferrite matrix between the nitride plates has a negligible nitrogen concentration, indicating that no AlN precipitation has occurred at this beginning stage of nitriding inside the ferrite matrix. Hence, before AlN precipitation takes place, γ' iron nitride precipitates, involving a (simultaneous) incorporation of the Al, originally dissolved in the ferrite matrix, into the developing γ' iron nitride (note the presence of Al at the locations of the iron-nitride plates, see Fig. 3.15).

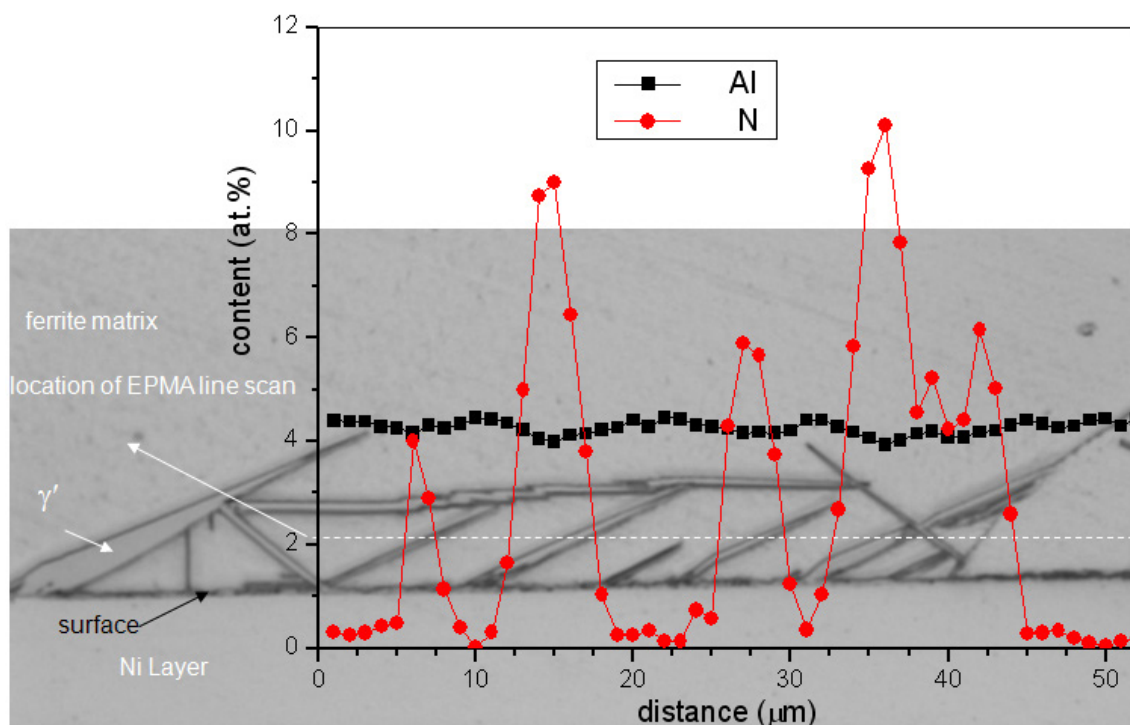


Fig. 3.15: Light optical micrograph showing the location of the EPMA elemental line scan (shown with white dashed line) crossing the γ' plates, together with the elemental concentrations for the nitrated (550°C, 10 min, $r_N = 0.82 \text{ atm}^{-1/2}$) Fe-4.75at.%Al alloy. Peaks in the nitrogen content correspond with the EPMA line scan crossing a γ' precipitate (plate). The ferrite matrix present between the γ' plates contains a very low nitrogen content (less than 0.3 at.%) which indicates that no AlN precipitates have formed inside the ferrite matrix, i.e. γ' has formed with the locally present Al dissolved in it.

The XRD pattern recorded from such short time (10 min) nitrated specimen indicated the occurrence of extra diffraction peaks (other than those due to γ' and α -Fe). These peaks can be ascribed to neither any of the reported iron nitrides, nor Fe-N martensite nor any of the AlN

phases (see Fig. 3.16; extra peaks are shown with arrows). Except for the two less intense extra peaks at the left-hand side of the γ' 111 peak, all other extra peaks are adjacent to γ' peaks and their shifts (to the left or to the right from the nearby γ' peak, see Fig. 3.16) are compatible with the peak shifts expected for stacking faults in fcc crystals [69]: 111 and 220 peaks shift to higher 2θ values, whereas the 200 and 222 peaks shift to lower 2θ values. However, the sharpness and the intensity of the extra peaks adjacent to the “normal” 111 and 200 γ' peaks (the peak intensity of the “normal” γ' 200 peak is even smaller than that of the unknown extra peak adjacent to it) and the presence of the two extra, small peaks at the left-hand side of the γ' 111 peak are incompatible with a simple faulting process. Thus it is suggested that the extra peaks are due to a possible formation of an unknown, metastable Fe-Al-N phase.

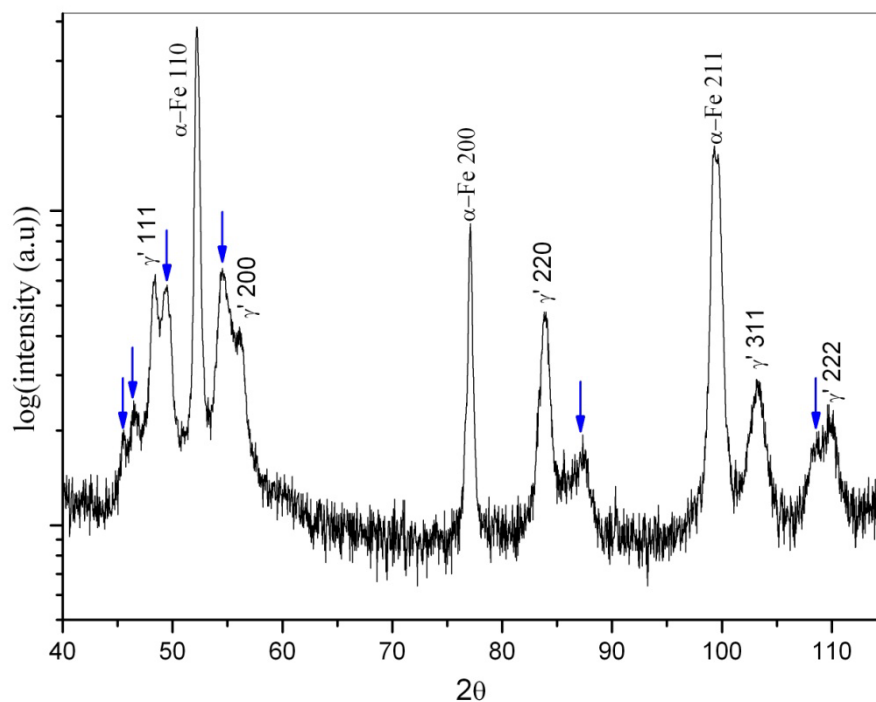


Fig. 3.16: X-ray diffractogram recorded from the surface of short time nitrided (550°C, 10 min, $r_N = 0.82 \text{ atm}^{-1/2}$) Fe-4.75at.%Al alloy specimen. Extra diffraction peaks (shown with arrows) which cannot be indexed according to any of the reported Fe-N and Al-N phases, thus suggesting the possible formation of an unknown metastable Fe-Al-N phase (see text).

The formation of γ' containing Al dissolved in it is difficult (i.e. the solubility of Al in γ' is negligible), which is demonstrated by the following nitriding experiment. Pure iron and Fe-4.75at.%Al alloy specimens were nitrided for 2 h now at the low temperature of 500°C, using a nitriding potential of $0.82 \text{ atm}^{-1/2}$ (indicated as “4” in Fig. 3.1 and Table 3.2). Both X-ray diffractograms recorded from the surface (Fig. 3.17) and light optical micrographs recorded from the cross-section of the nitrided specimens (Fig. 3.18) indicate that for the same nitriding

conditions, a significant amount of γ' has developed on the pure iron specimen, whereas no γ' has developed on the Fe-4.75at.%Al alloy specimen. If Al can dissolve in γ' , then the formation of γ' is also expected to occur for the Fe-4.75at.%Al alloy. Evidently, this is not the case. The driving force for the nucleation of a certain phase is likely to be reduced if an element which has no solubility in that phase is forced (because of lack of atomic mobility; here Al at 500°C) to dissolve under para-equilibrium conditions.

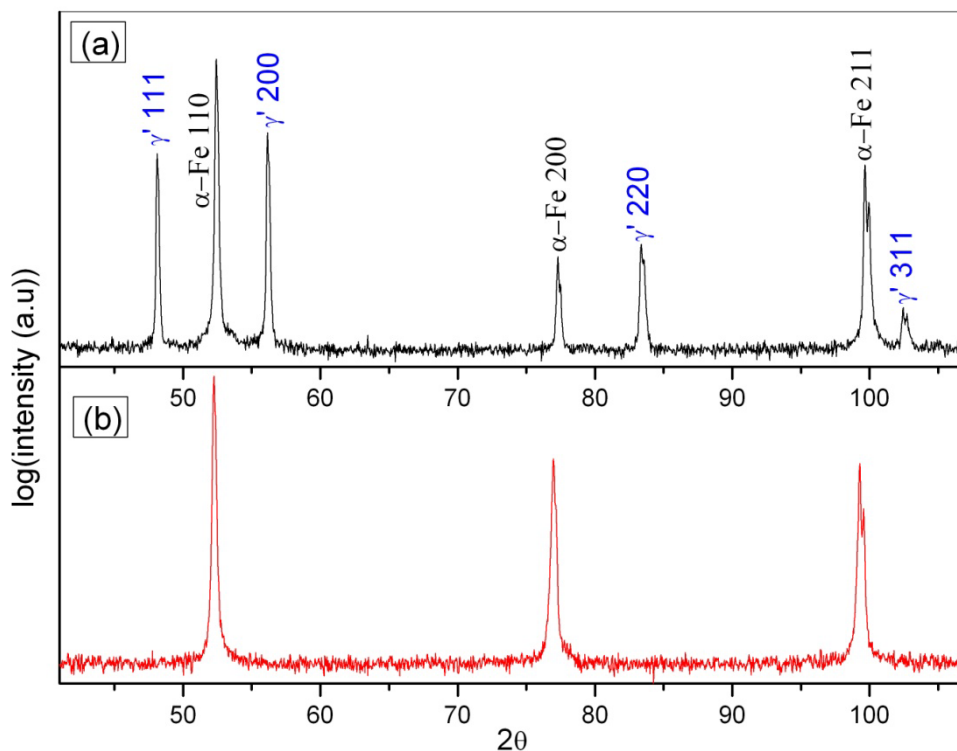


Fig. 3.17: X-ray diffractograms recorded from the surface of the nitrided (500°C, 2 h, $r_N = 0.82 \text{ atm}^{-1/2}$) specimens. (a) Nitrided pure α -Fe showing the formation of γ' . (b) Nitrided Fe-4.75at.%Al alloy showing no γ' formation.

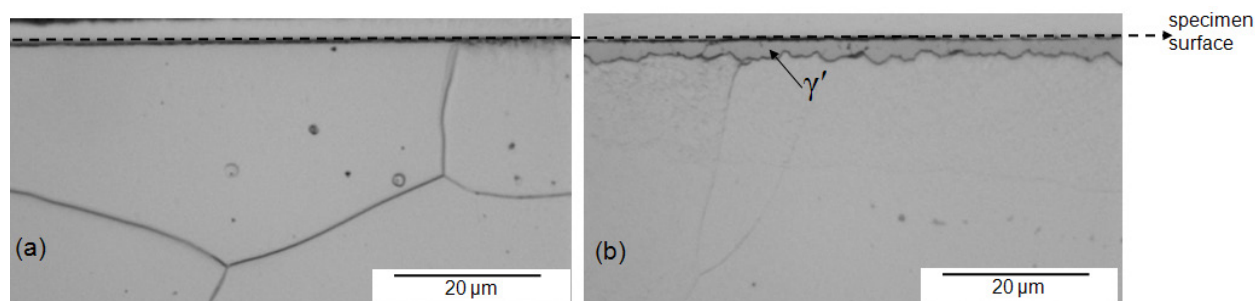


Fig. 3.18: Light optical micrographs recorded from the cross-sections of nitrided (500°C, $r_N = 0.82 \text{ atm}^{-1/2}$, 2 h) specimens. (a) Nitrided Fe-4.75at.%Al alloy, showing no γ' formation on specimen surface. (b) Nitrided pure α -Fe, showing a γ' layer formed on the specimen surface.

The solubility of Al in iron nitrides has been discussed controversially in the literature: it has been reported that Al cannot dissolve in both γ' and ϵ iron nitride [70], whereas it has also been reported that both γ' and ϵ iron nitrides can dissolve up to 40 at.% Al [71] and a recent claim of successful synthesis of a ternary nitride, AlFe_3N (Al substituted for Fe on γ' lattice) [72] was found to be invalid [73] and it is concluded that Al has negligible solubility in γ' .

The nitrogen content of the iron-nitride phase developed at 550°C on Fe-4.75at.%Al was measured by EPMA point analysis on thick plates (so that the volume probed by EPMA is contained by the nitride phase) for different nitriding times; see Fig. 3.19. It follows that upon prolonged nitriding, the nitrogen content of the nitride increases, which is compatible with the formation of nanosized ϵ precipitates inside the γ' plates (see section 3.4.4). It may be suggested that Al can relatively easily dissolve in ϵ rather than in γ' . In such a situation Al stabilizes the ϵ phase.

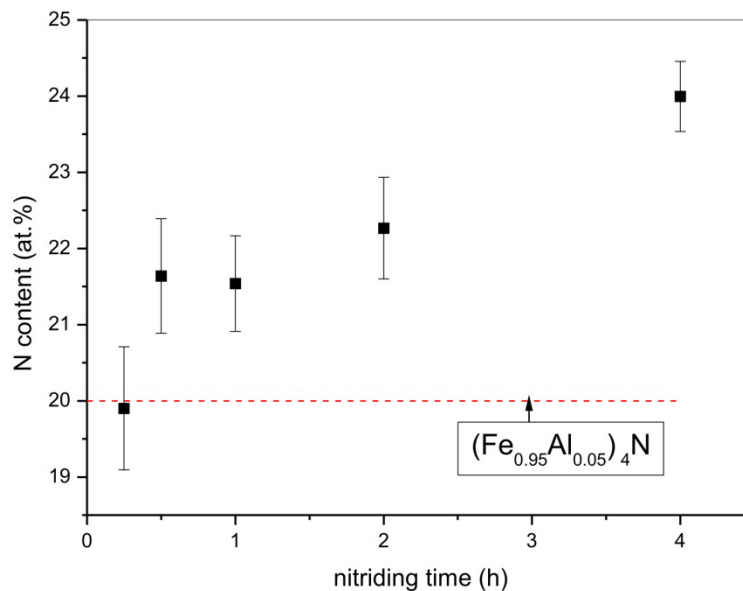


Fig. 3.19: Nitrogen content of the iron-nitride phase as measured by EPMA for the Fe-4.75at%Al alloy specimens nitrided (550°C, $r_N = 0.82 \text{ atm}^{-1/2}$) for different times. At the start of nitriding the nitrogen content of the iron-nitride phase is about 20 at.% which is as expected for pure γ' . Upon continued nitriding the nitrogen content increases which is ascribed to the formation of ϵ phase inside γ' phase.

3.5 General discussion: mechanism of γ' formation in Fe-Al alloy

The precipitation of the thermodynamically stable, hexagonal (wurtzite type) AlN in particular in a recrystallised ferrite matrix is difficult, owing to its large volume misfit with ferrite [21, 38, 49]. Further, nitrogen dissolved in ferrite tends to combine to N_2 (gas) molecules at sites of easy

nucleation, as grain boundaries, which leads to Gibbs energy reduction [11]. Hence, for recrystallised Fe-Al alloys, upon nitriding a competition between the precipitation of hexagonal (wurtzite type) AlN, from dissolved Al and dissolved nitrogen, and the diffusion of dissolved nitrogen to the grain boundaries occurs [49]. This leads, for nitriding under conditions that no γ' iron nitride can develop (see below), to AlN precipitation within the interior of the ferrite grains together with the formation of N₂ gas filled voids along grain boundaries surrounded by nitrogen depleted regions [49].

In the case, where Fe-4.75at.%Al alloy is nitrided under conditions which allow the formation of γ' , a competition between the precipitation of AlN and the precipitation of γ' occurs. As γ' has negligible solubility for Al, precipitation of γ' gets delayed (as well as the precipitation of AlN; see above) as it needs either an Al partitioning in the ferrite matrix to form Al free γ' or the γ' is forced to nucleate and grow under incorporation of Al (which process in any case has a low driving force [74])³. Due to the delay in the precipitation of both AlN and γ' , the inwardly diffusing nitrogen can deeply penetrate the specimen, leading to a large nitrogen supersaturation of the ferrite matrix up to certain depth from the specimen surface. Such large nitrogen supersaturation in the ferrite matrix eventually forces the γ' to precipitate and grow with Al dissolved in it, leading to the unusual morphology of γ' with plates deeply penetrating the substrate. Due to the difficulty in precipitation of Al containing γ' , at early stages an unknown metastable Fe-Al-N phase could occur. The unexpected formation of ϵ in the originally pure γ' plates may be derived from a higher solubility of Al in ϵ than in γ' .

Such unusual morphology of γ' formation and the unexpected formation of ϵ do not occur for nitrided Fe-Cr [30], Fe-V [57] and Fe-Ti [58-59] alloys. For these alloys the much faster precipitation of the alloying element nitrides, CrN, VN and TiN, allows precipitation of γ' only after all alloying element has precipitated as alloying element nitride, i.e., in these cases no such high nitrogen supersaturation of the ferrite matrix occurs as happens in Fe-Al alloys. Consequently, the unusual morphology of γ' precipitation is also expected upon nitriding of Fe-Si and Fe-Mo alloys where precipitation of silicon nitride and molybdenum nitride is difficult (due to their large volume misfit with the ferrite matrix) and accordingly delayed as well [77-78].

³ This phenomenon parallels the suppression or delayed precipitation of cementite from austenite/martensite in bainitic steels containing Si/Al due to the negligible solubility for Si and Al in cementite and the difficulty in partitioning of Si/Al in the austenite/martensite. For more details see Refs. [75-76]

Fundamental understanding of the influence of various alloying elements on the nucleation and growth of iron nitrides, as provided by this chapter, leads to a new approach for designing the chemistry of nitriding steel and for the choice of the nitriding parameters to control the microstructure of the nitrided layers. Having strong nitride forming alloying elements in steel together with alloying elements which cannot form alloying element nitrides and have negligible solubility in iron nitrides allows avoidance, or modification of the morphology and microstructure, of iron-nitride-based compound layers. In particular obstructing the formation of the outer, brittle, iron-nitride compound layer can be beneficial in many industrial applications.

3.6 Conclusions

1. Upon nitriding Fe-4.75at.%Al alloy specimens at a temperature and at a nitriding potential which allow the formation of γ' iron nitride, an unusual plate-type morphology develops for the γ' precipitates formed at the surface, which plates penetrate deeply into the diffusion zone, whereas upon nitriding pure iron, Fe-Cr, Fe-V and Fe-Ti alloys, the usual layer-type γ' develops at the surface. In addition to these thick γ' iron-nitride plates, nanosized γ' platelets develop in the ferrite matrix. The nanosized γ' precipitates have a Nishiyama-Wassermann orientation relationship with the ferrite matrix. Local lattice distortions/bending occur in the nanosized γ' platelets, as a consequence of the large volume misfit between γ' and ferrite. The γ' plates contain a high density of stacking faults.
2. Single-crystalline specimens show similar results as polycrystalline specimens, indicating that grain boundaries in the ferrite matrix play no role in the unusual microstructure development.
3. Instead of the thermodynamically stable hexagonal (wurtzite type) AlN, the metastable, cubic, NaCl-type AlN occurred in the ferrite matrix as fine platelets exhibiting a Bain orientation relationship with the ferrite matrix. The emergence of the cubic modification of AlN is ascribed to its easy precipitation on dislocations which are generated by the precipitating γ' as a consequence of its large volume misfit with the matrix.
4. Upon nitriding Fe-Al alloy the formation of γ' iron nitride is difficult due to the negligible solubility of Al in γ' . The difficulty in the precipitation of both the thermodynamically stable hexagonal (wurtzite type) AlN and the γ' iron nitride, allows the absorbed nitrogen to diffuse deeply into the specimen leading to a high nitrogen supersaturation inside the ferrite matrix. This high supersaturation eventually forces the γ' to precipitate (under

incorporation of the locally present Al) leading to the development of the unusual plate-like morphology of γ' . In the remaining ferrite matrix, the cubic AlN precipitates thereafter.

5. The unexpected formation of ϵ in the originally pure γ' plates upon nitriding Fe-Al alloy is ascribed to a solubility of Al in ϵ higher than in γ' and the high tendency to planar faulting of γ' . The orientation relationship of ϵ and γ' is given by $(11-1)_{\gamma'} // (001)_{\epsilon}$ and $[1-10]_{\gamma'} // [1-10]_{\epsilon}$ (adopting for ϵ the unit cell pertaining to the commonly observed superstructure), which OR can be conceived as resulting from glide of Shockley partial dislocations along close packed Fe lattice planes.
6. The results of this work suggest that iron-nitride-based compound layers can either be avoided or morphologically and microstructurally modified by incorporating, in dissolved state, next to strong nitride forming alloying elements, weak or not nitride forming alloying elements in the steel matrix.

Unusual precipitation of amorphous silicon nitride upon nitriding Fe-2at.%Si alloy

S. Meka, K.S. Jung, E. Bischoff and E.J. Mittemeijer

Abstract

Silicon-nitride precipitation in ferritic Fe-2at.%Si alloy was investigated upon nitriding in NH_3/H_2 gas mixtures, using, for microstructural characterization, light microscopy, hardness measurements, scanning and transmission electron microscopy, X-ray diffraction and electron-probe microanalysis. Surprisingly, an ideally weak nitriding behaviour occurs upon nitriding *thick* (1 mm) recrystallised Fe-2at.%Si alloy specimens. This phenomenon can be attributed to the onset of silicon-nitride precipitation only after a certain degree of nitrogen supersaturation has been established *at all depths* in the specimen. Silicon-nitride precipitates form inside the ferrite grains and also along the ferrite-grain boundaries. The precipitates are amorphous and have a stoichiometry of Si_3N_4 . The amorphous nature of the tiny precipitates has a thermodynamic origin. The nitride precipitation occurs very slowly due to a very large volume misfit of the nitride with the matrix. An anomalous non-monotonous hardness change occurs with increasing nitriding time, which was ascribed to the initially fully elastic accommodation of precipitate/matrix misfit. The nitrogen uptake rate increases upon continued nitriding as the result of “self-catalysis”. The possible, favourable application of amorphous silicon-nitride precipitates as grain-growth inhibitors in the production of grain-oriented electrical steel was discussed.

4.1 Introduction

Nitriding is a widely employed thermochemical surface treatment to enhance the mechanical (fatigue and wear) and chemical (corrosion) properties of ferritic steel components [16, 35, 43-45]. The presence of alloying elements, with chemical affinity for nitrogen, induces a complex nitriding behaviour. Therefore, nitriding studies on simple, iron-based binary alloys, such as Fe-Al [27, 38, 49], Fe-Cr [25, 79] and Fe-V [6, 80], and even, mostly recently, some ternary alloys, such as Fe-Cr-C [31] and Fe-Cr-Al [8-9], have been carried out, in particular to investigate how a substitutionally dissolved alloying element with affinity for nitrogen reacts with interstitially dissolved nitrogen in the ferrite matrix [81].

Presently, Si is not deliberately added to steel to enhance the properties of steel upon nitriding. However, steels usually contain Si as it is one of the principal de-oxidizers for steel melts and also Si is an important alloying element in TRIP, bainitic and electrical steels [82-83]. Hence, it is important to understand fundamentally the nucleation and growth of silicon nitride upon nitriding ferritic steels.

A significant thermodynamic, chemical driving force exists for the precipitation of silicon nitride upon nitriding. Thus silicon should be considered as a strong nitride former and (ideally) strong nitriding kinetics are expected (for a discussion on strong, moderate and weak Me-N interaction/kinetics (Me=dissolved alloying element) in a ferrite matrix, see Ref. [21]). Little is known about the precipitation of silicon nitride upon nitriding Fe-Si alloys. The work performed until now is of fragmentary nature [18, 20, 34] and, moreover, the results reported partly do not agree: in Ref. [34] the development of only crystalline silicon nitride precipitates was reported, whereas in much later work [18] it was demonstrated that the developed silicon-nitride precipitates are *amorphous* and of the composition Si_3N_4 . It was shown in Ref. [20] that the precipitation of silicon nitride occurs much faster in a deformed ferrite matrix than in a recrystallised ferrite matrix.

The present study combines microstructural analysis with a description of the precipitation kinetics for the gaseous nitriding of an Fe-2at.%Si alloy. Strikingly unusual phenomena for the nitriding of a binary Fe-Me alloy have been observed and discussed. As a result a first, comprehensive picture has been obtained for the nitriding behaviour of an iron-based Fe-Si alloy.

4.2 Experimental details

4.2.1 Specimen preparation

An Fe-2at.%Si alloy cast rod, having dimensions of 10 mm diameter and 100 mm length, was produced by induction melting of elemental granules of iron (purity: 99.98 wt.%) and pieces of silicon (purity: 99.999 wt.%) under a protective argon atmosphere. The amounts of silicon and light element impurities in the produced cast were analyzed. The silicon content was determined by inductively coupled plasma – optical emission spectroscopy (ICP-OES), the nitrogen and oxygen contents were measured applying carrier hot gas extraction and sulphur and carbon contents were determined by the combustion method. The thus obtained results of the chemical analysis are shown in Table 4.1.

Table 4.1: Amounts of silicon and light element impurities in the cast Fe-2at.%Si alloy.

Si (wt.%)	Si (at.%)	N ($\mu\text{g/g}$)	O ($\mu\text{g/g}$)	S ($\mu\text{g/g}$)	C ($\mu\text{g/g}$)
1.03 \pm 0.02	2.03 \pm 0.04	< 5	67 \pm 10	< 10	20 \pm 2

The cast rod was cold rolled to produce sheets having a thickness of approximately 1 mm. From these sheets, rectangular specimens with lateral dimensions 10 mm x 15 mm were cut and the surface of the specimens was ground and polished (final stage with 1 μm diamond paste). Such prepared specimens were placed into a quartz tube which was evacuated, filled with argon gas and encapsulated, and subsequently annealed at 750°C for 2 h to recrystallize the specimens. Thereafter the specimens were ultrasonically cleaned in ethanol and subjected to the nitriding treatment.

4.2.2 Nitriding and denitriding

The specimens were nitrided in a laboratory scale, vertical quartz tube furnace having an inner diameter of 28 mm, equipped with a facility to suspend the specimen in the middle of the furnace with the help of a quartz fibre. The furnace temperature was controlled within 1°C variation. For the nitriding treatment high purity ammonia (99.99 vol.%) and hydrogen (99.999 vol.%) gases were used. After setting the required flow rates of ammonia gas (45 ml/min) and hydrogen gas (455 ml/min), the specimen was suspended in the uniform temperature zone of the furnace (580°C). The total gas flow rate of 500 ml/min corresponds with a linear gas velocity of 13.5 mm/s at room temperature, for the quartz-tube furnace used. At this linear gas velocity, a change

of the chemical composition of the gas mixture due to the dissociation of ammonia can be neglected. These nitriding conditions result in a nitriding potential (r_N) of $0.104 \text{ atm}^{-1/2}$ [11]. At the applied temperature (580°C) and r_N ($0.104 \text{ atm}^{-1/2}$), no iron nitrides can develop upon nitriding pure iron, according to the Lehrer diagram [14]. After completing the nitriding treatment, the specimens were quenched into a water filled quenching flask. Denitriding of the nitrided specimens was performed in a similar way as nitriding but at a temperature of 450°C in flowing hydrogen gas (500 ml/min). At these denitriding conditions silicon nitride is stable, whereas nitrogen interstitially dissolved in the ferrite is removed from the specimen.

4.3 Microstructural characterization

4.3.1 Light microscopy and scanning electron microscopy

For investigating the microstructure, the nitrided specimens were cut perpendicular to the nitrided surface and hot embedded in Struers PolyFast. Before embedding, all specimens were stored at room temperature for about 3 days. During embedding, the specimen together with the embedding material (Polyfast) was heated for 5 min at 180°C followed by cooling to room temperature with a cooling rate of about $50^\circ\text{C}/\text{min}$. During the preceding storage at room temperature and during this subsequent heat treatment precipitation of $\alpha''\text{-Fe}_{16}\text{N}_2$ can occur in the nitrogen supersaturated ferrite which leads to microstrain and hardness increase [53-54]. This hardness increase is taken into account in the discussion given in section 4.8. The embedded specimens were prepared for metallographic examination by grinding and polishing (finishing with $1 \mu\text{m}$ diamond paste) followed by etching with 2 vol.% Nital. Light microscopy investigations were performed using a Zeiss Axiophot microscope equipped with a digital camera (Olympus Color View IIIu). Scanning electron microscopy (SEM) investigations were carried out using a Jeol JSM-6300F microscope equipped with a field emission gun and employing an accelerating voltage of 3 kV and a working distance of 15 mm.

4.3.2 Transmission electron microscopy

In order to characterize the fine nitride precipitates developing upon nitriding, electron transparent TEM foils were prepared. Discs of 3 mm diameter were stamped with a mechanical punch from sheets produced by removing material mechanically from both sides (faces) of the nitrided specimen such that the depth range 125-140 μm below the specimen surface became available for investigation (i.e. subsequent foil preparation). These discs were subjected to

polishing and dimpling operations followed by final thinning employing Ar ion milling (Gatan PIPS-691). For ion milling an accelerating voltage of 3-4 kV, a current of 10-12 μA , a milling time of 4-10 h and an angle of ion incidence of 8° were used and the specimen stage was cooled by liquid nitrogen.

Some of the TEM specimens were prepared by the jet electro polishing technique using a Struers Tenupol-3 apparatus, employing a bath composition of 85 vol.% acetic acid and 15 vol.% perchloric acid, a current of 22-29 mA, a voltage of 20.5 V, a temperature of 279- 280 K, a flow rate setting “20” and a treatment time of 225-388 s, followed by rinsing in, consecutively, ethanol, acetone and isopropanol.

TEM investigations were performed using a Philips CM 200 microscope operating at 200 kV, equipped with an energy-dispersive X-ray detection system (EDX). The bright field (BF), dark field (DF) images, and the selected area diffraction patterns (SADPs) were recorded using a Gatan CCD camera attached to the microscope. Qualitative compositional analysis of the nitride precipitates which developed upon nitriding was carried out by energy-dispersive X-ray analysis (EDX) using a detector attached to the TEM.

4.3.3 Quantitative analysis of composition and nitrogen uptake

For the determination of elemental (Fe, Si and N) concentrations in the nitrided zone EPMA was performed on the polished cross-sections of nitrided specimens employing a Cameca SX100 microprobe. Measurements were performed using an accelerating voltage of 15 kV and a current of 100 nA. For obtaining the contents of Fe, Si and N at each measured point, the intensities of the characteristic Fe-K β , Si-K α and N-K α radiations were measured and divided by the corresponding intensities measured from standard specimens (pure iron, pure silicon and γ' iron nitride (for nitrogen)). The elemental concentrations were calculated from these intensity ratios applying the $\phi(\rho z)$ approach [56].

For obtaining accurately the small amounts of nitrogen in both the nitrided and denitrided specimens, samples were weighed using a Mettler's microbalance before and after the nitriding and denitriding treatments. From the weight gain/loss of the nitrided/denitrided samples, the amount of nitrogen taken up/lost was determined.

4.3.4 X-ray diffraction

X-ray diffractograms were recorded using a PANalytical X'pert Multipurpose Diffractometer which was equipped with a graphite monochromator in the diffracted beam, employing Co-K α

radiation and Bragg- Brentano geometry. During the measurements, the specimens were rotated around their surface normal to get better crystallite statistics.

4.3.5 Microhardness measurement

Microhardness measurements were carried out on the cross-sections of nitrided specimens by use of a Vickers microhardness tester (Leica VMHT Mot). A load of 50 g, an indentation speed of 50 $\mu\text{m/s}$ and a loading time of 10 s were applied. Each hardness value presented is the average of four hardness measurements; the standard deviation of the four measurements is used as an error estimate.

4.4 Morphology: light optical and scanning electron microscopy

Light optical micrographs recorded from the etched cross-sections of an unnitrided recrystallised Fe-2at.%Si alloy specimen and of the recrystallised Fe-2at.%Si alloy specimens nitrided for different times (30 h, 65 h, 165 h and 332 h) at 580°C using a r_N of 0.104 $\text{atm}^{-1/2}$ are shown in Fig. 4.1. Surprisingly, the micrographs recorded from the specimens nitrided for different times show no distinction of a surface adjacent nitrided layer and an unnitrided core region, in contrast with results obtained for nitrided Fe-Al [49], Fe-Cr [25], Fe-V [6] and Fe-Ti [58] alloys. Instead, the etching contrast was found to be uniform at all depths of the 1 mm thick specimens, but changing with nitriding time, indicative for progress of the nitriding reaction (similarly at all depths) with nitriding time (Figs. 4.1 b-e). This finding suggests the occurrence of ideally weak nitriding kinetics (implying a constant nitrogen concentration and hardness, as function of depth, for different nitriding times, see Fig. 1 in Ref. [21]), which is confirmed by the measured hardness-and nitrogen-concentration depth profiles (cf. section 4.6).

The observation of ideally weak nitriding behaviour for a specimen of such large thickness, 1 mm, is highly unusual: for example, nitriding of recrystallised Fe-Al alloy also shows weak nitriding interaction, but in order to realize *ideally* weak nitriding behaviour (i.e. the nitrogen concentration is constant at all depths), under comparable conditions, the specimen should be 0.1 mm thick or less, i.e. 10 times less thick [21] (further, see section 4.6).

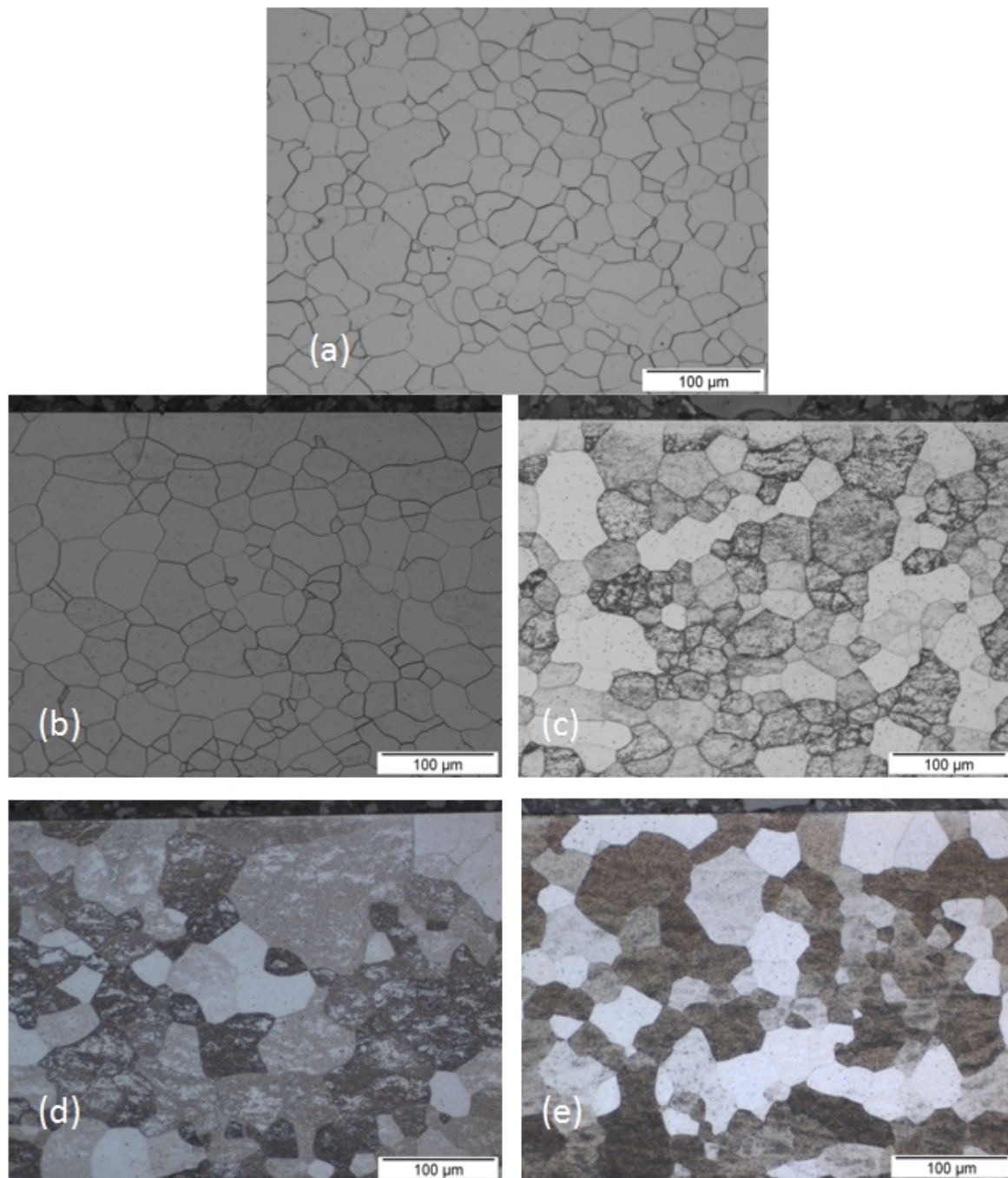


Fig. 4.1: Light optical micrographs recorded from cross-sections of Fe-2at.%Si alloy specimens (a) unnitrided (b) 30 h nitrided, (c) 65 h nitrided, (c) 165 h nitrided, and (d) 332 h nitrided ($T = 580^{\circ}\text{C}$; $r_{\text{N}} = 0.104 \text{ atm}^{-1/2}$). A uniform etching contrast is observed for the nitrided specimens: distinction of a nitrided zone and an unnitrided core region cannot be made. The etching contrast becomes more pronounced upon increasing nitriding time.

SEM performed at cross-sections of the specimens nitrided for different times show a thin layer of nitride phase precipitated along the ferrite-grain boundaries of the 30 h nitrided specimen (Fig. 4.2a). Upon prolonged nitriding fine, more or less cubical and rod/plate-like precipitates develop inside the ferrite grains (Figs. 4.2 b-c). Adjacent to the grain-boundary

nitride layer a thin precipitate free zone (PFZ) occurs (Fig. 4.2d). TEM investigation showed that the precipitates both inside the ferrite grains and along the ferrite grain boundaries are *amorphous* silicon nitride (cf. section 4.5).

The very slow nucleation and growth of (amorphous) silicon nitride can be understood in view of the extraordinarily large volume misfit between nitride particles and matrix: 106 % for Si_3N_4 ⁴, as compared to 52 % for CrN, 50 % for VN, 64 % for TiN (cf. section 1.3 of chapter 1). This also makes understandable that precipitation of silicon nitride occurs more rapidly, i.e. more easily, at grain boundaries as there the misfit can be accommodated more easily, apart from a higher driving force for nucleation due to the annihilation of grain-boundary area.

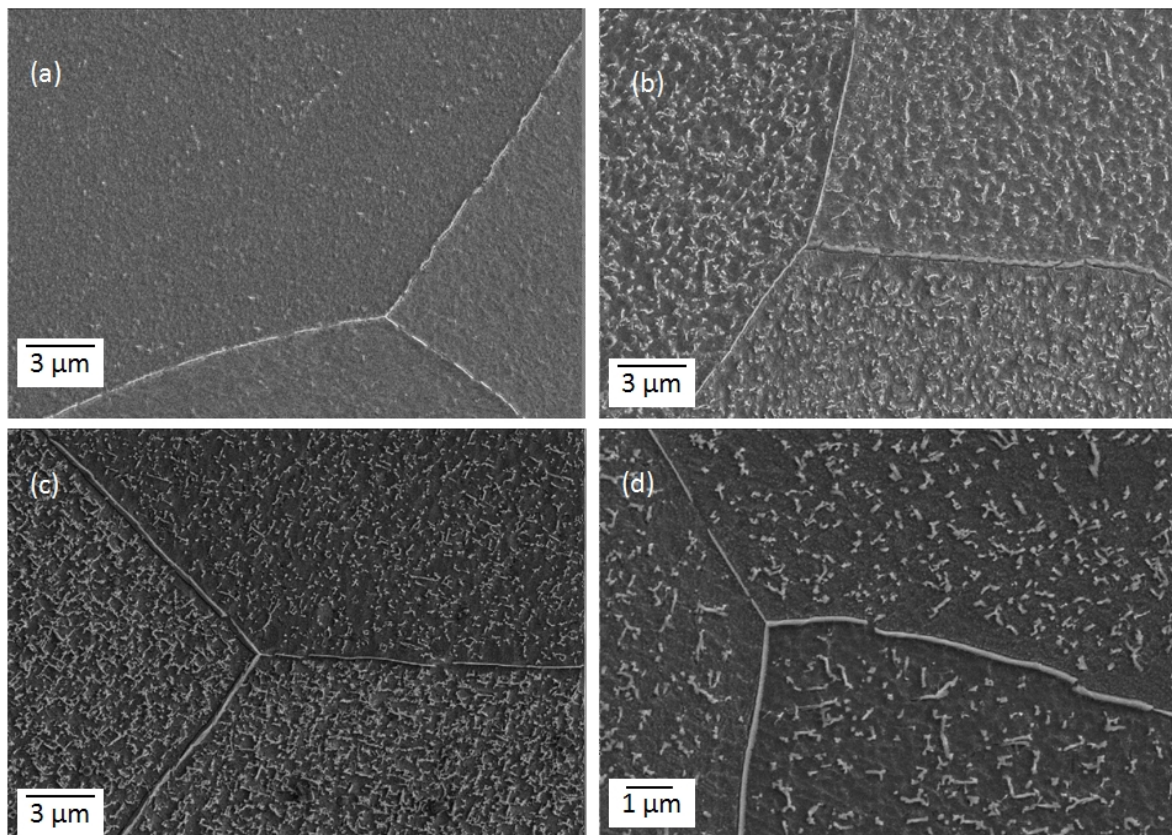


Fig. 4.2: SEM micrographs recorded from cross-sections of nitrided ($T = 580^\circ\text{C}$; $r_N = 0.104 \text{ atm}^{-1/2}$) Fe-2at.%Si alloy specimens. After 30 h (a) of nitriding bands of nitride phase have developed along the ferrite-grain boundaries. Upon increasing nitriding time to 165 h (b) and 332 h (c), fine precipitates have developed inside the ferrite grains. Precipitate free regions occur adjacent to the ferrite-grain boundaries (d) (332 h).

⁴ This calculation is based on the crystalline modification of Si_3N_4 . For the amorphous modification of Si_3N_4 the volume misfit will be even somewhat larger.

4.5 Amorphous nature of the silicon-nitride precipitates

In none of the SADPs recorded from TEM foils prepared from nitrated Fe-2at.%Si alloy specimens, diffraction spots additional to those belonging to ferrite can be detected. A diffuse intensity (“halo”) around the transmitted beam is observed (cf. inset of Fig. 4.3a), indicating the possible presence of an amorphous (silicon-nitride) phase, as reported for the first time in an earlier, unnoticed work [18]. A TEM dark field (DF) image formed with a part of the diffuse intensity around the transmitted beam (see the encircled region in the SADP shown as inset in Fig. 4.3a) reveals the (precipitate) regions, contributing to the diffuse intensity, which regions appear moreover contrastless (Fig. 4.3a). These observations demonstrate the amorphous nature of the nitride precipitates. The same type of TEM analysis was applied to the grain-boundary precipitates (not reported in the earlier work [18]), which showed that the grain-boundary precipitates are amorphous as well (Fig. 4.3b).

The amorphous nitride particles in the bulk appear to have a cubical or plate (rod) – like morphology (see Figs. 4.3a and 4.5a,c). In an early note [84] on nitrated iron-silicon alloy, particles of the same cubical morphology as found here and in Ref. [18] were observed, but they could not be identified.

Employing the electropolishing technique for TEM-foil preparation resulted in selective dissolution of the less inert ferrite matrix, leaving the rather inert silicon-nitride precipitates. As a result the nitride precipitates got separated from the ferrite matrix and some precipitates appeared “self supported” near the (jet-polished) holes in the TEM foil (Fig. 4.3c). The electron-diffraction pattern of these particles (inset of Fig. 4.3c) only shows the diffuse intensity rings as already discussed above. Application of local X-ray elemental point analysis (EDX) showed that the precipitates contain both silicon and nitrogen. The amount of nitrogen taken up by a through nitrated specimen (cf. section 4.7) indicates that silicon precipitates as the stoichiometric silicon nitride, Si_3N_4 .

X-ray diffractograms recorded from the surface of the nitrated specimens showed only broadened diffraction peaks of the ferrite matrix (Fig. 4.4): compatible with the amorphous nature of the silicon-nitride precipitates (see above), no reflections corresponding to silicon nitride occur. The broadening of the diffraction peaks of the ferrite matrix is ascribed to the microstrain (see Ref. [67]), induced by the large volume misfit (106 %) between silicon-nitride precipitates and the surrounding ferrite matrix.

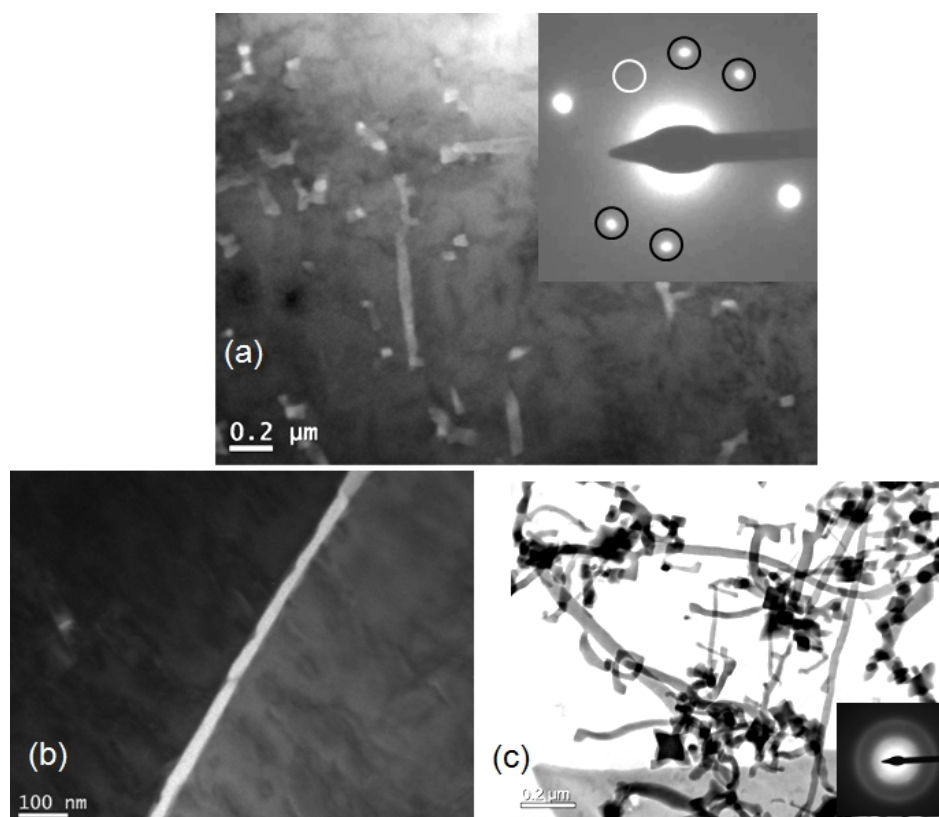


Fig. 4.3: (a) TEM-DF image and the corresponding SADP (electron-beam/zone axis not far from $[113]_{\alpha\text{-Fe}}$) recorded from the ion-thinned TEM foil from a 332 h nitrated Fe-2at.%Si specimen; DF image was formed with the diffuse intensity from the halo around the transmitted beam (as contained by the white circle indicated in the SADP shown in (a)); the diffraction spots encompassed by black circles pertain to 113-type reflections of iron oxide, Fe_3O_4 , which develops on the surface of the TEM foil). The bright, contrastless regions are amorphous silicon nitride (see text). (b) TEM-DF image (formed in a similar way as the DF image (a)) recorded from the ion-thinned TEM foil prepared from a 332 h nitrated Fe-2at.%Si specimen. The bright, contrastless appearance of the grain-boundary phase is compatible with its amorphous nature. (c) TEM BF image and the corresponding SADP recorded from the TEM foil prepared by electro-jet polishing from a 130 h nitrated Fe-2at.%Si specimen. SADP from such isolated particles (c) shows only diffuse intensity rings compatible with an amorphous nature of the nitride particles. The isolated amorphous silicon-nitride nanoprecipitates have a thickness up to 50 nm and length up to 1000 nm. The precipitates got isolated from the matrix due to selective dissolution of the ferrite matrix.

The very slow nucleation and growth of silicon nitride in the ferrite matrix (cf. results presented in section 4.6) leaves more than enough time for Si and N atoms to come together by solid state diffusion in the ferrite matrix and to arrange themselves in the *crystalline* modification of Si_3N_4 . The emergence of an amorphous modification then should have a thermodynamic rather than a kinetic origin. For smaller sized precipitates (having a relatively large interface/volume ratio), a relatively low energy of the interface between amorphous silicon

nitride and the crystalline ferrite matrix, as compared to the energy of the interface between crystalline silicon nitride and the crystalline ferrite matrix, can stabilize thermodynamically an amorphous nature of the silicon-nitride precipitates, as first suggested in Ref. [18] adopting a theoretical framework reviewed in Ref. [19]. Remarkably, the faces of the cubical particles are parallel to $\{100\}_{\alpha\text{-Fe}}$ (cf. Figs. 4.5a,c and Fig. 2 in Ref. [18]) suggesting that the amorphous Si_3N_4 /crystalline $\alpha\text{-Fe}$ interface preferably forms along $\{001\}_{\alpha\text{-Fe}}$.

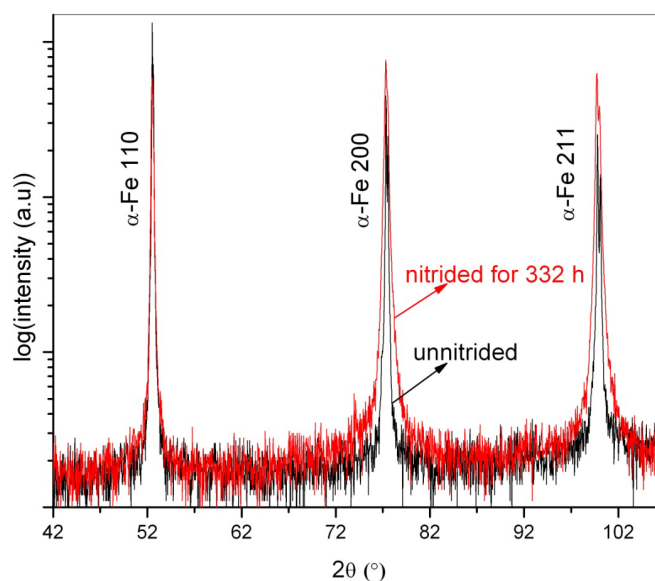


Fig. 4.4: Superposition of X-ray diffractograms (Co-K α radiation) recorded from the surface of an unnitrided Fe-2at.%Si specimen and a 332 h nitrided ($T = 580^\circ\text{C}$; $r_N = 0.104 \text{ atm}^{-1/2}$) Fe-2at.%Si alloy specimen. Only reflections of the ferrite matrix can be detected. The ferrite reflections become broadened upon nitriding due to the microstrain in the ferrite matrix surrounding the misfitting silicon-nitride precipitates.

Efforts in the present work to crystallize the amorphous precipitates by annealing the specimens at 700°C in a nitriding atmosphere (NH_3/H_2 mixture at a r_N of $0.02 \text{ atm}^{-1/2}$) for 40 h were not successful. This is compatible with the very high temperatures ($>1200^\circ\text{C}$) needed to crystallize bulk specimens of amorphous silicon nitride [85]. It is noted here that similar to internal precipitation of silicon nitride, precipitation of spherical amorphous silica (SiO_2) has been observed during internal oxidation of Cu-Si [86] and Ni-Si [87] alloys, which here is suggested to have the same thermodynamic origin as the precipitation of amorphous Si_3N_4 particles upon nitriding Fe-Si alloys (no explanation was given in Refs. [86] and [87] for the development of amorphous SiO_2 particles in a crystalline matrix).

TEM investigation on a ferrite grain in the TEM foil with an electron-beam/zone axis close to $[001]_{\alpha\text{-Fe}}$ showed, in addition to the amorphous silicon-nitride precipitates, the presence of crystalline $\alpha''\text{-Fe}_{16}\text{N}_2$ precipitates along $\{100\}$ planes of the ferrite matrix, having a platelet-

type morphology (see bright field, dark field and SADP shown in Fig. 4.5). Due to the orientation relationship between α'' -nitride and ferrite [88-89], $(010)_\alpha // (001)_{\alpha''}$ and $[001]_\alpha // [010]_{\alpha''}$, and its variants, the strongest reflections of α'' overlap with/are close to ferrite reflections (Fig. 4.5d). This, together with the very low intensity of α'' nitride diffraction spots (in particular the “superstructure” reflections), only a few α'' diffraction spots can well be detected as separate reflections: e.g. 103-type spots and 004-type spots close to 002 type spots of the ferrite matrix (see SADP shown in Fig. 4.5b and compare with the calculated diffraction pattern in Fig. 4.5d).

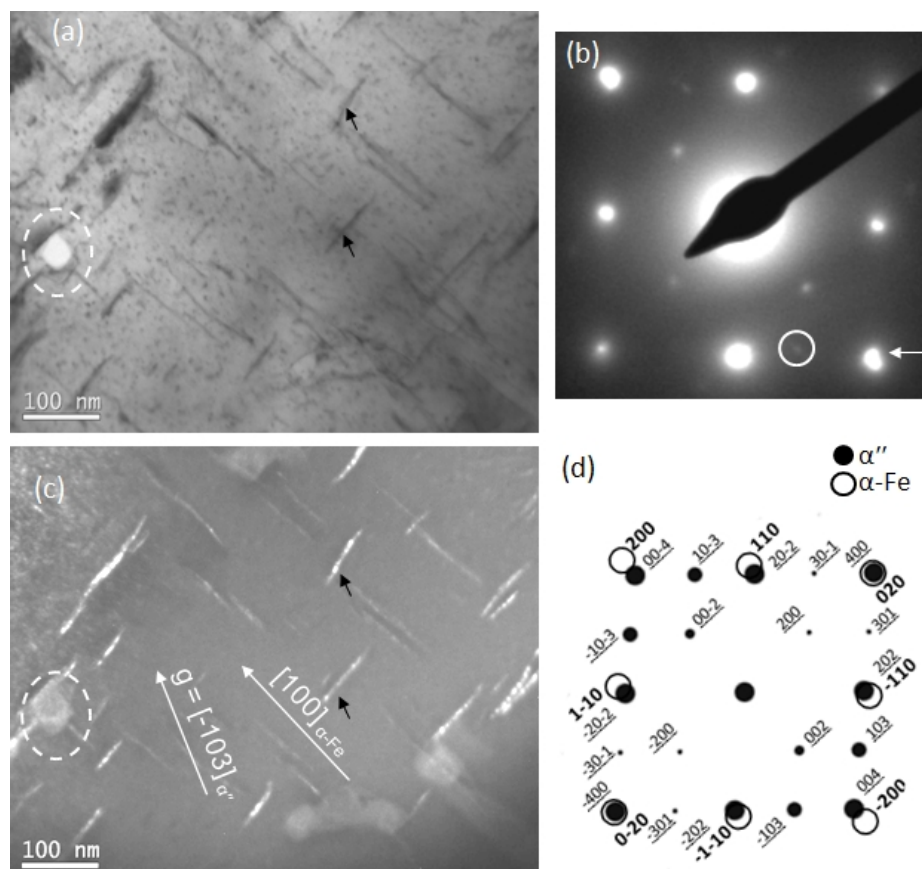


Fig. 4.5: TEM-BF image (a) and the corresponding SADP ((b) electron-beam/zone axis near to $[001]_{\alpha\text{-Fe}}$) recorded from the Fe-2at.%Si alloy specimen nitrated for 332 h and the DF image (c) formed with the -103 diffraction spot (shown with white circle in the SADP shown in (b)) of $\alpha''\text{-Fe}_{16}\text{N}_2$; the direction perpendicular to the (100) lattice planes of $\alpha\text{-Fe}$ and the diffraction vector, \mathbf{g} , have been indicated in (c). In addition to cubical shaped amorphous silicon nitride precipitates (indicated with white dashed ovals in (a) and (c)), crystalline $\alpha''\text{-Fe}_{16}\text{N}_2$ platelets (indicated with small black arrows in (a) and (c)) can be observed. The calculated diffraction pattern for the orientation relationship between ferrite and α'' -nitride, $(010)_\alpha // (001)_{\alpha''}$ and $[001]_\alpha // [010]_{\alpha''}$, is shown in (d); in (d) miller indices for α'' spots are underlined. The location of the 103-type diffraction spots of α'' , relative to that of matrix diffraction spots, and the appearance of the split 200-type diffraction spot of the $\alpha\text{-Fe}$ matrix (shown with white arrow in (b)) are compatible with the orientation relationship between α'' and ferrite (cf. Figs. b and d).

The occurrence of these α'' -nitride precipitates is likely due to precipitation from the nitrogen supersaturated ferrite matrix during the cooling (water quenching) and/or upon subsequent room temperature aging [53-54] of the nitrided specimen. This could in particular occur for the 332 h nitrided specimen shown in Fig. 4.5, as the nitrogen solubility of the matrix of long-time nitrided specimens is relatively large; (cf. section 4.6).

4.6 Ideally weak nitriding kinetics; hardness and nitrogen-concentration depth profiles

Vickers hardness-depth profiles, measured on cross-sections of the Fe-2at.%Si alloy specimens nitrided for different times at 580°C applying a r_N of $0.104 \text{ atm}^{-1/2}$, are shown in Fig. 4.6. At all times, the hardness increase due to nitriding is the same at all depths of the nitrided specimens.

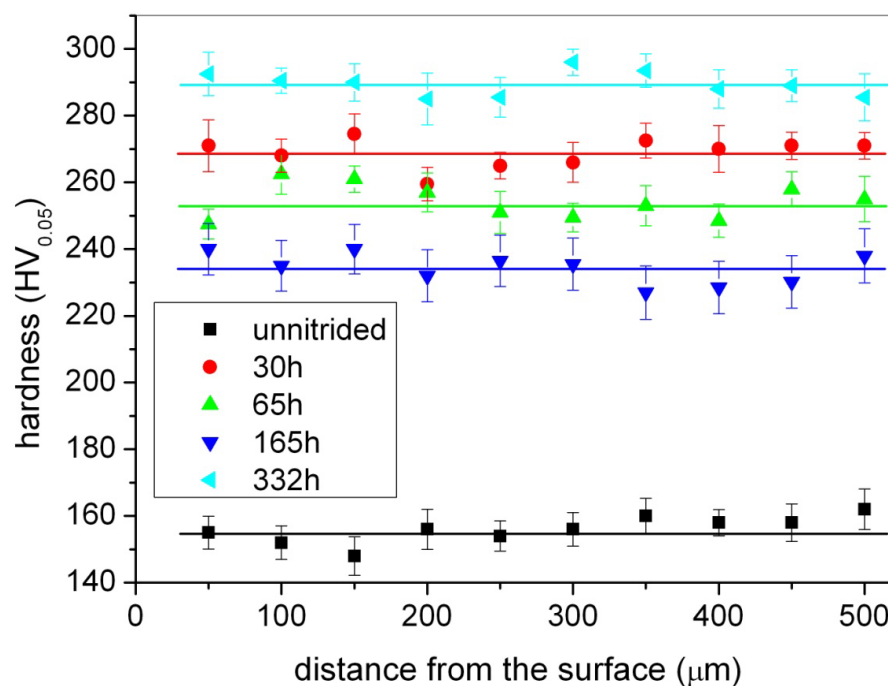


Fig. 4.6: Hardness (load=50 g, time=10 s)-depth profiles measured on cross-sections of unnitrided and for different times (as indicated in the figure) nitrided ($T = 580^\circ\text{C}$; $r_N = 0.104 \text{ atm}^{-1/2}$) Fe-2at.%Si alloy specimens.

The measured (EPMA) elemental concentration-depth profiles show that the nitrogen content is the same at all depths of the nitrided specimens (Fig. 4.7), which is compatible with the hardness-depth profiles. The scatter in the measured N and Si contents is ascribed to the distribution and size of the silicon-nitride precipitates in the bulk of the grains and at the grain boundaries: indeed the variation of the N content correlates with the variation of the Si content

(Fig. 4.7c). The higher sensitivity of the EPMA measurements for Si than for the light element N led to a larger scatter in the measured N-content values than in the measured Si-content values.

The observed uniform, depth independent nature of the hardness, nitrogen content and etching contrast (cf. section 4.4) of the nitrided specimens is a clear manifestation of ideally weak nitriding kinetics (see Fig. 3b in Ref. [21]). Such ideally weak nitriding kinetics implies that the silicon-nitride precipitation reaction initiates at the same time at all depths and proceeds at the same rate at all depths, i.e. the amount of silicon nitride formed by precipitation is the same at all depths of the nitrided specimens.

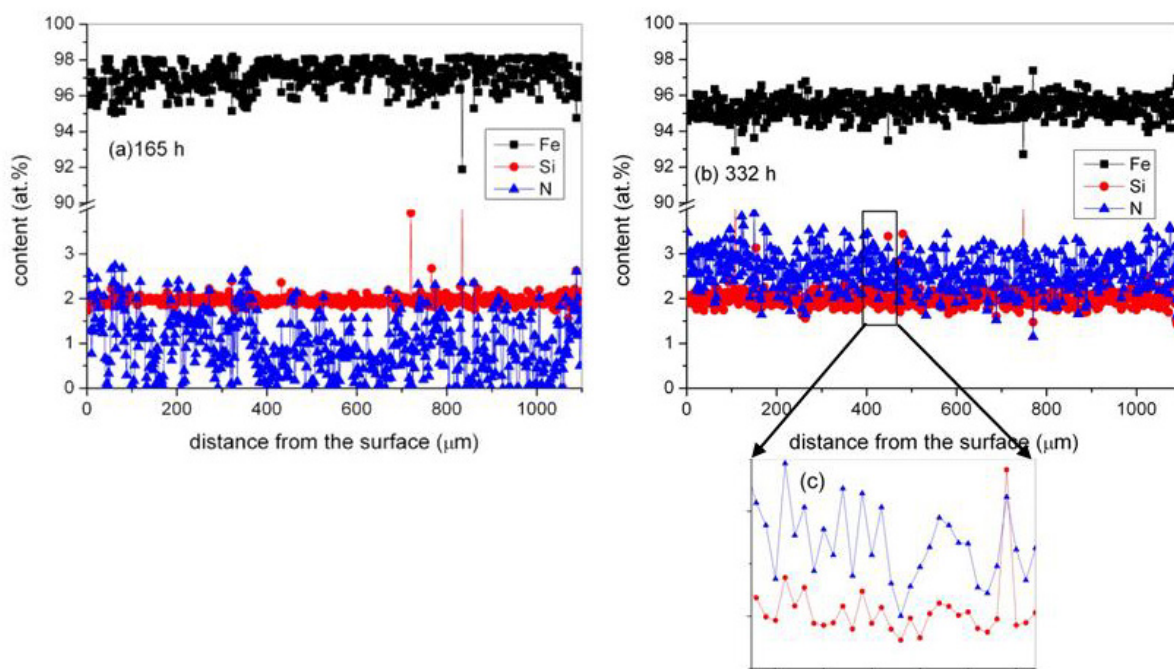


Fig. 4.7: Elemental (Fe, Si and N) concentration-depth profiles determined by EPMA for 165 h nitrided (a) and 332 h nitrided (b) Fe-2at.%Si alloy specimens ($T = 580^{\circ}\text{C}$; $r_{\text{N}} = 0.104 \text{ atm}^{-1/2}$). Scatter in the N content is ascribed to the distribution and size of the silicon-nitride precipitates because a peak in the N content is spatially correlated with a peak in the Si content (c).

The occurrence of ideally weak nitriding kinetics implies that the apparent incubation time for alloying element nitride (MeN_n) nucleation is (much) larger than the time required to homogeneously saturate the entire specimen with nitrogen: then the alloying element nitride precipitation initiates at the same time at all depths of the nitrided specimen. After that, in accordance with the occurrence of ideally weak nitriding kinetics throughout the precipitation reaction, inwardly diffusing nitrogen prefers to (again) saturate the ferrite matrix throughout the

specimen with dissolved nitrogen, rather than to react near the surface with silicon to form new or let grow already existing silicon-nitride precipitates.

The nitrogen concentration-depth profiles which develop upon nitriding of pure iron can be straightforwardly calculated numerically, recognizing the competition between the finite rates of surface reactions such as ammonia dissociation, nitrogen diffusion into the solid substrate and the association of surface adsorbed nitrogen atoms and their subsequent desorption as N₂ molecules. Due to the finite rates of these competing surface reactions the nitrogen-surface concentration increases with nitriding time up to establishment of a stationary state or the local (= at the surface) thermodynamic equilibrium [2, 12-13]. To achieve local thermodynamic equilibrium (instead of a stationary state), the desorption rate of nitrogen gas from the surface by the association of the surface adsorbed nitrogen atoms, must be neglectable [2, 12-13]⁵. For details about the numerical calculation method followed in this work, see the appendix in Ref. [2]. Calculations were performed for the specimen thickness and the nitriding conditions employed in the present work (1 mm thick Fe-2at.%Si alloy specimens nitrided at 580°C using a r_N of 0.104 atm^{-1/2}) and in earlier work (0.3 mm thick Fe-1.75at.%Si alloy specimens nitrided at 575°C using a r_N of 0.075 atm^{-1/2}, see Ref. [20]). For the calculations the following data were used: the equilibrium nitrogen solubility of ferrite at 580°C for a r_N of 0.104 atm^{-1/2} is 0.27 at.%, and at 575°C for a r_N of 0.075 atm^{-1/2} is 0.19 at.% (using data from Ref. [12]); the diffusion coefficients of nitrogen in pure ferrite at 580°C and at 575°C are 1.122*10⁻⁷ cm²/s and 1.052*10⁻⁷ cm²/s, respectively (using data from Ref. [90]); the ammonia-dissociation reaction-rate coefficient on the iron surface at 580°C for a r_N of 0.104 atm^{-1/2} is 9.58*10⁻⁶ cm/s and at 575°C for a r_N of 0.075 atm^{-1/2} is 9.31*10⁻⁶ cm/s (using data from Refs. [91-92]). The results of such calculations for nitrided ferrite specimens, for the thicknesses, nitriding potentials and temperatures indicated above, are presented in Fig. 4.8 (note the different scales used for the abscissas in this figure).

The calculated nitrogen concentration-depth profiles for the thin (0.3 mm) pure iron specimen (Fig. 4.8a) reveal a relatively small gradient of the nitrogen concentration and the equilibrium nitrogen solubility of pure ferrite is reached throughout the specimen thickness after nitriding for 5 h. On the other hand, the calculated nitrogen concentration-depth profiles for the thick (1 mm) pure iron specimen (Fig. 4.8b) show the occurrence of relatively large gradients of

⁵ Consideration of N₂ desorption increases the calculated time needed for nitrogen saturation of the specimens by about 10%. This increase of the nitrogen saturation time does not affect the conclusions drawn in this work.

the nitrogen concentration and the equilibrium nitrogen solubility is reached throughout the specimen thickness only after a long nitriding time of 20 h (cf. Figs. 4.8a and b).

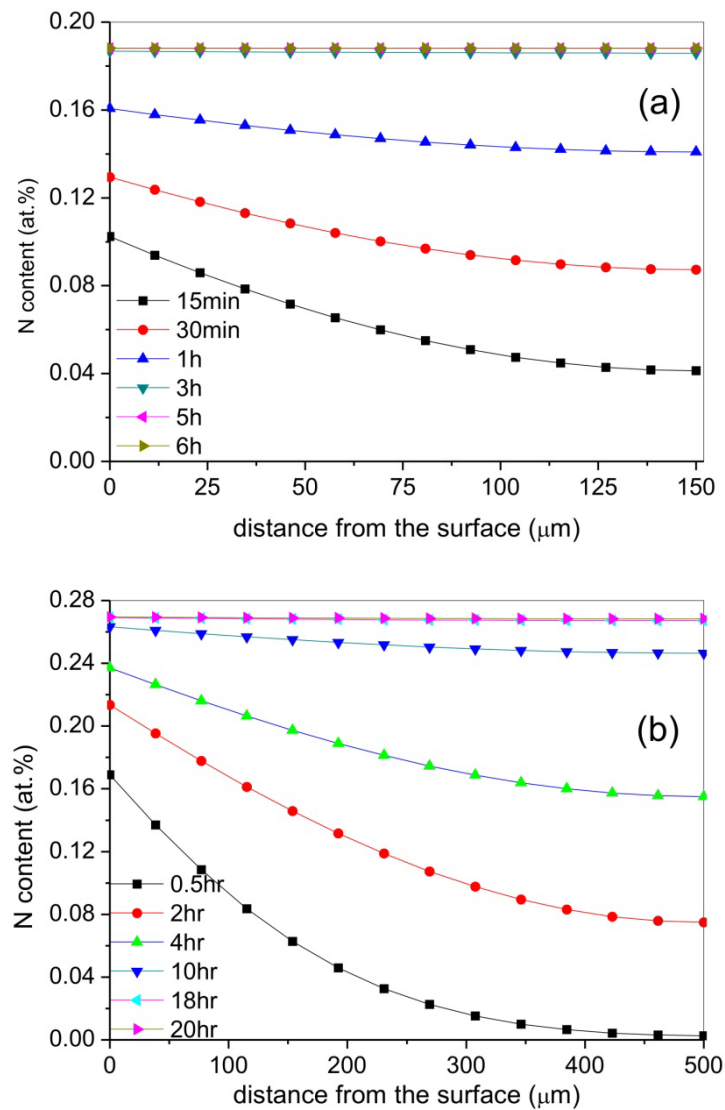


Fig. 4.8: Calculated (see text) nitrogen concentration-depth profiles developing upon nitriding pure iron specimens of different thickness (note the different scales of the abscissas). (a) 0.3 mm thick specimen: nitrided at 575°C employing a r_N of 0.075 atm^{-1/2}. (b) 1 mm thick specimen: nitrided at 580°C employing a r_N of 0.104 atm^{-1/2}.

For a thin (0.3 mm) recrystallised Fe-1.75at.%Si alloy specimens nitrided at 575°C an incubation time of 10 h was observed for silicon-nitride precipitation [20], which is significantly larger than the time needed for nitrogen saturation of the specimen (which is about 5 h; see Fig. 4.8a). Hence, the occurrence of ideally weak nitriding kinetics is expected and was observed indeed.

In view of the incubation time of 10 h for initiating silicon-nitride precipitation in a Fe-1.75at.%Si alloy specimen nitrided at 575°C, and the need of a nitriding time of at least 20 h for nitrogen saturation of a specimen of thickness 1 mm at 580°C (see above), the occurrence of ideally weak nitriding interaction for the *thick* (1 mm) Fe-2at.%Si alloy specimens nitrided at 580°C at first sight is surprising. This finding can then be discussed as follows.

The incubation time for silicon-nitride precipitation in the thick (1 mm) Fe-2at.%Si specimen nitrided at 580°C is about 30 h (see section 4.8), which is three times larger than reported [20] for the thin (0.3 mm) Fe-1.75at.%Si specimens at an even somewhat lower temperature (575°C vs. 580°C) and at an even somewhat smaller silicon content (1.75 at.% vs. 2.03 at.%). In view of the calculated nitrogen concentration-depth profiles (Figs. 4.8a and b) it may now be concluded that the apparent incubation time for silicon-nitride precipitation is always larger than the time necessary for nitrogen saturation of the matrix throughout the thickness of the specimen. In other words: silicon nitride can only start to precipitate after the equilibrium nitrogen solubility of the ferrite matrix has been realized *throughout the specimen*. An extreme consequence of this reasoning is, that weak nitriding kinetics is expected for Fe-2at.%Si alloy at 580°C for specimens of *any* thickness. Or, alternatively, for an infinitely thick specimen the incubation time would be infinitely large: the nitrogen entering the specimen from the gas phase prefers to maintain its dissolved state in the ferrite matrix and only after a certain degree of nitrogen supersaturation of the ferrite matrix has been attained at all depths (i.e. has been forced to occur by employing a specimen of finite thickness), silicon-nitride precipitation sets in.

4.7 Nitrogen solubility of ferrite matrix and composition of the amorphous nitride precipitates

The amounts of strongly bonded nitrogen (to silicon in the form of silicon-nitride precipitates) and of weakly or less strongly bonded nitrogen (interstitially dissolved nitrogen and nitrogen possibly adsorbed at the silicon-nitride/ferrite-matrix interface [24]), in specimens nitrided for different times, were obtained by hydrogen reduction/denitriding at 450°C. Whereas silicon nitride is stable against hydrogen reduction at 450°C, the weakly bonded, interstitially dissolved and possibly interface adsorbed nitrogen atoms are removed from the specimen upon denitriding. From the measured mass changes (cf. section 4.3.3), the amounts of nitrogen present in the nitrided and denitrided specimens were determined and the thus obtained results are presented in

Table 4.2 (note that the distribution of nitrogen is uniform in the nitrified specimens; see Figs. 4.1, 4.6 and, in particular 4.7).

Table 4.2: Nitrogen content in the nitrified ($T = 580^{\circ}\text{C}$; $r_N = 0.104 \text{ atm}^{-1/2}$) and denitrified (450°C , 72 h in H_2) Fe-2at.%Si alloy specimens as determined by mass measurements. The error in the measured nitrogen contents is less than 0.01 at.%.

nitrifying time (h)	N content after nitrifying (at.%)	N content after denitrifying $\sim [\text{N}]_{\text{Si}_3\text{N}_4}$ (at.%)	N content removed during denitrifying ($[\text{N}]_{\alpha} + [\text{N}]_{\text{ads}}$) (at.%)
30	0.2	0.05	0.15
165	1.34	1.17	0.17
332	2.78	2.53	0.25
609	2.86	2.59	0.27
825	2.93	2.65	0.28

The amount of nitrogen remaining in the specimen after denitrifying increases with increasing nitrifying time (see third column in Table 4.2). The amount of nitrogen removed from the specimen during denitrifying also increases with increasing nitrifying time (see column 4 in Table 4.2)⁶. Both observations suggest that with increasing nitrifying time dissolved Si gradually precipitates as silicon nitride. As a consequence the nitrogen solubility of the ferrite matrix increases (see 4th column in Table 4.2 and see the above indicated footnote). After completed precipitation of Si as silicon nitride (after 825 h of nitrifying the saturation, plateau level of nitrogen uptake is reached; see Fig. 4.9), the amount of nitrogen removed during the denitrifying treatment is slightly larger than the equilibrium N solubility of pure ferrite. Nitrogen in excess of the equilibrium solubility is called “excess nitrogen” (for more information on excess N, see [24]).

The nitrogen content remaining in the 825 h nitrified specimen after denitrifying (2.65 at.%) is nearly equal to the nitrogen content expected if all Si present in the Fe-2.03at.%Si alloy would precipitate as silicon nitride, of composition Si_3N_4 (2.64 at.%). Hence, the amorphous silicon-nitride precipitates have the composition Si_3N_4 .

⁶ The amount of nitrogen removed during the denitrifying treatment of the 30 h nitrified specimen (0.15at.%) is smaller than the equilibrium N solubility of unstrained pure ferrite (0.27at.% at 580°C and at a r_N of $0.104 \text{ atm}^{-1/2}$ [12]), which is attributed to a nitrogen solubility of ferrite lower in the presence of dissolved Si [93-94].

4.8 Initial stage of nitride precipitation and “self-catalysis”: non-monotonous hardness change and increasing nitrogen-uptake rate with nitriding time

An unusual, non-monotonous change of hardness of the nitrified specimens with increasing nitriding time was observed (Fig. 4.9; cf. Fig. 4.6): After 30 h of nitriding, a significant increase in the hardness of the specimen had occurred. Prolonged nitriding up to 165 h led to a decrease of hardness. After a nitriding time of 332 h the hardness had increased (again) to a value somewhat larger than the hardness value obtained after 30 h. In contrast to the non-monotonous change of the hardness as function of nitriding time, the nitrogen content of the specimen increases continuously with increase in nitriding time (Fig. 4.9).

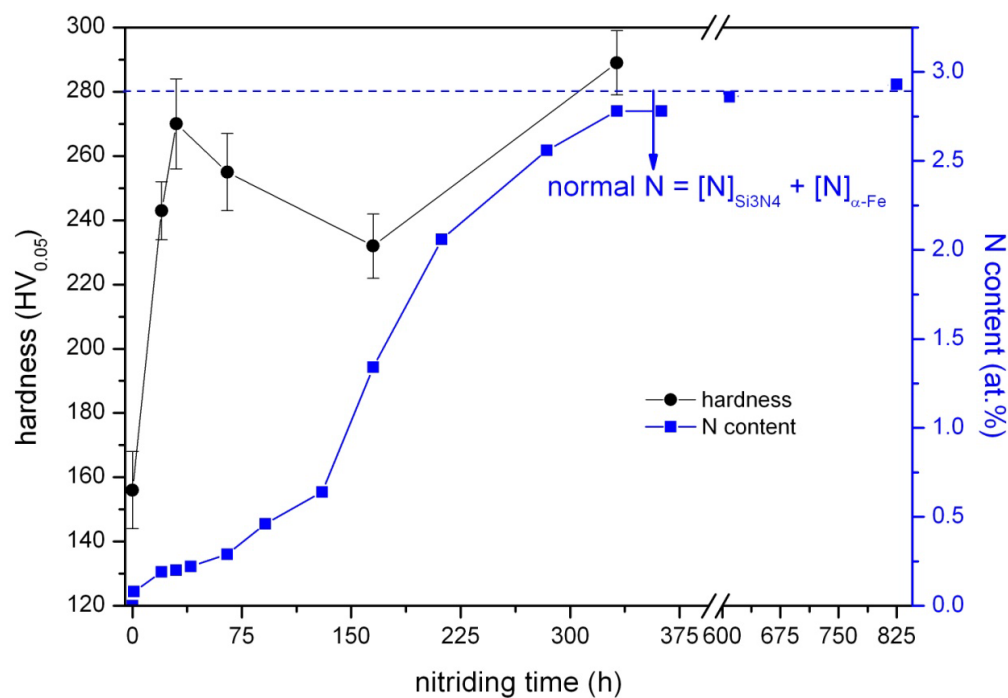


Fig. 4.9: Hardness and nitrogen content for the recrystallised Fe-2at.%Si alloy specimens nitrified for different times at 580°C applying a r_N of 0.104 atm^{-1/2}. Blue dotted line indicates the level of “normal nitrogen” uptake which is the sum of (i) the nitrogen associated with the stoichiometric Si₃N₄ (when all Si present in the Fe-2at.%Si alloy precipitates as Si₃N₄) and (ii) the equilibrium nitrogen solubility of the remaining ferrite matrix (0.27 at.% at 580°C and $r_N=0.104$ atm^{-1/2}).

It should be recognized that part of the nitrogen in the specimen not bonded to silicon, i.e. dissolved in the ferrite matrix after quenching, can precipitate as α'' -Fe₁₆N₂ nitride during (cooling and in particular during) storage at room temperature and during the subsequent heat treatment associated with the embedding of the cross-sectional specimens (see section 4.3.1).

However the hardness increase observed upon nitriding for 30 h (~120 HV) is much larger than possible by the precipitation of α'' -Fe₁₆N₂: as follows from the data published in Ref. [95] (see Fig. 3, in [95]), the hardness increase by α'' -Fe₁₆N₂ precipitation for the same amount of nitrogen as present in the 30 h nitrided specimen (0.2 at.%), after a similar specimen-preparation method, is only about 60 HV. Hence, about (120-60 =) 60 HV of the hardness increase observed for the 30 h nitrided specimen cannot be ascribed to α'' -Fe₁₆N₂ precipitation but, instead, has to be attributed to the precipitation of (some) silicon nitride.

Hydrogen reduction of the 30 h nitrided specimen, by annealing at 450°C for 70 h in a flowing (500 ml/min) hydrogen gas atmosphere, removed most (0.15 at.%) of the nitrogen taken up during nitriding (0.20 at.%), i.e. only a small amount of nitrogen (0.05 at.%) remained in the specimen, which is assumed to be bonded with silicon (at 450°C silicon-nitride is stable in a hydrogen atmosphere, whereas the metastable α'' -Fe₁₆N₂ precipitates (see above discussion) dissociate and the corresponding nitrogen is removed from the specimen). It is this small amount of nitrogen bonded to silicon that is responsible for the above discussed contribution to the hardness increase (of about 60 HV) observed after 30 h of nitriding.

The higher hardness obtained for the specimen nitrided for 30 h, as compared to the specimens nitrided for 65 h and 165 h, may be discussed as follows. The initial bonding of silicon and nitrogen leads to very fine precipitates of amorphous silicon nitride. At this stage, due to the ultrasmall size of the precipitates, the volume misfit between precipitates and matrix can be (largely) accommodated elastically. The associated long-range strain fields surrounding the precipitates are responsible for the peak hardness after 30 h of nitriding. Upon continued nitriding growth of the precipitates occurs and elastic accommodation of the large volume misfit is no longer possible: a partially plastic accommodation of the misfit occurs leading to dislocation production associated with a reduction of the long-range nature of the misfit-strain fields leading to a decrease of hardness.

Evidently, after having reached a first saturation level of nitrogen, after about 30 h of nitriding, the nitrogen-uptake rate strongly increased upon continued nitriding (Fig. 4.9). The increase in nitrogen-uptake rate reflects the now progressively on-going silicon-nitride precipitation. This increase of the nitrogen-uptake rate with increasing nitriding time can be considered as the result of “self-catalysis”: the defects produced in the matrix by the first developed nitride precipitates, as dislocations (see above discussion), provide sites for *easier* nucleation of new precipitates (e.g. see Ref. [74]) and thus the nitrogen-uptake rate can increase

with nitriding time (a similar observation was made for the difficult precipitation of AlN in recrystallised Fe-2at.%Al alloy [38]).

4.9 Technological application of silicon-nitride precipitation in ferrite

As compared to the hardness increase induced by the precipitation of MeN_n nitrides in iron-based Fe-Me alloys with $\text{Me} = \text{Cr}, \text{Al}, \text{Ti}, \text{V}$, the hardness increase due to the precipitation of the amorphous Si_3N_4 is modest. Therefore application of Si as alloying element in nitriding steels to enhance pronouncedly the mechanical properties appears less likely. However, the initial development of (amorphous) nitride precipitates as bands along the grain boundaries of the ferrite matrix (cf. the results presented in section 4.4) suggests its application as a very efficacious “inhibitor” for grain growth.

Si is an important alloying element in electrical steel, usually applied as (laminated) sheets of, say, 0.3 mm thickness. The magnetically beneficial $\{110\} \langle 001 \rangle$, “Goss” [96] texture in electrical steel is the result of the preferential abnormal growth of “Goss” grains during the so-called secondary recrystallization [74]⁷. For the secondary recrystallization, also called abnormal grain growth, to dominate over the normal grain growth, it is necessary to attain small grain size or a sharp texture during primary recrystallization [74]. Small grain size after the primary recrystallization can be obtained by obstructing the normal grain growth during primary recrystallization by the inhibiting effect of second-phase particles at the grain boundaries, such as AlN and MnS (called “inhibitors” [97]). Controlled formation of inhibitors during dedicated thermo-mechanical treatment followed after slab casting is crucial to achieve the desired “Goss” texture. Inhibitors which form during or after hot rolling of the slabs are called “inherent” inhibitors, whereas the inhibitors which form during the nitriding treatment after cold rolling are called “acquired” inhibitors. By employing controlled low temperature nitriding (as in the present work), before the primary recrystallization, it is possible to realize amorphous silicon-nitride precipitation (in sheets of electrical steel) predominantly as bands along the grain boundaries (i.e. at this stage most of the silicon remains in dissolved state in the bulk of the grains so that its beneficial effect in increasing the resistivity of steel can be retained), which bands may act as inhibitor for normal grain growth in electrical steel.

⁷ Although several theories have been proposed for the mechanisms which can lead to the preferential, abnormal growth of “Goss” grains in electrical steel, none of them can explain completely the underlying mechanisms [97-99].

4.10 Conclusions

1. Upon nitriding crystalline, ferritic Fe-2at.%Si alloy amorphous precipitates of silicon nitride develop very slowly, initially along the ferrite-grain boundaries and later inside the ferrite grains. Although the chemical driving force for precipitation of silicon nitride is large, this precipitation occurs only with difficulty due to the extraordinarily large volume misfit (106 %) between nitride precipitate and ferrite matrix. The amorphous precipitates have the composition Si_3N_4 . The occurrence of the amorphous nature of the precipitates has a thermodynamic and not a kinetic origin: the amorphous silicon-nitride/ferrite-matrix interface has a lower interfacial energy than the crystalline silicon-nitride/ferrite-matrix interface.
2. Ideally weak nitriding kinetics hold for the internal nitriding of the recrystallised Fe-2at.%Si alloy specimens: hardness, nitrogen content and etching contrast observed in light microscopy are the same at all depths of the nitrided specimens. The apparent incubation time for nitride precipitation increases with increasing thickness of the specimen: only after a certain degree of nitrogen supersaturation has been established at all depths, silicon-nitride precipitation sets in.
3. An unusual non-monotonous hardness change occurs with increasing nitriding time: the hardness of the specimen nitrided at 580°C first increases until a nitriding time of about 30 h, then decreases until a nitriding time of about 165 h and thereafter increases again. The nitrogen content of the specimen reaches a first plateau value after about 30 h of nitriding and strongly increases upon continued nitriding. The simultaneous occurrence of the first hardness maximum and the first plateau of the nitrogen content are ascribed to the initial formation of ultra small silicon-nitride precipitates for which the large misfit with the matrix is accommodated (largely) elastically.
4. The strong increase of the nitrogen-uptake rate upon continued nitriding is caused by the relatively easy nucleation of silicon-nitride precipitates on defects (dislocations) generated in the matrix by the first developed precipitates upon their growth as a consequence of the now (partially) plastically accommodated misfit between precipitates and matrix.
5. The occurrence of ideally weak nitriding kinetics and the initially preferential precipitation of amorphous silicon nitride as bands along the ferrite-grain boundaries suggest its

technological application as inhibitor of “normal grain growth” in the production of crystallographically grain-oriented electrical steel.

Nitride formation and excess nitrogen uptake upon nitriding ferritic Fe-Ti-Cr alloys

K.S. Jung, S. Meka, R.E. Schacherl, E. Bischoff and E.J. Mittemeijer

Abstract

The microstructure of the nitrated zone of Fe-Ti-Cr alloys, containing a total of 0.30 at.% (Ti + Cr) alloying elements, with varying Ti/Cr atomic ratio (0.45, 0.87 and 1.90), was investigated by X-ray diffraction (XRD) and transmission electron microscopy (TEM). The stable TiN and CrN nitrides did not precipitate upon nitriding. Instead, ultrafine, metastable, mixed $Ti_{1-x}Cr_xN$ nitride precipitates developed in the nitrated zone: the precipitates were of platelet morphology (length ≤ 30 nm and thickness ≤ 3 nm) and of cubic, rock-salt crystal-structure type. The misfit strain around the nitride platelets in the ferrite matrix increases with increasing Ti/Cr atomic ratio. As a consequence, most pronouncedly for the highest Ti/Cr atomic ratio, a tetragonally distorted ferrite matrix surrounds the precipitates, as evidenced both by XRD and TEM. The amount of nitrogen taken up was determined quantitatively by measuring so-called nitrogen-absorption isotherms. It follows that the absorbed amount of so-called excess nitrogen dissolved in the matrix and adsorbed at the nitride-platelet faces increases distinctly with increasing Ti/Cr atomic ratio. The results were discussed in terms of the dependence of misfit strain on the Ti/Cr atomic ratio and the higher chemical affinity of Ti for N than of Cr for N.

5.1 Introduction

Nitriding is a widely-used thermochemical surface treatment for, in particular, ferritic steels [100]. The formation of inner nitrides can cause a large improvement of the mechanical properties. Due to the possibility of precise control of the nitriding atmosphere, i.e. the chemical potential of nitrogen can be tuned [11], gaseous nitriding of metallic alloys, by applying a NH_3/H_2 gas mixture at atmospheric pressure, is often applied to introduce nitrogen in the ferrite matrix at the surface of a specimen. Note that the application of specific NH_3/H_2 gas mixtures allows the adjustment of the chemical potential of nitrogen corresponding hypothetically to thousands of atmospheres of pure N_2 gas [12].

During *internal* nitriding of iron-based alloys containing alloying elements (Me) with a strong affinity for nitrogen, as Cr, Al, V and Ti, fine alloying element nitride precipitates can develop in the nitrided zone adjacent to the surface (called “diffusion zone”), which leads to a pronounced increase of the hardness of the nitrided component. The increase of hardness and related (mechanical) properties strongly depends on the amount of alloying elements, the chemical composition of the nitride precipitates, the degree of coherency of the nitride precipitates with the matrix and the precipitate size and morphology [42, 101].

Until now, most studies concerning internal nitriding have focused on binary Fe-Me alloy systems, i.e. Fe-Cr, Fe-Al, Fe-V and Fe-Ti [6, 17, 21, 25, 28, 36, 38, 102-112]. However, commercial nitriding steels often contain more than one alloying element with affinity for nitrogen. Only a few investigations were performed until now on ternary Fe-Me₁-Me₂ alloy systems. Recently, Ti-based ternary nitrides such as (Ti,Al)N, (Ti,Zr)N and (Ti,Cr)N have gained much attention as second phase particles in steels due to their contribution to the enhanced performance for cutting tools and machinery components, e.g. regarding wear/corrosion protection [113-117].

In the present work, Ti and Cr were selected as alloying elements, because both Cr and Ti, as separate alloying elements, can form nitrides which are cubic (rock-salt crystal structure), albeit of different lattice constants ($a_{\text{CrN}} = 4.13\text{\AA}$ and $a_{\text{TiN}} = 4.23\text{\AA}$). Cr and Ti have different chemical affinity for nitrogen (affinity between Ti and N is much larger than that between Cr and N (cf. Table 1.1 in chapter 1)). Both TiN and CrN exhibit a Bain orientation relationship ($\{001\}_{\text{bcc, Fe}} // \{001\}_{\text{fcc, MeN}}$, $\langle 100 \rangle_{\text{bcc, Fe}} // \langle 110 \rangle_{\text{fcc, MeN}}$) for the nitride precipitates with the ferrite matrix [24, 64, 111-112, 118].

The current project involves investigation of the nitriding behaviour of ternary Fe-Ti-Cr alloys. Different Ti/Cr atomic ratios have been employed (Ti/Cr = 0.45, 0.87 and 1.90), while keeping the total amount of alloying element at about 0.30 at.%. The microstructure of the precipitates in the nitrated zone has been investigated by means of X-ray diffraction (XRD) and transmission electron microscopy (TEM). Furthermore, the amount of absorbed nitrogen during nitriding was investigated quantitatively by the analysis of nitrogen-absorption isotherms.

5.2 Experimental

5.2.1 Specimen preparation

Ingots of Fe-Ti-Cr alloys, containing about 0.30 at.% (Ti + Cr) with varying Ti/Cr atomic ratio (0.45, 0.87 and 1.90), were prepared from pure Fe (99.98 wt.%), pure Ti (99.999 wt.%) and pure Cr (99.999 wt.%) using a light-arc furnace. The molten alloys were cast as buttons, with a shape given by a diameter of 40 mm and a height of 15 mm. The precise composition of the Fe-Ti-Cr alloys was analyzed, applying (i) inductive coupled plasma-optic emission spectroscopy (ICP-OES) to determine the content of the alloying elements Ti and Cr, (ii) a combustion method to determine the content of the light elements C and S and (iii) a hot-extraction to determine the content of the light elements O and N. The thus determined composition of the alloys is shown in Table 5.1.

The cast buttons were cold-rolled to foils with a thickness of about 0.2 mm. In order to reduce the rolling induced texture of the specimen, specimens of the as cast buttons were rolled in different directions. From the foils thus obtained rectangular specimens (15 mm × 15 mm) were cut and subsequently ground and polished. The polished specimens were encapsulated in a quartz tube filled with Ar and annealed at 800°C for 2 h to establish a recrystallized grain structure (grain size of about 30 μm). Before nitriding the specimens were ground and polished (last step: 1 μm diamond paste) and cleaned ultrasonically with ethanol.

Table 5.1: Amounts of Cr, Ti and light element impurities in the cast Fe-Ti-Cr alloys.

element alloy	Cr	Ti	Ti/Cr	N	O	S	C
	(at.%)			(μg/g)			
Fe-0.10at.%Cr- 0.19at.%Ti	0.10 (±0.01)	0.19 (±0.02)	1.90	< 10	13 ± 5	< 10	9 ± 2
Fe-0.15at.%Cr- 0.13at.%Ti	0.15 (±0.02)	0.13 (±0.01)	0.87	< 10	15 ± 5	19 ± 5	7 ± 2
Fe-0.20at.%Cr- 0.09at.%Ti	0.20 (±0.02)	0.09 (±0.01)	0.45	< 10	21 ± 5	22 ± 5	6 ± 2

5.2.2 Nitriding

For nitriding the specimens were suspended at a quartz fiber and placed in the middle of a vertical tube furnace. The gaseous nitriding experiments were performed in a flux of ammonia/hydrogen gas mixture. The fluxes of both gases were precisely adjusted with mass flow controllers. The gas flow rate was kept at 500 ml/min, which, because the inner diameter of the tube furnace is 28 mm, corresponds to a linear gas velocity of 13.5 mm/s in the furnace, which is sufficient to avoid any significant (thermal) decomposition of ammonia in the nitriding atmosphere [12].

To maintain a homogeneous precipitation morphology over the entire specimen thickness, during the determination of the absorption isotherms, pre- and denitriding steps were performed prior to the nitrogen-absorption isotherm measurements. The prenitriding step involved nitriding at 580°C for 48 h with a nitriding potential of $r_N = 0.104 \text{ atm}^{-1/2}$. After completion of this prenitriding the specimen was quenched into water at room temperature. Subsequently, the specimen was denitrided in a pure H₂ atmosphere at 470°C for 72 h.

Nitrogen-absorption isotherms were determined at a temperature of 560°C for nitriding potentials r_N in the range from 0.054 atm^{-1/2} to 0.140 atm^{-1/2} (the specimen was nitrided at each nitriding potential for 48 h; for details, see Table 5.2). The prenitriding treatment was performed at a nitriding temperature 20°C higher than the temperature applied to record the nitrogen-absorption isotherms. The prenitriding at an elevated temperature assures that the precipitation morphology of the specimens does not change during the determination of the nitrogen-

absorption isotherms. All applied nitriding treatments in the present work were performed in the α -region of the Lehrer diagram [14, 119] thus ensuring that no iron nitride formation at the specimen surface occurred.

Table 5.2: Applied nitriding parameters for the prenitriding, denitriding and nitriding experiments for determination of the nitrogen-absorption isotherms of the Fe-Ti-Cr alloys.

treatment	Temperature (°C)	Time (h)	NH ₃ (ml/min)	H ₂ (ml/min)	r _N (atm ^{-1/2})
pre-nitriding	580	48	45	455	0.104
de-nitriding	470	72	.	500	.
absorption isotherms	560	48	58	442	0.140
			50	450	0.117
			40	460	0.091
			25	475	0.054

The amount of nitrogen uptake and/or loss was determined by weight measurements after and before nitriding or denitriding using a Mettler microbalance with an accuracy of 0.1 μ g. In order to obtain an accurate weight value, the average value of ten weight measurements was taken.

5.2.3 X-ray diffraction

X-ray diffraction (XRD) analysis of the specimens before and after nitriding was performed employing a Philips X'Pert diffractometer in Bragg-Brentano geometry using Co-K α radiation and a graphite monochromator in the diffracted beam. The measurements were performed in the diffraction-angle, 2θ , range of 40° - 130° with a step size of 0.05°. The contribution of the Co-K α_2 radiation of the recorded diffractograms, was removed according to Ref. [120]. The thus corrected diffractograms were evaluated by fitting a Pearson VII profile-shape function, using TOPAS software, for the diffraction-line profiles in the diffractograms.

5.2.4 Microhardness measurement

Microhardness values before and after nitriding were obtained by carrying out hardness measurements across the cross section of specimens employing a Vickers microhardness tester (Leica VMHT Mot). A load of 100 mN, an indenter speed of 30 μ m/s and a holding time of 12 s for each indentation were applied. The distances between the indentations and the length of both

indentation-diagonals were measured with a calibrated light optical microscope (Zeiss Axiophot microscope equipped with Olympus ColorView IIIu digital camera) using analySIS Imaging software. The microhardness values reported in this chapter are the average of five measurements made at the same depth of the specimen cross-section.

5.2.5 Transmission electron microscopy

Foils for transmission electron microscopy (TEM) were prepared from the middle of the nitrided zone. Discs ($\Phi = 3\text{mm}$) were stamped with a mechanical punch from sheets produced by removing material mechanically from both sides (faces) of a nitrided specimen. These discs were thinned, to obtain an electron-transparent area, applying the jet-electropolishing technique employing a Struers Tenupol-3 apparatus (bath composition: 85 vol. % acetic acid and 15 vol. % perchloric acid, current: $24\text{ mA} \leq I \leq 42\text{ mA}$, voltage: 19.5 V, temperature: 278K, flow rate setting: “20”, and treatment time: $174\text{ s} \leq t \leq 242\text{ s}$) and subsequently rinsed in ethanol, acetone and isopropanol.

TEM analysis was performed using a Philips CM 200 transmission electron microscope operated at 200kV. Bright field (BF) images and selected area diffraction patterns (SADPs) were taken by a Gatan CCD camera.

5.2.6 Electron probe microanalysis

To determine the (depth) distribution of the alloying elements and nitrogen after nitriding of the specimens, electron probe microanalysis (EPMA) was performed on specimen cross sections employing a Cameca SX100 instrument. Pieces of the specimen were cut to prepare cross-sections by subsequently embedding of these pieces with a Polyfast (Struers, a conductive bakelite resin with carbon filler embedding material), followed by grinding and polishing (last step: 1 μm diamond paste). A focused electron beam at an accelerating voltage of 15 kV and a current of 100 nA was applied. To obtain the element contents in the specimens, the intensities of the characteristic Ti-K α , Cr-K α , Fe-K β and N-K α X-ray emission peaks were determined at points separated at distances of 2 μm along lines perpendicular to the surface of the specimen in the specimen cross section. The concentrations of Ti, Cr and Fe were determined on the basis of the ratio of the corresponding characteristic X-ray emission peak intensity of the specimen and that of a standard specimen (i.e. pure Ti, pure Cr and pure Fe) by applying the $\Phi(\rho z)$ -correction [56].

For the determination of the characteristic X-ray emission peak of nitrogen a correction procedure had to be applied, because of severe overlap of the N-K α and Ti-L1 X-ray emission peaks. The correction procedure, known as *ratio method*, is as follows [121]:

- (i) EMPA analysis of the nitrided Fe-Ti-Cr alloy specimen (“SPE”), provides the intensity $I_{Ti-K\alpha}^{SPE}$ and the total intensity at the 2 θ position of the N-K α , $I_{tot(N)}^{SPE}$, which intensity consists of contribution from both $I_{N-K\alpha}^{SPE}$ and $I_{Ti-L1(N)}^{SPE}$ at the 2 θ position of N-K α .
- (ii) The 2 θ position and standard intensity of the N-K α X-ray emission peak are obtained using γ' -Fe₄N as a standard material.
- (iii) Intensities of the Ti-K α emission peak ($I_{Ti-K\alpha}^{STD}$ at its own specific 2 θ value) and of the Ti-L1 emission peak at the 2 θ position of the N-K α ($I_{Ti-L1(N)}^{STD}$) are obtained using a pure Ti standard specimen (“STD”).
- (iv) Assuming a constant Ti-L1(N) and Ti-K α intensity ratio for standard (“STD”) and nitrided specimen (“SPE”), i.e. ignoring a possible emission peak shift between standard material and the specimen, a correction factor, CF can be given as follows;

$$CF = \left(\frac{I_{Ti-L1(N)}^{STD}}{I_{Ti-K\alpha}^{STD}} \right) = \left(\frac{I_{Ti-L1(N)}^{SPE}}{I_{Ti-K\alpha}^{SPE}} \right) \quad (1)$$

- (v) The nitrogen intensity, $I_{N-K\alpha}^{SPE}$, can now be calculated from $I_{tot(N)}^{SPE}$ and $I_{Ti-K\alpha}^{SPE}$:

$$\begin{aligned} I_{N-K\alpha}^{SPE} &= I_{tot(N)}^{SPE} - I_{Ti-L1(N)}^{SPE} \\ &= I_{tot(N)}^{SPE} - CF * I_{Ti-K\alpha}^{SPE} \end{aligned} \quad (2)$$

Finally, the concentration of nitrogen is obtained from the ratio of the thus obtained N-K α intensity of the specimen and that of the standard material (γ' -Fe₄N), applying the $\Phi(\rho z)$ approach (see above).

5.3 Results and evaluation

5.3.1 The nitrided microstructure

X-ray diffractograms were taken from the specimen surface before and after nitriding for all Fe-Ti-Cr alloys (Ti/Cr atomic ratio = 0.45, 0.87 and 1.90). Only ferrite reflections appear in the diffractograms. For all alloys, the diffraction peaks of the ferrite, particularly the 200 α -Fe

reflection, had strongly broadened after nitriding (Figs. 5.1a-c). The occurrence of pronounced diffraction-line broadening of the ferrite reflexes upon nitriding, without the appearance of separate alloying element nitride reflections, can be ascribed to the development of microstrain due to the formation of (largely) coherent precipitates in the ferrite matrix which diffract coherently with the matrix, as discussed in Ref. [7]. In addition to the observed broadening of the 200 α -Fe diffraction line, an intensity hump arises at the high-angle side of the 200 α -Fe reflection. It becomes more pronounced with increasing Ti/Cr atomic ratio of the specimen (see, especially, the intensity data within the dashed circle in Fig. 5.1d).

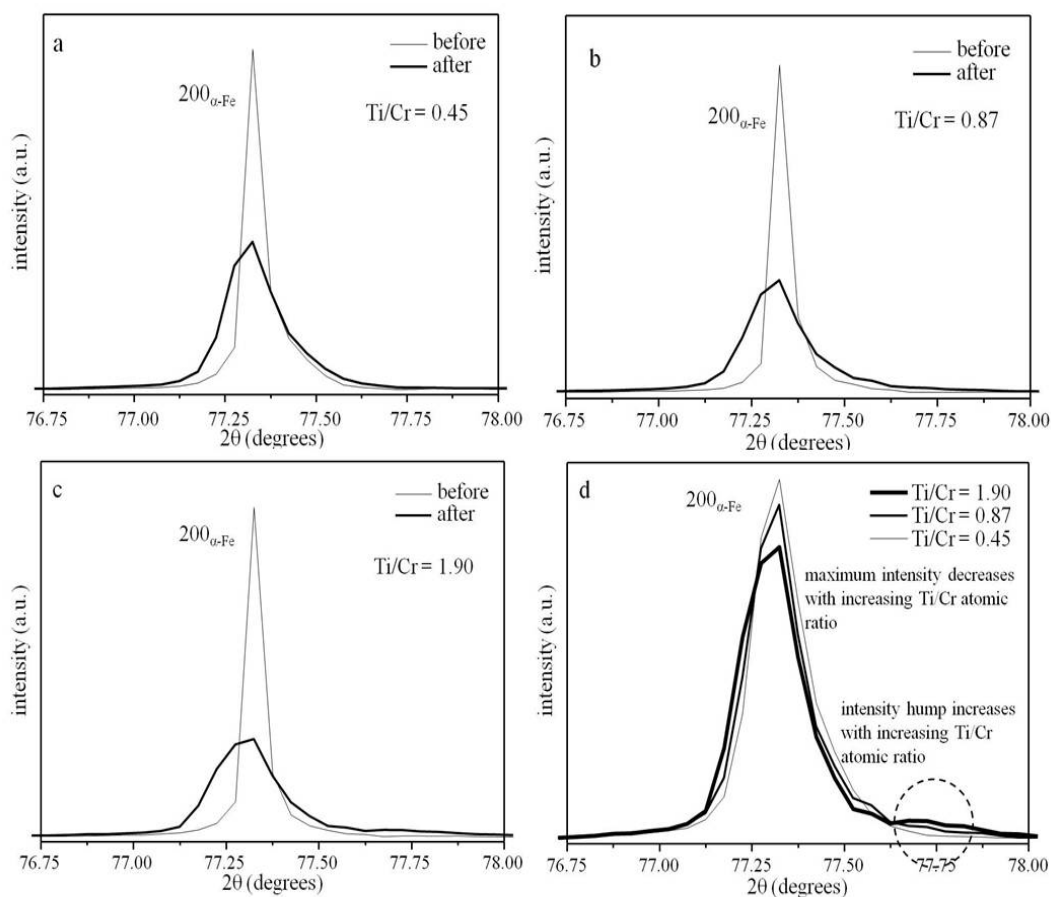


Fig. 5.1: X-ray diffractograms of the 200 α -Fe reflection ($76.5^\circ < 2\theta < 78.5^\circ$, Co-K α radiation, step size 0.05° ; normalized with respect to the integral intensity) before and after nitriding of the Fe-Ti-Cr alloy concerned; (a) Ti/Cr = 0.45, (b) Ti/Cr = 0.87, (c) Ti/Cr = 1.90; (d) composite of all 200 α -Fe reflections (a - c) after nitriding. The nitriding experiments were performed at 580°C for 48 h with nitriding potential $r_N = 0.104 \text{ atm}^{-1/2}$.

TEM bright field (BF) and corresponding selected area diffraction patterns (SADPs) of nitrated Fe-Ti-Cr alloys with Ti/Cr = 0.45 and 1.90 are shown in Figs. 5.2a and b, respectively. The electron-beam direction in both SADPs is close to (i.e. does not coincide exactly with) the

[001] zone axis of the ferrite, in order to avoid strong diffraction by the matrix and to reveal the presence of the precipitates by their diffraction contrast. The TEM BF diffraction-contrast images show an ultra-thin platelet morphology of the nitride precipitates in the ferrite matrix (see the dotted circles in the BF images, which indicate regions showing the typical coffee-bean contrast due to the misfit-strain between the thin nitride platelets and the ferrite matrix for platelets parallel to the $[001]_{\alpha\text{-Fe}}$ electron beam/zone axis; the nitride platelets in the dotted circles are parallel to $(100)_{\alpha\text{-Fe}}$ matrix lattice planes (see below)). The size of the platelets (length ≤ 30 nm and thickness ≤ 3 nm) does not depend significantly on the Ti/Cr atomic ratio.

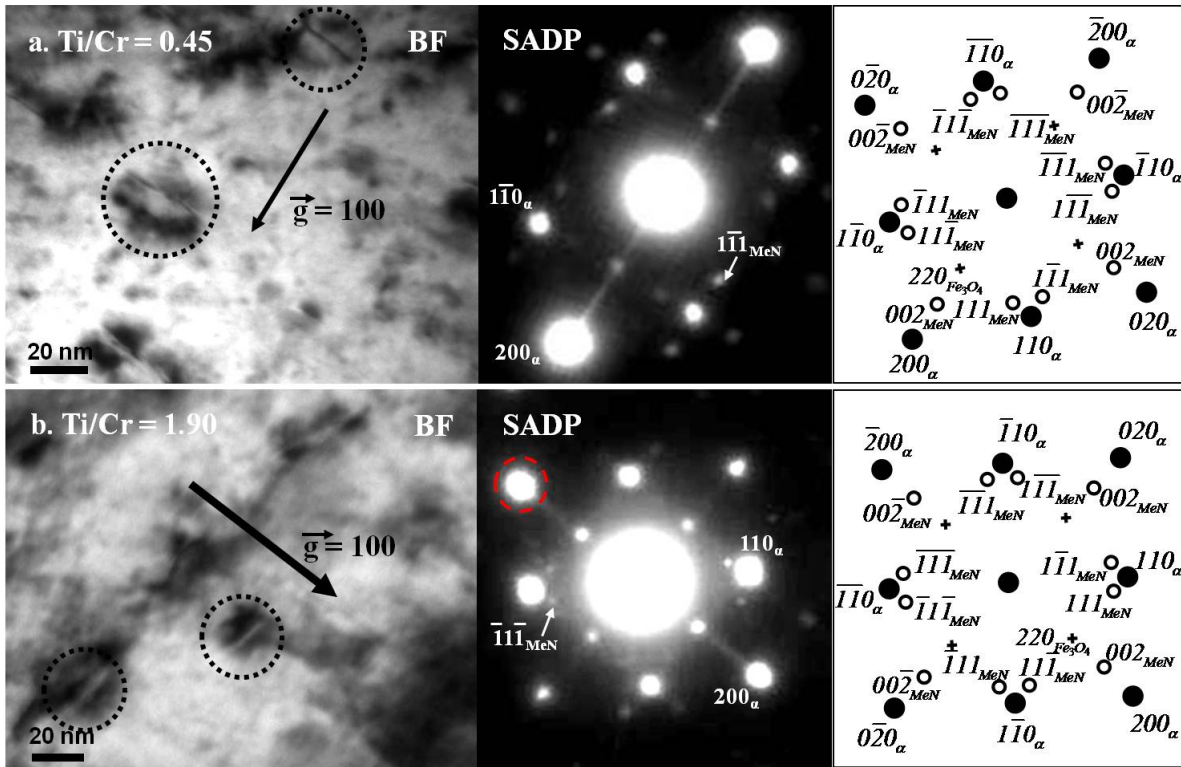


Fig. 5.2: TEM BF images (left) showing diffraction contrast due to fine (misfitting) $\text{Ti}_{1-x}\text{Cr}_x\text{N}$ nitride platelets in the ferrite matrix. (a) $\text{Ti}/\text{Cr} = 0.45$ and (b) $\text{Ti}/\text{Cr} = 1.90$. The dotted open circles in the BF images indicate locations where fine nitride platelets had developed, giving rise to misfit-strain field induced “coffee-bean” contrast. The SADPs (middle) were taken at electron-beam directions close to $[001]_{\alpha\text{-Fe}}$. The SADP of the Fe-Ti-Cr, $\text{Ti}/\text{Cr} = 1.90$ alloy in (b) shows elongated $200_{\alpha\text{-Fe}}$ diffraction spots (see dashed circle), which is composed of a cubic ferrite 200 diffraction spot and a 200 diffraction spot originating from tetragonally strained ferrite (see text). Schematic diffraction patterns (right), corresponding with the SADPs shown, for the concerned electron-beam, i.e. $[001]_{\alpha\text{-Fe}}$ direction and nitride precipitates complying with a Bain orientation relationship with the $\alpha\text{-Fe}$ matrix (black dots: diffraction spots of the ferrite matrix; unfilled circles: diffraction spots of the nitride precipitates).

The SADPs show pronounced streaks through the 200 α -Fe diffraction spots in the $\langle 100 \rangle$ α -Fe directions and additional diffraction spots near the 110 α -Fe diffraction spots corresponding with a lattice spacing, d , which is compatible with the spacing of the {111} lattice planes of a cubic, rock-salt structure-type nitride (MeN). Moreover, particularly for the highest Ti/Cr ratio (see SADP in Fig. 5.2b), the 200 α -Fe diffraction spots have split into two; one corresponding to cubic ferrite (d_{200} of cubic ferrite from SADP = 1.43 Å) and another one corresponding to tetragonally distorted ferrite.

The intensity hump observed in the X-ray diffractograms at the high-angle side of the 200 α -Fe reflection (see dashed circle in Fig. 5.1d) is compatible with the occurrence of a split 200 α -Fe spot in the SADP shown in Fig. 5.2b. As demonstrated here by fitting (using a Pearson VII profile-shape function) to the overall 200 α -Fe reflection shown in Fig. 5.1c, the overall reflection is composed of two peaks (see Fig. 5.3 for the nitrated Fe-Ti-Cr alloy with Ti/Cr = 1.90): one is ascribed to a cubic ferrite 200 reflection (d_{200} of cubic ferrite = 1.43 Å) and the other one is ascribed to the 200/002 doublet reflection of tetragonally distorted ferrite (d_{200} of tetragonal ferrite = 1.43 Å, d_{002} of tetragonal ferrite = 1.42 Å).

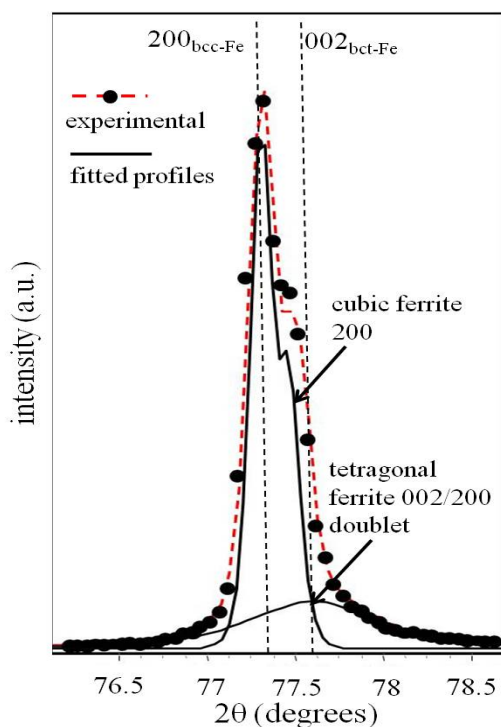


Fig. 5.3: Contributions of the 200 reflection of the (cubic, bcc) ferrite and the 200/002 doublet reflection of the tetragonally distorted (bct) ferrite to the total observed diffraction profile as evaluated by fitting a Pearson VII profile-shape function for the various reflection contributions (Ti/Cr = 1.90).

The fit of the tetragonal doublet and cubic reflections to the measured intensity data, as shown in Fig. 5.3, was performed adopting the procedure described in Ref. [7] (Note that in Ref. [7] the c and a lattice parameters of the bct phase have been, unconventionally, defined such that $c = b$ instead of $a = b$). These d -spacings, derived from the XRD pattern, are well compatible with the split 200 α -Fe diffraction spot in the SADP shown in Fig. 5.2b.

The positions in the SADPs of the 111 MeN diffraction spots, near the 110 α -Fe diffraction spots and ascribed to the face centred cubic, rock-salt type MeN structure, are compatible with the occurrence of a Bain orientation relationship of cubic, rock-salt structure type MeN precipitates with the bcc ferrite matrix, $\{001\}_{\text{bcc}} // \{001\}_{\text{fcc}}$, $\langle 100 \rangle_{\text{bcc}} // \langle 110 \rangle_{\text{fcc}}$ (Refs. [7] and [8]).

The nitride platelets develop with $\{001\}_{\alpha\text{-Fe}}$ lattice planes as habit planes. The mismatch of the nitride platelet with the ferrite matrix is such that, in order to maintain coherency, the ferrite matrix in the immediate surroundings of the nitride platelets is anisotropically, tetragonally deformed: A compressive misfit stress develops in the directions normal to the platelet (i.e. in a $\langle 001 \rangle_{\alpha\text{-Fe}}$ direction), whereas a tensile misfit stress develops parallel to the platelet faces (i.e. in $\langle 100/010 \rangle_{\alpha\text{-Fe}}$ directions). The surrounding ferrite matrix of the nitride platelet can thus be considered as a bct phase (see Fig. 5.4).

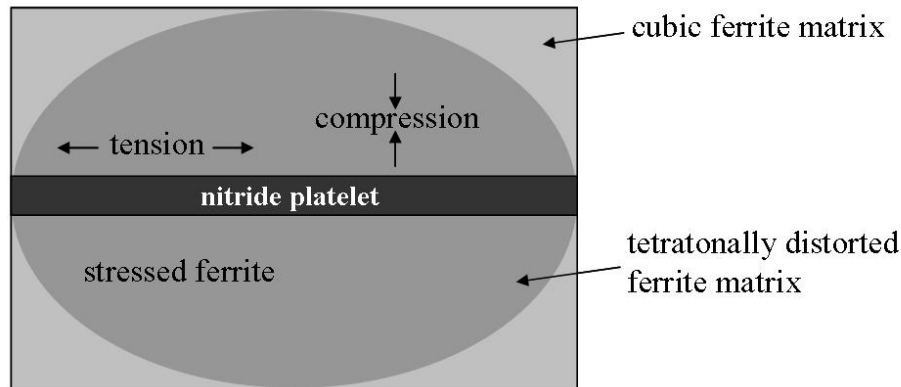


Fig. 5.4: Schematic presentation of a misfitting coherent nitride platelet and the surrounding ferrite matrix, and the associated state of stress in the matrix [7].

If precipitates of CrN and TiN would have developed separately in the ferrite matrix during nitriding, the diffraction spots of both nitrides should be distinguishable (in the SADPs). However, the SADPs show only singular 111 reflections of a cubic, rock-salt crystal structure type MeN nitride. This suggests that Ti and Cr have precipitated together in a cubic, rock-salt type mixed, $\text{Ti}_{1-x}\text{Cr}_x\text{N}$ nitride (such mixed precipitation, leading to a metastable precipitate, $(\text{Me}_1, \text{Me}_2)\text{N}$, in principle prone to decomposition into the two equilibrium precipitates, Me_1N and Me_2N , was

observed for the first time upon nitriding Fe-Cr-Al alloys [8]). The d-spacing measured from the 111 reflection of the mixed $Ti_{1-x}Cr_xN$ ($Ti/Cr = 0.45$) is 2.41 \AA , which (indeed) is in-between the 111 d-spacing of CrN (2.38 \AA) and the 111 d-spacing of TiN (2.44 \AA). Furthermore, the lattice parameter derived from the 111 reflection of mixed $Ti_{1-x}Cr_xN$ with $Ti/Cr = 0.45$ (see above), which is 4.17 \AA , agrees well with that reported for a $(Ti, Cr)N$ ($Ti/Cr = 0.45$) film produced by reactive cathodic sputtering [122-123].

The lattice parameters of mixed $Ti_{1-x}Cr_xN$ nitride, as derived from the reflections recorded in the SADPs, are shown as function of the relative Ti content in Fig. 5.5, together with those pertaining to pure CrN and pure TiN. Evidently, the lattice parameter of mixed $Ti_{1-x}Cr_xN$ nitride increases linearly with increasing relative Ti content, indicating that the substitutional solid solution of Ti and Cr in the mixed nitride complies with Vegard's law. This provides further support for the above interpretation implying that mixed $Ti_{1-x}Cr_xN$ nitride forms upon nitriding.

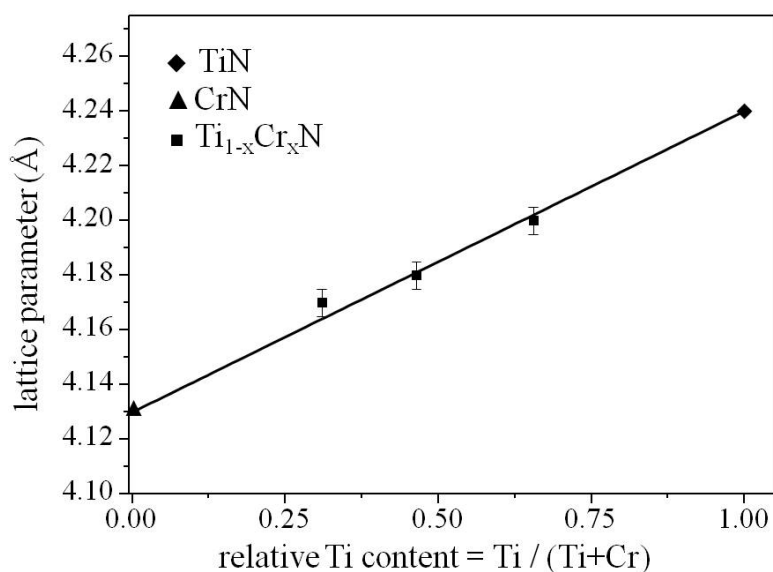


Fig. 5.5: Lattice parameters of pure CrN (open triangle), pure TiN (open diamond) and mixed $Ti_{1-x}Cr_xN$ (open squares) as a function of relative Ti atomic content (relative with respect to the total amount of alloying elements, i.e. $Ti + Cr$).

5.3.2 Quantitative analysis of excess nitrogen uptake

A nitrogen-absorption isotherm shows the dependence of the amount of nitrogen taken up by a (homogeneously) nitrated specimen as function of the nitriding potential, r_N (directly related to the chemical potential of nitrogen absorbed in the ferrite matrix for a given nitriding atmosphere [11]). The analysis of nitrogen-absorption isotherms allows distinction of various kinds of differently (chemically) bonded nitrogen.

The amount of nitrogen absorbed in the ferrite matrix upon nitriding by means of an NH_3/H_2 gas mixture can be described by the equilibrium:



where $[N]_{\alpha}$ is the concentration of nitrogen dissolved interstitially in the ferrite matrix. The solubility of nitrogen in ferrite matrix, $[N]_{\alpha}$, is proportional to the nitriding potential, r_N , according to

$$[N]_{\alpha} = K \times r_N \quad (4)$$

where K is the equilibrium constant for Eq. (3) and where it has been assumed that the activity coefficient of the nitrogen atoms is constant and has been incorporated in K [11]. Any point on a nitrogen-absorption isotherm indicates the equilibrium amount of nitrogen absorbed by the specimen at a given nitriding potential. To determine experimentally nitrogen-absorption isotherms, it is essential to establish a homogeneous, constant nitrogen content throughout the cross-section of the specimen. Further, the precipitation morphology should not change during determination of the absorption isotherm. Therefore the preceding prenitriding treatment (cf. section 5.2.2) is performed at a temperature higher than applied for determination of the absorption isotherm, to ensure a constant precipitate morphology. It has been verified that such conditions have been realized in the present work (see what follows).

Elemental concentration-depth profiles determined for the entire cross section of the specimens (pre)nitrided at 580°C for 48 h (EPMA data) are shown in Figs. 5.6a-c for the alloys with Ti/Cr = 0.45, 0.87 and 1.90, respectively. Evidently, after the homogeneous nitriding, the nitrogen uptake is larger than the amount of nitrogen required for the precipitation of all Ti and Cr as mixed $Ti_{1-x}Cr_xN$ nitride, $[N]_{Ti_{1-x}Cr_xN}$, plus the amount of nitrogen necessary to establish the equilibrium solubility in an unstrained ferrite matrix, $[N]_{\alpha}^{\circ}$. This so-called amount of “normal” nitrogen, $[N]_{nor} \equiv [N]_{Ti_{1-x}Cr_xN} + [N]_{\alpha}^{\circ}$, has been indicated by the horizontal-dashed line in Figs. 5.6a-c. The difference between the experimentally obtained total amount of nitrogen, $[N]_{tot}$, and the amount of “normal” nitrogen, $[N]_{nor}$, is defined as excess nitrogen, $[N]_{ex}$ (for details see section 1.4 of chapter 1).

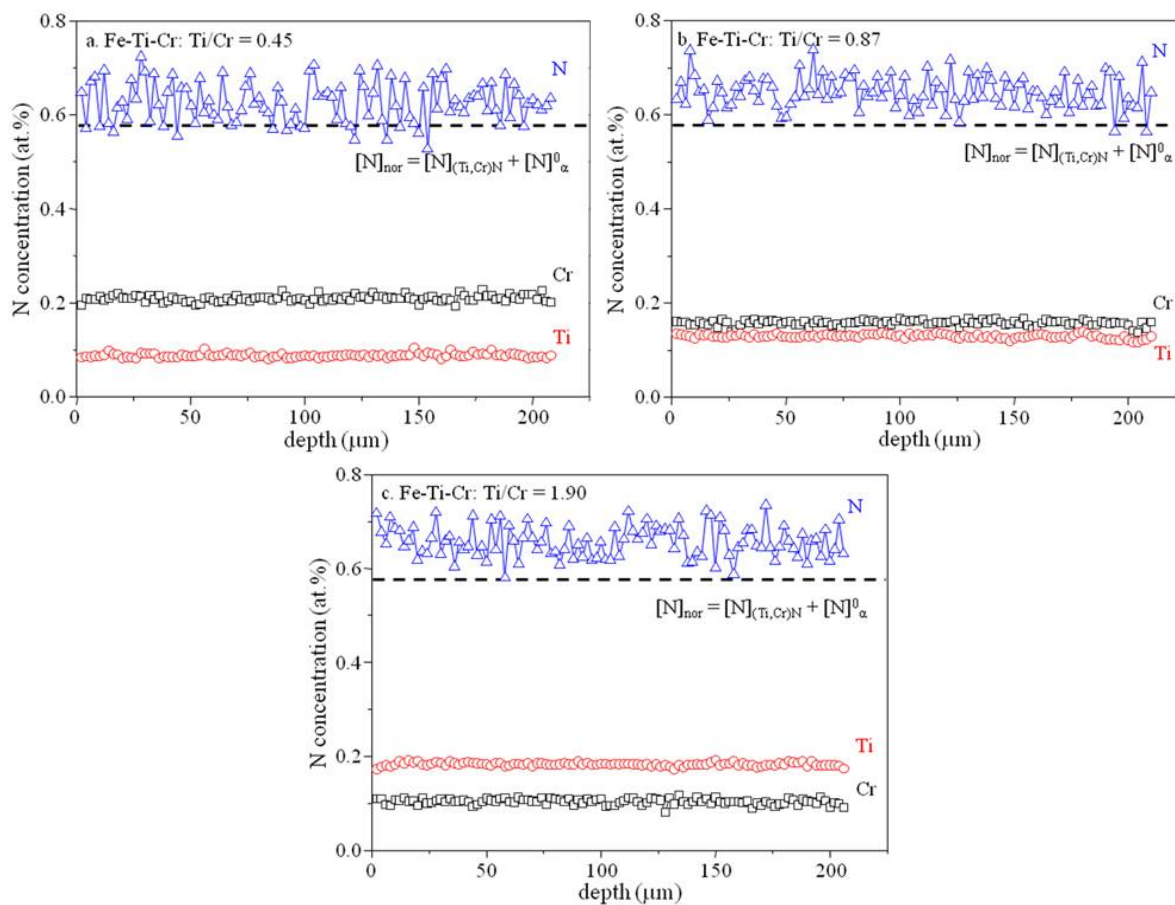


Fig. 5.6: N, Ti and Cr (EPMA) concentration-depth profiles measured for the entire cross sections of nitrated Fe-Ti-Cr specimens (a) Ti/Cr = 0.45, (b) Ti/Cr = 0.87 and (c) Ti/Cr = 1.90 after pre-nitriding (48 h at 580°C with $r_N = 0.104 \text{ atm}^{-1/2}$). The dashed horizontal line denotes the amount of “normal” nitrogen.

After prenitriding, the specimens were subsequently denitrated in a pure H_2 (500 ml/min) atmosphere at 470°C for 72 h. After the denitrating step, the nitrogen content which remains in the specimen was determined by weighing. The remaining nitrogen content in the Fe-Ti-Cr alloys amounts to 0.25 (± 0.04), 0.25 (± 0.01) and 0.26 (± 0.01) at.%⁸ for the alloys with Ti/Cr = 0.45, 0.87 and 1.90, respectively, which can be fully attributed to nitrogen strongly bonded to Ti and Cr in corresponding nitride precipitates $\text{Ti}_{1-x}\text{Cr}_x\text{N}$. This indicates that all excess nitrogen was removed from the specimens by the denitrating treatment.

The nitrogen-absorption isotherms for each specimen (after prenitriding and denitrating, as discussed above) are shown in Figs. 5.7a-c for the alloys with Ti/Cr = 0.45, 0.87 and 1.90,

⁸ The error ranges indicated were taken equal to the *maximal* deviation from the average value calculated on the basis of the ten weight measurements before and after (de)nitriding.

respectively. A straight line (dashed line in Figs. 5.7a-c) can well be fitted (least squares analysis) to the data points representing the total amount of absorbed nitrogen.

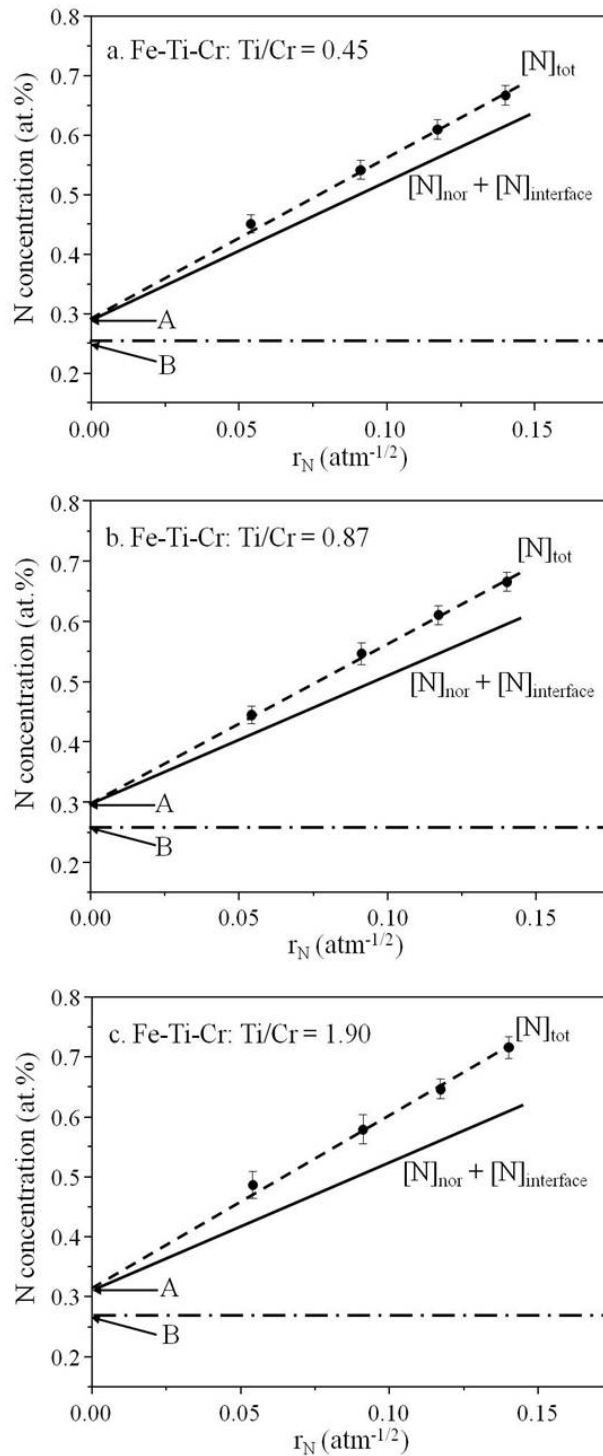


Fig. 5.7: Nitrogen-absorption isotherms after successive prenitriding and denitriding treatments for Fe-Ti-Cr alloys (a) Ti/Cr = 0.45, (b) Ti/Cr = 0.87 and (c) Ti/Cr = 1.90. The linear portions of the nitrogen-absorption isotherms have been indicated by the dashed lines which intersect the ordinates at $r_N = 0$ at nitrogen levels indicated by A. The nitrogen levels after de-nitriding (horizontal dash-dot lines) have been indicated by B.

The extrapolation to $r_N = 0$ yields the data point ‘A’ on the ordinate as shown in Figs. 5.7a-c. The nitrogen level indicated with ‘B’ on the ordinate in Figs. 5.7a-c represents the amount of nitrogen required for the formation of stoichiometric mixed $Ti_{1-x}Cr_xN$ nitride precipitates (i.e. $[N]_{Ti_{1-x}Cr_xN}$), i.e. the (measured) amount of nitrogen remaining after denitriding (see above). Hence, in line with the reasoning applied for e.g. Fe-V [109] and Fe-Cr [102] alloys, it is suggested that the difference $A - B$ can be ascribed to (excess) nitrogen adsorbed at the interface between nitride precipitate and ferrite matrix, $[N]_{interface}$. The thus obtained $[N]_{interface}$ values have been gathered, together with the values of levels A and B, in Table 5.3 and Fig. 5.8a.

The composition of a $Ti_{1-x}Cr_xN$ precipitate together with the interfacial adsorbed excess nitrogen, $[N]_{interface}$, can be described as $Ti_{1-x}Cr_xN_y$, where

$$y = \frac{[N]_{Ti_{1-x}Cr_xN} + [N]_{interface}}{[N]_{Ti_{1-x}Cr_xN}} = \frac{level\ A}{level\ B} \quad (5)$$

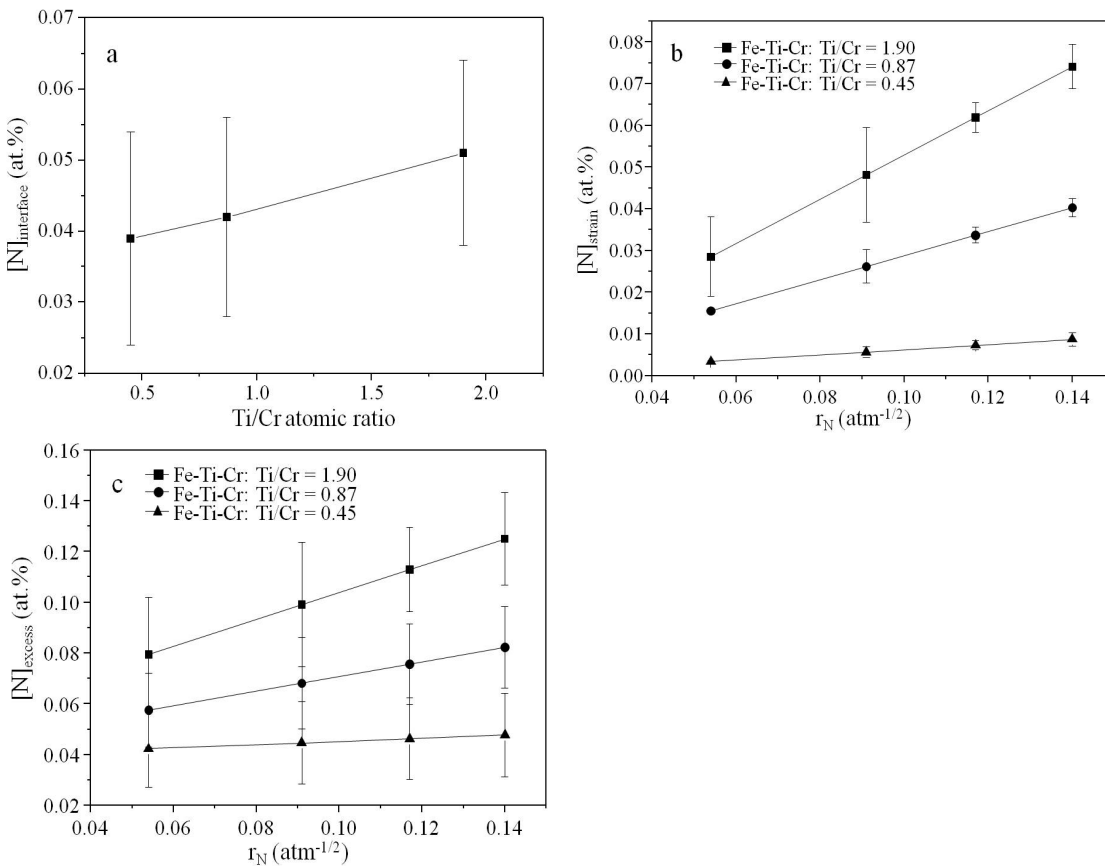


Fig. 5.8: Excess nitrogen (a) adsorbed at the nitride precipitates/ferrite matrix interface, $[N]_{interface}$, as function of Ti/Cr atomic ratio (b) dissolved interstitially in the ferrite matrix due to the presence of a misfit-strain field, $[N]_{strain}$ and (c) total amount of excess nitrogen ($= [N]_{interface} + [N]_{strain}$) for Fe-Ti-Cr alloys (Ti/Cr = 0.45, 0.87 and 1.90) as function of the nitriding potential, r_N .

Table 5.3: The values of nitrogen uptake at level A (interception of the dashed line in Figs. 5.7a-c with the ordinate, i.e. at nitriding potential, $r_N = 0$), at level B (as obtained after denitriding) and the accordingly calculated amount of nitrogen adsorbed at the interface nitride-precipitate/ferrite matrix, $[N]_{interface}$ (i.e. $A - B$).

alloy	A (at.%)	B (at.%)	$[N]_{interface}$ (at.%)
Fe-Ti-Cr: Ti/Cr = 0.45	0.290	0.251 (± 0.015)	0.039 (± 0.015)
Fe-Ti-Cr: Ti/Cr = 0.87	0.296	0.254 (± 0.014)	0.042 (± 0.014)
Fe-Ti-Cr: Ti/Cr = 1.90	0.311	0.260 (± 0.013)	0.051 (± 0.013)

The value of y thus obtained contains indirect information on the average thickness of the precipitate platelet. As shown above (see section 5.3.1), $Ti_{1-x}Cr_xN$ precipitates develop as platelets of cubic, rock-salt crystal structure type obeying a Bain orientation relationship with the ferrite matrix. With $\{001\}$ of $Ti_{1-x}Cr_xN$ as a habit plane, the thickness of a monolayer of $Ti_{1-x}Cr_xN$ is one half of the lattice parameter of the rock-salt crystal structure type (i.e. $\frac{a_{Ti_{1-x}Cr_xN}}{2}$). If at every octahedral interstice in the ferrite matrix at the nitride/matrix interface one excess nitrogen atom is trapped, it follows

$$y = \frac{n + 2}{n} \quad (6)$$

where n is the number of $Ti_{1-x}Cr_xN$ monolayers comprising the platelet. Thus the thickness t of a $Ti_{1-x}Cr_xN$ platelet follows from

$$t = n \times \frac{a_{Ti_{1-x}Cr_xN}}{2} = \frac{a_{Ti_{1-x}Cr_xN}}{y - 1} \quad (7)$$

Using lattice-parameter data of mixed $Ti_{1-x}Cr_xN$ nitride as obtained in this work (see Fig. 5.5) the thus obtained nitride-platelet thickness values have been gathered in Table 5.4 together with the corresponding y values. These deduced thickness values obtained are well compatible with the data obtained by the TEM investigations (see section 5.3.1).

Table 5.4: The value of y in $Ti_{1-x}Cr_xN_y$ and the accordingly deduced (see text) average thickness of the $Ti_{1-x}Cr_xN$ platelets for Fe-Ti-Cr alloys with atomic ratio Ti/Cr = 0.45, 0.87 and 1.90.

alloy	y in $Ti_{1-x}Cr_xN_y$	average thickness of platelets (nm)
Fe-Ti-Cr: Ti/Cr = 0.45	1.16	2.6
Fe-Ti-Cr: Ti/Cr = 0.87	1.18	2.3
Fe-Ti-Cr: Ti/Cr = 1.90	1.20	2.1

As follows from Eq. (4), $[N]_{\alpha} = [N]_{tot} - A$ represents the amount of nitrogen dissolved in the ferrite matrix. The normal amount of dissolved nitrogen, $[N]_{\alpha}^{\circ}$, is represented by $[N]_{\alpha}^{\circ} = [N]_{nor} + [N]_{interface} - A$; see the full line indicated with $[N]_{nor} + [N]_{interface}$ in Figs. 5.7a-c. The difference between the dashed and full straight lines represents excess nitrogen dissolved in the ferrite matrix. This dissolved excess nitrogen, $[N]_{strain}$, is due to the presence of strain fields around the misfitting nitride precipitates [24]. Positive volumetric misfit is associated with the precipitation of nitride precipitates in the ferrite matrix. Assuming fully elastic accommodation of this misfit, a finite matrix shows positive lattice dilation. The matrix-lattice dilation generated by the misfitting nitrides, induced by the hydrostatic component of the image-stress field of finite bodies, provides a geometrical understanding for the occurrence of an enhanced amount of dissolved nitrogen.

From the slope of the extrapolated straight dashed line, S , the amount of $[N]_{strain}$ can be calculated:

$$S = \frac{\Delta[N]_{\alpha}}{\Delta r_N} = \frac{\Delta[N]_{\alpha}^{\circ} + \Delta[N]_{strain}}{\Delta r_N} = S_{\alpha}^{\circ} + \frac{\Delta[N]_{strain}}{\Delta r_N} \quad (8)$$

The value of S_{α}° at a given nitriding temperature can be obtained from the nitriding behavior of pure α -Fe (such data used here have been taken from Ref. [27]). Hence from the slope S the value of $[N]_{strain}$ can be given as fraction of r_N : see Fig. 5.8b. It follows that $[N]_{strain}$ increases distinctly with increasing Ti/Cr atomic ratio. This suggests that the level of microstrain in the ferrite matrix increases with increasing Ti/Cr atomic ratio.

This result is compatible with the measured microhardness data: the average microhardness of the specimens before and after nitriding is shown in Fig. 5.9 as a function of the Ti/Cr atomic ratio. The hardness of the nitrated specimen increases significantly with increasing Ti/Cr ratio. This result is compatible with the X-ray diffraction data which indicate an

increase of microstrain level with increasing Ti/Cr atomic ratio (see the XRD results and their discussion in section 5.3.1).

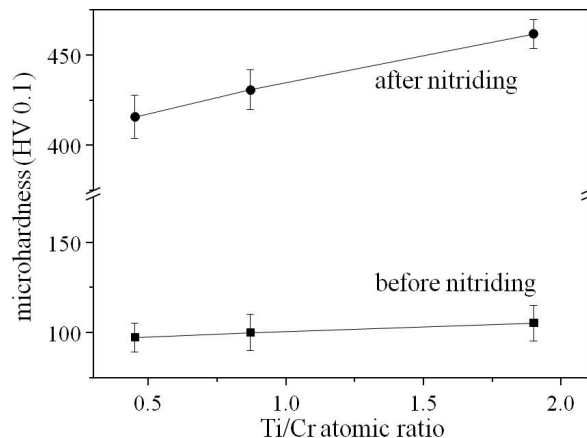


Fig. 5.9: Microhardness of the Fe-Ti-Cr alloys (Ti/Cr = 0.45, 0.87 and 1.90) before and after nitriding as a function of their Ti/Cr atomic ratio. The error ranges indicated were taken equal to the maximal deviation from the average value (10 measurements) for each data point.

The total amount of excess nitrogen is given by the sum of $[N]_{strain}$ (dependent on r_N) and $[N]_{interface}$ (independent of r_N): $[N]_{excess} = [N]_{strain} + [N]_{interface}$. Evidently, as $[N]_{strain}$, $[N]_{interface}$ also increases with increasing Ti/Cr atomic ratio (cf. Fig. 5.8).

5.4 General discussion: the role of the Ti/Cr atomic ratio

During nitriding of ferritic ternary Fe-Ti-Cr alloys cubic, rock-salt type crystal structure, mixed $Ti_{1-x}Cr_xN$ nitride platelets precipitate. The chemical affinity of Ti for N to precipitate as TiN is much larger than that of Cr for N to precipitate as CrN (cf. section 1.3 of chapter 1) [24]. This suggests a much larger driving force for Ti than for Cr to precipitate as nitride upon nitriding. There is no difficulty for the mixed nitride to form in the cubic, rock-salt type crystal structure: both TiN and CrN have this crystal structure. In particularly considering the misfit-strain development upon formation of nitride precipitates in the ferrite matrix, it follows that uptake of Cr in TiN can be favoured because it leads to reduction of the misfit strain with the surrounding ferrite matrix (see below). On this basis it can be suggested that the Cr atoms are “dragged” into the developing cubic, rock-salt structure type TiN precipitates, thereby forming mixed $Ti_{1-x}Cr_xN$ nitride.

The mixed $Ti_{1-x}Cr_xN$ nitride platelets exhibit a Bain orientation relationship with the ferrite matrix with $\{001\}$ α -Fe habit planes parallel to the platelet faces. The platelet morphology

is a consequence of the strongly anisotropic misfit strain with the surrounding ferrite matrix: the linear misfits of the mixed $Ti_{1-x}Cr_xN$ nitride platelet ($Ti/Cr = 0.45$) along and perpendicular to the $\{001\}$ α -Fe habit planes are about 3.8 % and 47 %, respectively. This anisotropic nature of the misfit strain field, together with the coherent nature of the interface between nitride platelets and ferrite matrix, induces the tetragonal distortion of the ferrite matrix adjacent to the nitride platelets (Fig. 5.4).

The lattice parameter of mixed $Ti_{1-x}Cr_xN$ nitride increases with increasing Ti/Cr atomic ratio (cf. Fig. 5.5). In view of the Bain orientation relationship and the lattice parameter of pure α -Fe this implies that the misfit-strain field surrounding the precipitates becomes more pronounced with increasing atomic Ti/Cr ratio. As a consequence a significant hardness increase occurs with increasing atomic Ti/Cr ratio (the minor differences in the total amounts of nitrogen dissolved in the ferrite matrix (cf. data for $[N]_{tot-A}$ in Fig. 5.7) cannot cause this effect; see also Fig. 3 in Ref. [95]). Indeed, the diffraction-line broadening observed for the ferrite matrix and the tetragonal distortion of the ferrite matrix as revealed by the intensity hump at the high-angle side of the 200 α -Fe reflection increase with increasing Ti/Cr atomic ratio (cf. Fig. 5.1d).

The coherent nature of the nitride platelet/matrix interface makes adsorption of nitrogen at the octahedral interstices in the ferrite matrix *adjacent to* the platelet faces likely, as in this way bonding to Ti and/or Cr in the platelet is realized, i.e. $[N]_{interface}$. Because the affinity of Ti for N is much higher than that of Cr for N, $[N]_{interface}$ increases with Ti/Cr, as observed (Fig. 5.8a). A similar observation was made for nitrided Fe-Cr-Al alloys where $[N]_{interface}$ increases with increasing Al/Cr atomic ratio [10]. Moreover, for increasing Ti/Cr atomic ratio the nitride-platelet thickness decreases (Table 5.4) implying that the amount of interfacial area between nitride precipitates and the matrix increases with increasing Ti/Cr atomic ratio. Obviously this effect contributes to an increase of $[N]_{interface}$ with increasing Ti/Cr atomic ratio, as well.

The presence of dissolved excess nitrogen in the ferrite matrix upon nitriding of Fe-Ti-Cr alloys is a consequence of elastic accommodation of the misfit between nitride platelet and ferrite matrix: such elastic accommodation of misfit induces a tensile hydrostatic stress component in the ferrite matrix [24]. As a consequence, as compared to the unstrained state, more nitrogen can be dissolved (on octahedral interstices) in the ferrite matrix; i.e. $[N]_{strain}$. Because the misfit increases with increasing Ti/Cr atomic ratio (see above), $[N]_{strain}$ increases with increasing Ti/Cr atomic ratio, as observed (Fig. 5.8b).

5.5 Conclusions

1. Upon nitriding of ternary iron-based Fe-Ti-Cr alloys highly coherent cubic, rock-salt crystal-structure type, mixed $Ti_{1-x}Cr_xN$ nitrides develop in the ferrite matrix. Separate TiN and CrN nitrides do not develop. Uptake of Cr in TiN is favored as it reduces the misfit-strain field in the ferrite matrix.
2. The misfit of the largely coherent nitride precipitates with the surrounding ferrite matrix is strongly anisotropic. As a consequence the nitride precipitates develop as platelets (length ≤ 30 nm and thickness ≤ 3 nm) obeying a Bain orientation relationship with the ferrite matrix with $\{100\}\alpha\text{-Fe}$ habit planes, and are surrounded by a tetragonally distorted ferrite matrix. As a result cubic and tetragonal ferrite reflections can be discerned in both X-ray diffraction and selected area electron diffraction patterns.
3. The lattice parameter of the mixed $Ti_{1-x}Cr_xN$ nitride increases with increasing Ti/Cr atomic ratio. Consequently the misfit-strain field is most pronounced for the highest relative Ti content of the alloy, which corresponds with a microhardness increasing with increasing Ti/Cr atomic ratio.
4. The amount of excess nitrogen dissolved in the ferrite matrix, $[N]_{strain}$, increases with increasing Ti/Cr atomic ratio as a consequence of a tensile hydrostatic component of misfit stress increasing with increasing Ti/Cr atomic ratio.
5. The amount of excess nitrogen adsorbed at the nitride-platelet faces, $[N]_{interface}$, increases with increasing Ti/Cr atomic ratio because (i) Ti has a much larger affinity for N than Cr and (ii) the relative amount of interfacial (nitride/matrix) area increases with increasing Ti/Cr atomic ratio.

Chapter 6

Summary

In this thesis, the precipitation of alloying element nitrides upon gaseous nitriding of ferritic iron-based binary (Fe-Al and Fe-Si) and ternary (Fe-Cr-Ti) alloys has been investigated. Additionally, the role of substitutionally dissolved Al on the nucleation and growth of iron nitride, γ' -Fe₄N, has been investigated. The major outcomes of this thesis can be summarized as follows.

The precipitation of AlN in recrystallized and cold rolled specimens of Fe-4.65at.%Al alloy was investigated upon nitriding in ammonia-hydrogen gas mixtures (**chapter 2**). For the first time, the peculiar phenomenon of the emergence and disappearance of a high density of microcracks in the nitrided zone (Fig. 6.1) and the occurrence of AlN precipitate free zones around the ferrite grain boundaries was observed (Fig. 6.2). Due to the large volume misfit between the thermodynamically stable hexagonal (wurtzite type) AlN and the ferrite matrix, its precipitation in recrystallized ferrite is difficult. Hence, a competition between the precipitation of nitrogen gas (dissociation of nitrogen supersaturated ferrite into pure ferrite and nitrogen gas) at the grain boundaries and the precipitation of hexagonal (wurtzite-type) AlN occurs. This leads to the emergence of microcracks along the grain boundaries (via the coalescence of pores filled with nitrogen gas) and the formation of AlN precipitate free zones near the grain boundaries. Upon continued nitriding the initially partially nitrided grains become fully nitrided and the microcracks disappear. Such a phenomenon cannot occur in cold rolled specimens where relatively easy precipitation of metastable cubic (NaCl-type) AlN, on dislocations, inhibits the association of dissolved nitrogen atoms to molecular nitrogen gas.

The influence of substitutionally dissolved Al in ferritic Fe-4.75at.%Al alloy on the nucleation and growth of γ' iron nitride was investigated upon nitriding in ammonia-hydrogen gas mixtures (**chapter 3**). As compared to the nitriding of pure ferrite (α -Fe), where a layer of γ' develops at the surface, upon nitriding ferritic Fe-4.75at.%Al an unusual morphology of γ' plates develops at the surface, which plates deeply penetrate the substrate (Fig. 6.3). In the diffusion zone, nanosized precipitates of γ' and of metastable, cubic (NaCl-type) AlN occur, having, with the ferrite matrix, a Nishiyama – Wassermann orientation relationship and a Bain orientation relationship, respectively. The γ' plates contain a high density of stacking faults and fine ϵ iron nitride (Fe₂N_{1-z}) precipitates, although the formation of ϵ iron nitride is not expected for the

employed nitriding parameters. On the basis of dedicated nitriding experiments it could be shown that the unusual microstructural development is a consequence of the negligible solubility of Al in γ' and the obstructed precipitation of the thermodynamically stable, hexagonal (wurtzite-type) AlN in ferrite.

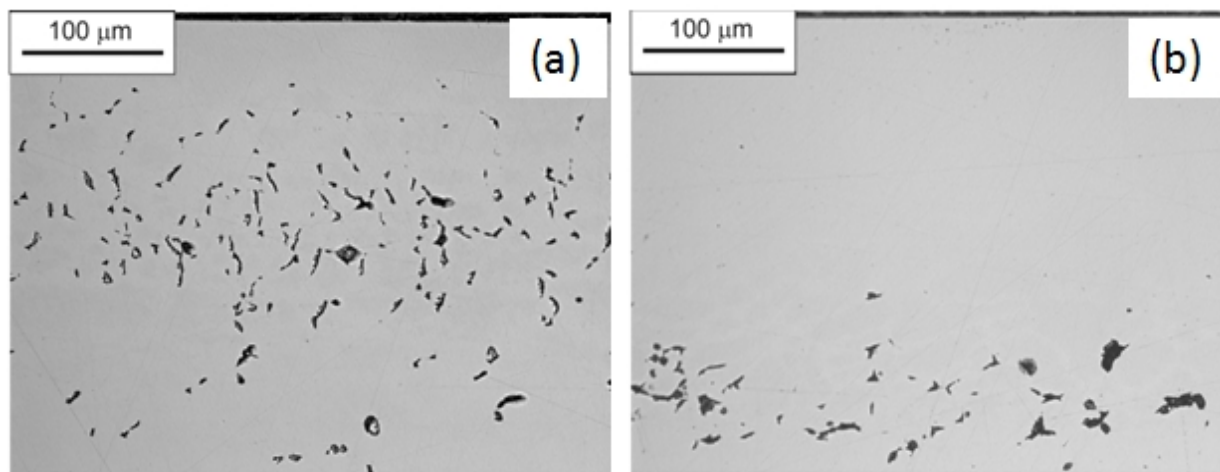


Fig. 6.1: Light optical micrographs of the unetched cross-section of the Fe-4.65at.%Al alloy specimens nitrided (550°C , $r_{\text{N}} = 0.104 \text{ atm}^{-1/2}$) for (a) 12 h and (b) (12 + 24) h (same specimen). Microcracks formed after 12 h of nitriding have disappeared after 24 h further nitriding.

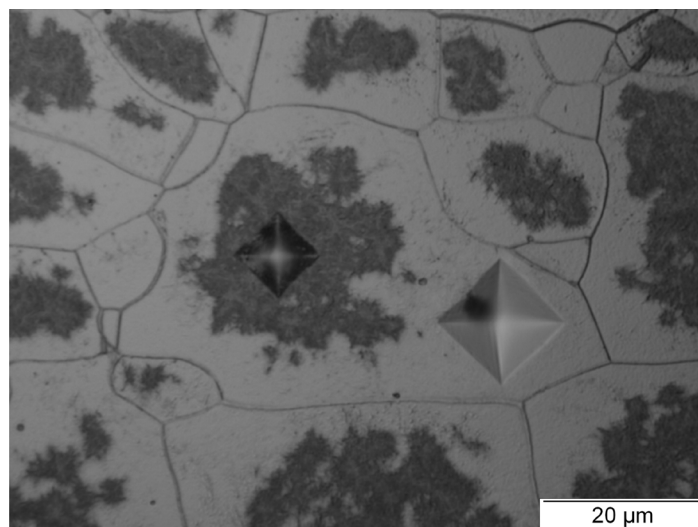


Fig. 6.2: Light optical micrograph showing two Vickers micro-hardness indentations in one grain of a Fe-4.65at.%Al specimen nitrided (550°C , $r_{\text{N}} = 0.104 \text{ atm}^{-1/2}$) for 12 h: the dark region (with precipitates) at centre of the grain is much harder than the white (precipitate free) region near to grain boundaries.

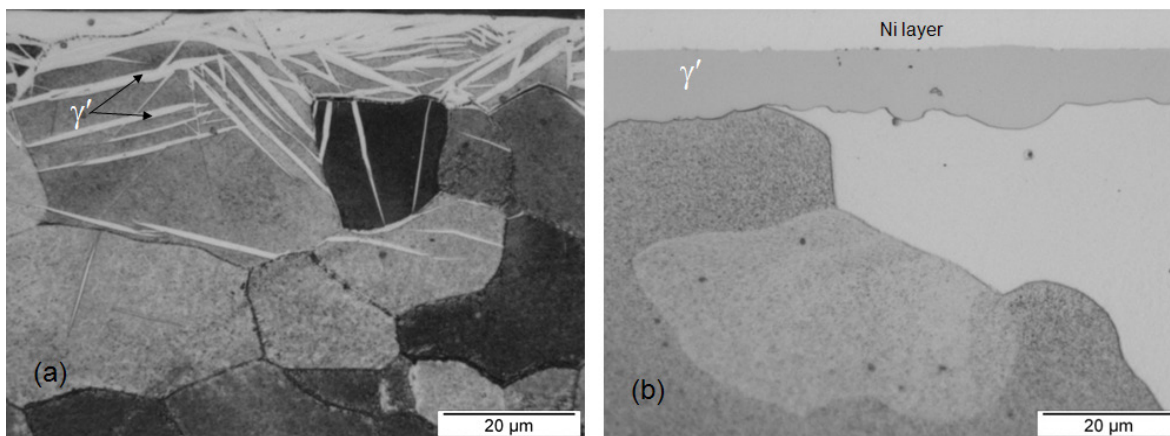


Fig. 6.3: Light optical micrographs of the cross-section of nitrided (550°C , 20 h, $r_N = 0.82 \text{ atm}^{-1/2}$) specimens. (a) Fe-4.75at.%Al alloy specimen with an unusual plate-type morphology of γ' precipitates; (b) Pure α -Fe specimen with a closed layer-type γ' formation.

Silicon-nitride precipitation in ferritic Fe-2at.%Si alloy was investigated upon nitriding in ammonia-hydrogen gas mixtures (**chapter 4**). Surprisingly, an ideally weak nitriding behaviour occurs upon nitriding *thick* (1 mm) recrystallised Fe-2at.%Si alloy specimens. This unexpected phenomenon can be attributed to the onset of silicon-nitride precipitation only after a certain degree of nitrogen supersaturation has been established *at all depths* in the specimen. Silicon-nitride precipitates form inside the ferrite grains and also along the grain boundaries. The precipitates are amorphous (Fig. 6.4) and have a stoichiometry of Si_3N_4 . The amorphous nature of the tiny precipitates has a thermodynamic origin. The nitride precipitation occurs very slowly due to a very large volume misfit of the nitride with the matrix. An anomalous non-monotonous hardness change occurs with increasing nitriding time (Fig. 6.5), which was ascribed to the initially fully elastic accommodation of precipitate/matrix misfit. The nitrogen-uptake rate increases upon continued nitriding as the result of “self-catalysis” (Fig. 6.5). It has been suggested that the precipitation of amorphous silicon-nitride as bands along the grain boundaries can be applied in practice to inhibit grain growth in the production of grain-oriented electrical steel.

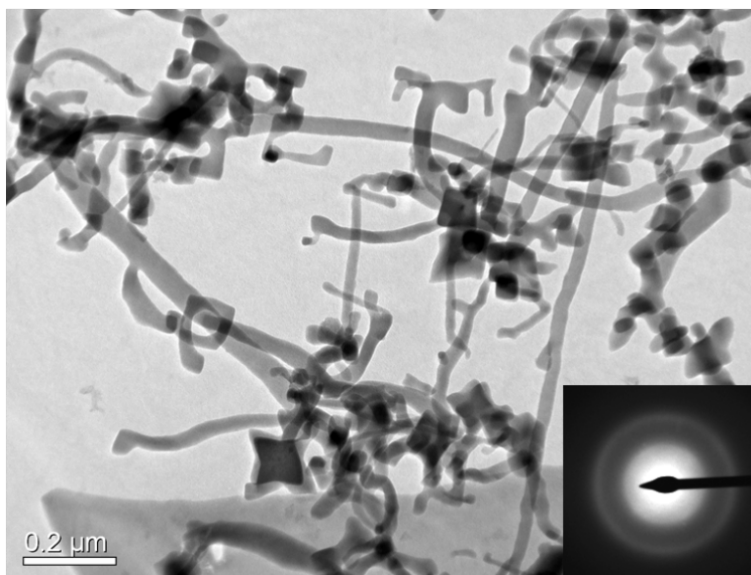


Fig. 6.4: TEM BF image and the corresponding SADP recorded from a 130 h nitrided Fe-2at.%Si specimen prepared by electro-jet polishing. Silicon-nitride precipitates became isolated from the matrix due to selective dissolution of the ferrite matrix. SADP from such isolated particles shows only diffuse intensity rings compatible with an amorphous nature of the silicon-nitride.

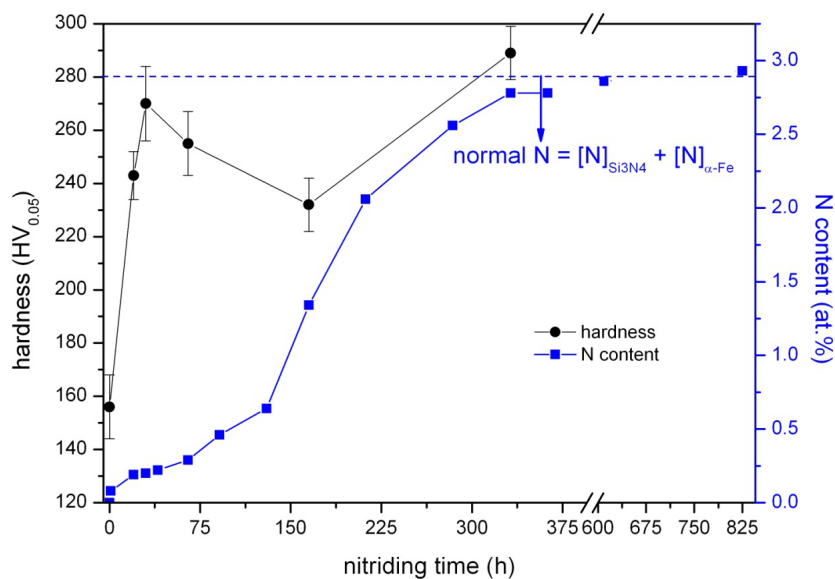


Fig. 6.5: Hardness and nitrogen content of the recrystallised Fe-2at.%Si alloy specimens as a function of nitriding time (580°C , $r_{\text{N}} = 0.104 \text{ atm}^{-1/2}$): a non-monotonous hardness change and an increase in nitrogen uptake rate occur with increase in nitriding time.

The microstructure of the nitrated zone of Fe-Ti-Cr alloys, containing a total of 0.3 at.% (Ti + Cr) alloying elements, with varying Ti/Cr atomic ratio was investigated (**chapter 5**). The thermodynamically stable TiN and CrN nitrides do not precipitate upon nitriding. Instead, ultrafine, metastable, mixed $Ti_{1-x}Cr_xN$ nitride precipitates develop in the nitrated zone: the precipitates are of platelet morphology (length ≤ 30 nm and thickness ≤ 3 nm) and of cubic (NaCl-type) crystal-structure. The misfit strain around the nitride platelets in the ferrite matrix increases with increasing Ti/Cr atomic ratio. As a consequence, most pronouncedly for the highest Ti/Cr atomic ratio, a tetragonally distorted ferrite matrix surrounds the precipitates. The amount of nitrogen taken up was determined quantitatively by measuring so-called nitrogen-absorption isotherms. It follows that the amount of so-called excess nitrogen dissolved in the matrix and adsorbed at the nitride-platelet faces increases distinctly with increasing Ti/Cr atomic ratio (Fig. 6.6). The results were discussed in terms of the dependence of misfit strain on the Ti/Cr atomic ratio and the higher chemical affinity of Ti for N than of Cr for N.

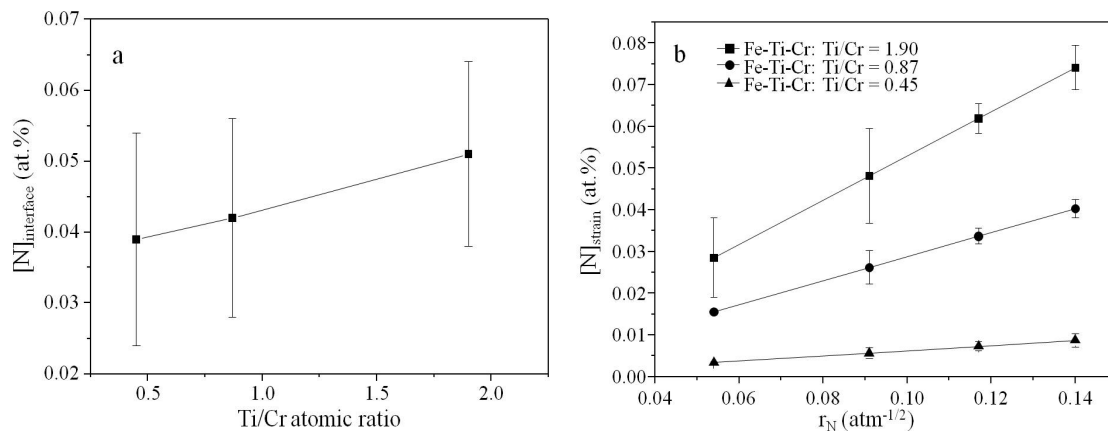


Fig. 6.6: Contributions to the excess nitrogen uptake during nitriding of ternary Fe-Ti-Cr alloys. (a) excess nitrogen adsorbed at the nitride precipitates/ferrite matrix interface, $[N]_{interface}$ (b) excess nitrogen dissolved interstitially, due to misfit strain fields, in the ferrite matrix, $[N]_{strain}$.

Chapter 7

Zusammenfassung in deutscher Sprache

In der vorliegenden Arbeit wurden die beim Gasnitrieren von ferritischen binären (Fe-Al und Fe-Si) und ternären (Fe-Cr-Ti) Eisenlegierungen entstehenden Nitride der jeweiligen Legierungselemente untersucht. Zusätzlich wurde der Einfluss von substitutionell gelöstem Al auf die Keimbildung und das Wachstum von Eisennitrid, γ' -Fe₄N, näher betrachtet. Die wichtigsten Ergebnisse dieser Arbeit können wie folgt zusammengefasst werden.

Die Ausscheidung von AlN in kalt gewalzten und rekristallisierten Proben einer Fe-4.65at.%Al Legierung beim Nitrieren in einer Ammoniak-Wasserstoff Gasatmosphäre wurde untersucht (**Kapitel 2**). Zum ersten Mal wurde das eigenartige Phänomen des Entstehens und des Verschwindens einer hohen Zahl von Mikrorissen in der Nitrierzone (Fig. 6.1), sowie die Bildung einer ausscheidungsfreien Zone entlang der Korngrenzen beobachtet (Fig. 6.2). Aufgrund der Volumen-Fehlpassung zwischen der thermodynamisch stabilen, hexagonalen (Wurtzit-Typ) AlN-Modifikation und der ferritischen Matrix, ist deren Ausscheidung in rekristallisiertem Ferrit schwierig. Die Folge ist ein Wettbewerb zwischen der Abscheidung von gasförmigem Stickstoff (Dissoziation von Stickstoff übersättigtem Ferrit in reinen Ferrit und Stickstoffgas) an den Korngrenzen und der Ausscheidung von hexagonalem (Wurtzit-Typ) AlN. Dies führt zur Entstehung von Mikrorissen entlang der Korngrenzen (via Koaleszenz von mit gasförmigem Stickstoff gefüllten Poren) und der Bildung einer von AlN-Ausscheidungen freien Zone nahe der Korngrenzen. Während des fortschreitenden Nitrierens werden die ursprünglich nur teilweise nitrierten Körner vollständig nitriert und die Mikrorisse verschwinden. Dieses Phänomen kann in kalt gewalzten Proben nicht auftreten, da hier an Versetzungen die vergleichsweise leichte Ausscheidung der metastabilen, kubischen (NaCl-Typ) AlN-Modifikation den Zusammenschluss von gelösten Stickstoffatomen zu molekularem Stickstoffgas verhindert.

Der Einfluss von substitutionell gelöstem Al in einer ferritischen Fe-4.65at.%Al Legierung auf die Keimbildung und das Wachstum von γ' -Eisennitrid beim Nitrieren in einer Ammoniak-Wasserstoff Gasatmosphäre wurde untersucht (**Kapitel 3**). Im Vergleich zu nitriertem Reineisen (α -Fe), wo sich eine γ' -Schicht an der Oberfläche bildet, entstehen beim Nitrieren einer ferritischen Fe-4.65at.%Al Legierung an der Oberfläche γ' -Platten mit einer ungewöhnlichen Morphologie, welche tief in das darunter liegende Material eindringen (Fig.

6.3). In der Diffusionszone treten nanoskalige γ' - und metastabile, kubische (NaCl-Typ) AlN-Ausscheidungen auf, welche mit der Ferritmatrix eine Nishiyama-Wassermann-, beziehungsweise eine Bain-Orientierungsbeziehung haben. Die γ' -Platten haben eine hohe Stapelfehlerdichte und enthalten feine ϵ -Eisennitrid ($\text{Fe}_2\text{N}_{1-z}$) Ausscheidungen, obwohl die Bildung von ϵ -Eisennitrid bei den angewandten Nitrierbedingungen nicht erwartet wird. Mit speziell abgestimmten Nitrierexperimenten konnte gezeigt werden, dass die ungewöhnliche Mikrostruktur eine Folge der vernachlässigbaren Al-Löslichkeit in γ' und der gehemmten Ausscheidung der thermodynamisch stabilen, hexagonalen (Wurtzit-Typ) AlN-Modifikation in Ferrit ist.

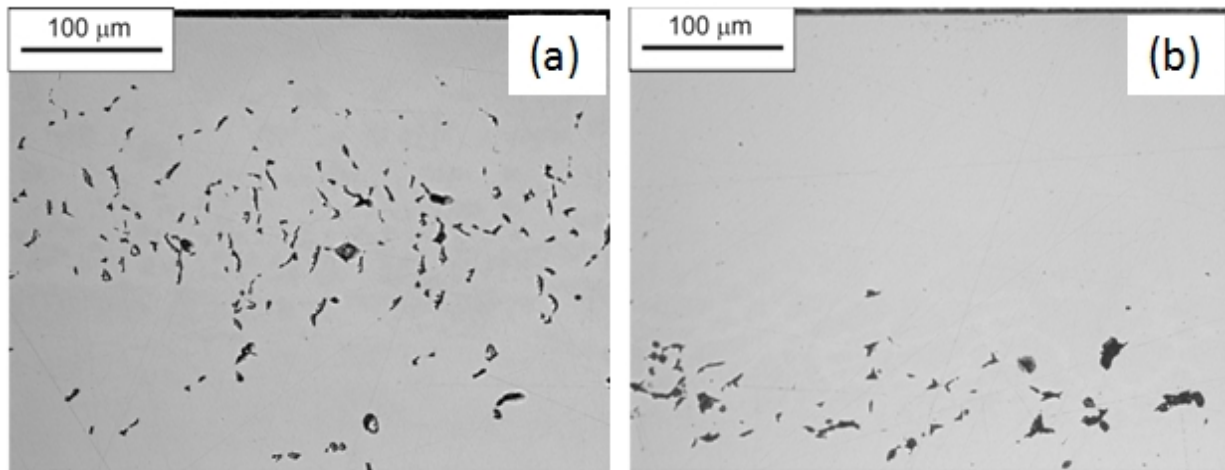


Fig. 6.1: Lichtmikroskopische Aufnahmen des ungeätzten Querschliffs einer Fe-4.65at.%Al Legierung nitriert (550°C , $r_N = 0.104 \text{ atm}^{-1/2}$) für a) 12 h und b) 12 h + 24 h (gleiche Probe). Die nach 12 h Nitrieren entstandenen Mikrorisse sind nach 24 h zusätzlichem Nitrieren verschwunden.

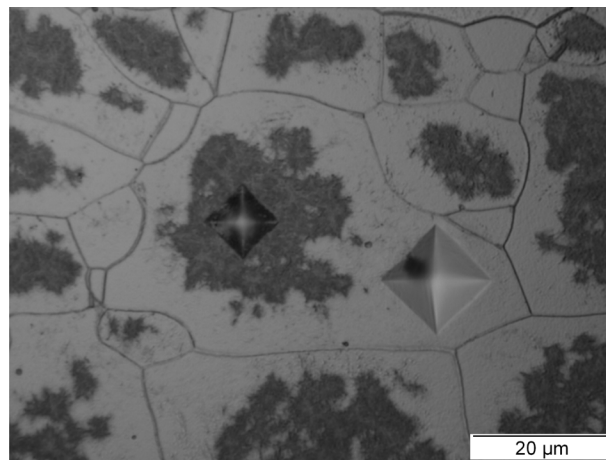


Fig. 6.2: Lichtmikroskopische Aufnahme von zwei Vickers-Mikrohärte-Eindrücken in einem Korn einer Fe-4.65at.%Al Legierung nitriert (550°C , $r_N = 0.104 \text{ atm}^{-1/2}$) für 12h: der dunkle Bereich (mit Ausscheidungen) im Korninneren ist viel härter als der weiße (ausscheidungsfreie) Bereich nahe der Korngrenzen.

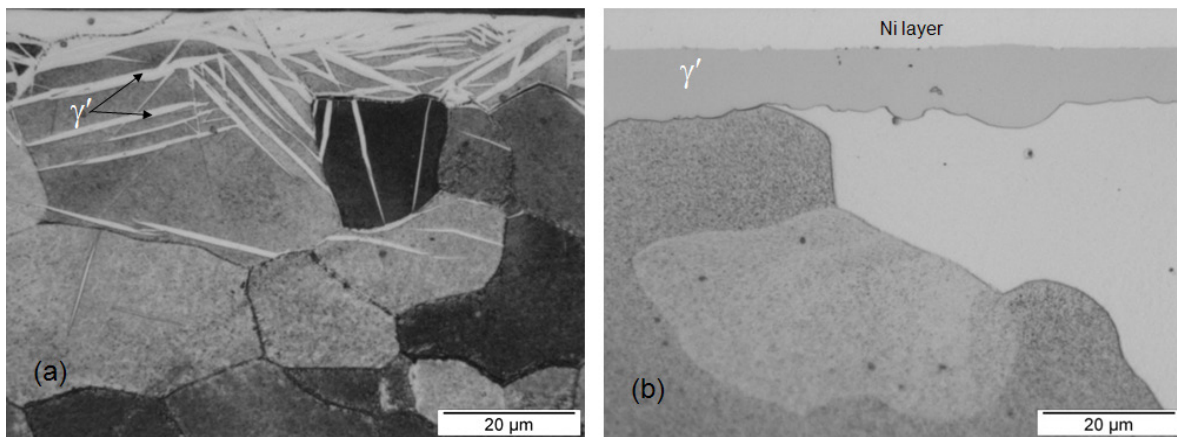


Fig. 6.3: Lichtmikroskopische Aufnahmen des Querschliffs von unter gleichen Bedingungen (550°C , 20 h, $r_{\text{N}} = 0.82 \text{ atm}^{-1/2}$) nitrierten Proben: (a) Fe-4.65at.%Al Legierung mit ungewöhnlichen plattenförmigen γ' -Ausscheidungen; (b) reine α -Fe Probe mit geschlossener, schichtförmiger γ' -Eisennitrid Bildung.

Die Ausscheidung von Siliziumnitrid in einer Fe-2at.%Si Legierung beim Nitrieren in einer Ammoniak-Wasserstoff Gasatmosphäre wurde untersucht (**Kapitel 4**). Überraschenderweise trat beim Nitrieren von (1 mm) dicken rekristallisierten Fe-2at.%Si Proben ein ideal schwaches Nitrierverhalten auf. Dieses unerwartete Verhalten kann dem Umstand zugeschrieben werden, dass die Ausscheidung von Siliziumnitrid erst beginnt, nachdem ein gewisser Grad an Stickstoffübersättigung über *die ganze Dicke* der Probe erreicht wurde. Siliziumnitrid-Ausscheidungen bilden sich innerhalb der Ferritkörner und entlang der Korngrenzen. Sie sind amorph (Fig. 6.4) und haben eine stöchiometrische Zusammensetzung wie Si_3N_4 . Die amorphe Natur der kleinen Ausscheidungen hat thermodynamische Gründe. Die Nitridbildung geschieht wegen der sehr großen Volumen-Fehlpassung zwischen Ausscheidung und Matrix sehr langsam. Es tritt ein ungewöhnlicher, nichtmonotoner Härteanstieg mit zunehmender Nitrierzeit auf (Fig. 6.5), welcher der anfänglich völlig elastischen Akkommodation der Ausscheidung/Matrix-Fehlpassung zugeschrieben wird. Die Stickstoffaufnahme nimmt mit fortschreitendem Nitrieren als Folge einer „self-catalysis“ (Fig. 6.5) zu. Es wurde darauf hingewiesen, dass die Ausscheidung von amorphem Siliziumnitrid als Belag entlang der Korngrenzen in der Praxis angewandt werden kann, um Kornwachstum bei der Produktion von kornorientiertem Elektrostahl zu verhindern.

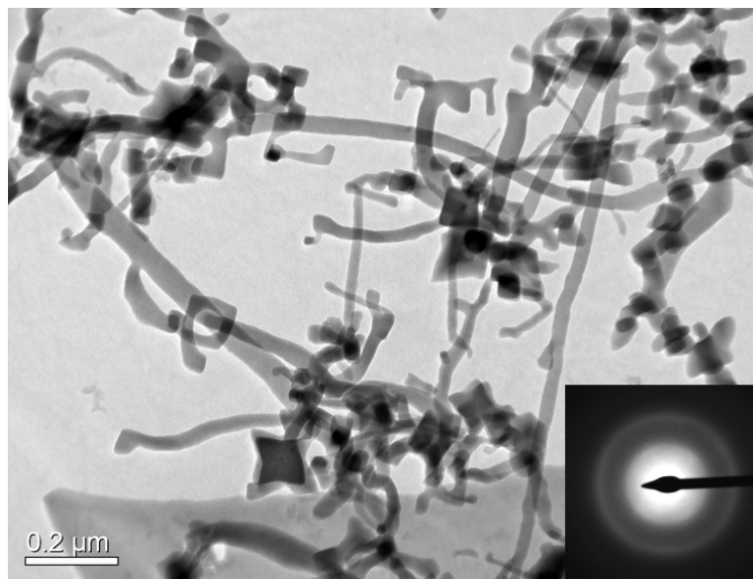


Fig. 6.4: TEM-Hellfeldabbildung einer 130 h nitrierten Fe-2at.%Si Probe, die durch elektrolytisches Polieren hergestellt wurde. Sie zeigt isolierte Siliziumnitrid-Ausscheidungen, welche nach der selektiven Auflösung der ferritischen Matrix übrig geblieben sind. Das Feinbereichsbeugungsbild eines isolierten Teilchens zeigt nur diffuse Intensitätsringe, in Übereinstimmung mit dem amorphen Zustand des Siliziumnitrids.

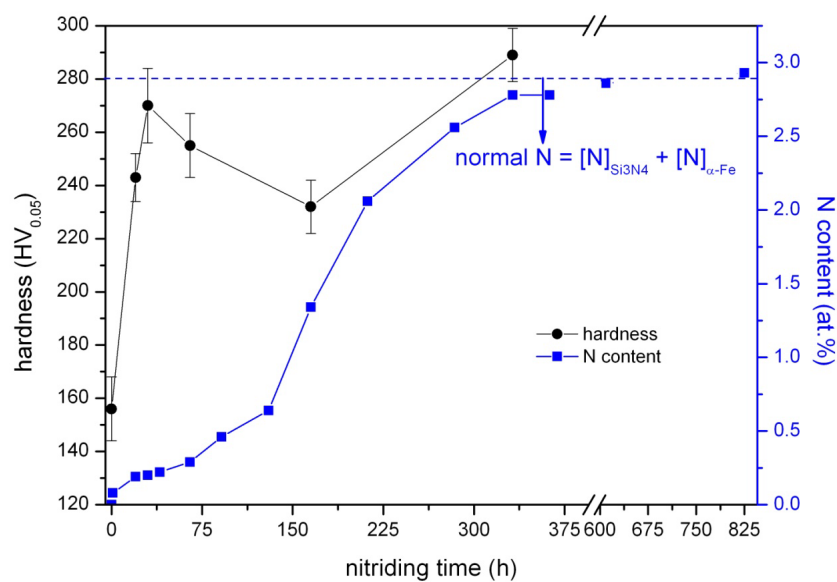


Fig. 6.5: Härte und Stickstoffgehalt von rekristallisierten Fe-2at.%Si Proben als Funktion der Nitrierzeit (580°C, $r_N = 0.104 \text{ atm}^{-1/2}$). Es tritt ein nichtmonotoner Härteverlauf und eine Zunahme der Stickstoffaufnahme mit zunehmender Nitrierzeit auf.

Das Gefüge der Nitrierzone von Fe-Ti-Cr Legierungen wurde untersucht, welche einen konstanten Legierungselementgehalt (Ti+Cr) von 0.3 at.% enthielten, jedoch mit unterschiedlichen Ti/Cr Verhältnissen (**Kapitel 5**). Die thermodynamisch stabilen TiN- und CrN-Nitride wurden beim Nitrieren nicht ausgeschieden. Stattdessen entwickelten sich in der Nitrierzone ultrafeine, metastabile $Ti_{1-x}Cr_xN$ Mischnitride mit plättchenförmiger Morphologie (Länge ≤ 30 nm, Dicke ≤ 3 nm) und kubischer (NaCl-Typ) Kristallstruktur. Die durch die Fehlpassung der Nitridplättchen hervorgerufenen Spannungen in der ferritischen Matrix nehmen mit zunehmendem Ti/Cr Verhältnis zu. Als Konsequenz entsteht, insbesondere für das größte Ti/Cr Verhältnis, eine tetragonal verzerrte Ferritmatrix um die Ausscheidungen. Die Stickstoffaufnahme wurde quantitativ bestimmt indem so genannte Stickstoff-Absorptions-Isothermen aufgenommen wurden. Es zeigte sich, dass der Anteil zum so genannten Stickstoffüberschuss, welcher in der Matrix gelöst ist und jener, der an Nitridplättchenoberfläche absorbiert ist, mit größer werdendem Ti/Cr Verhältnis deutlich zunimmt (Fig. 6.6). Die Ergebnisse wurden diskutiert in Bezug auf die Abhängigkeit der Fehlpassung vom Ti/Cr Verhältnis und der größeren chemischen Affinität von Ti zu N gegenüber Cr zu N.

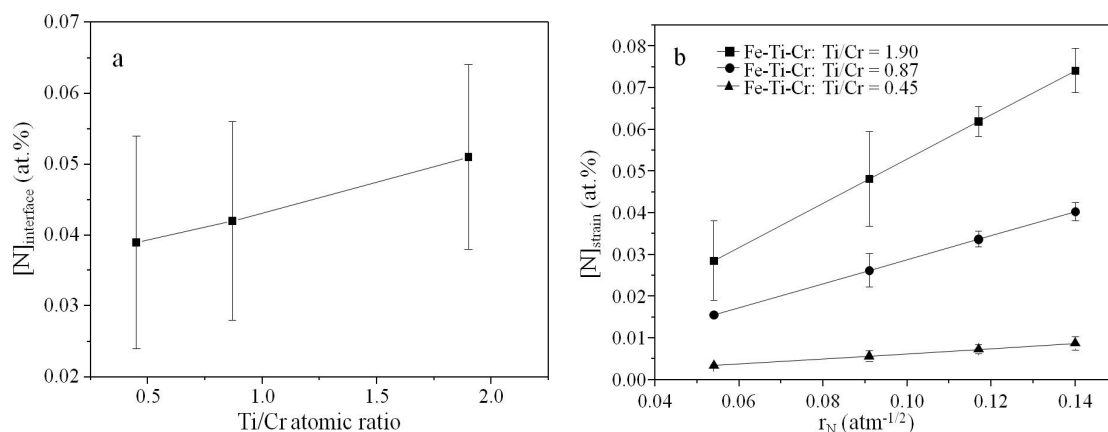


Fig. 6.6: Beiträge zur Stickstoffüberschussaufnahme während des Nitrierens von ternären Fe-Ti-Cr Legierungen: (a) Stickstoffüberschussanteil durch Absorption an der Nitridausscheidung/Ferritmatrix Grenzfläche, $[N]_{\text{interface}}$; (b) interstitiell gelöster Stickstoffüberschussanteil als Folge der Fehlpassungsspannungen in der Ferritmatrix, $[N]_{\text{strain}}$

References

- [1] M.A.J. Somers and E.J. Mittemeijer, *Metall. Mater. Trans. A* 26 (1995) p. 57.
- [2] H.C.F. Rozendaal, E.J. Mittemeijer, P.F. Colijn and P.J. van der Schaaf, *Metall. Trans. A* 14 (1983) p. 395.
- [3] M.A.J. Somers, B.J. Kooi, W.G. Sloof and E.J. Mittemeijer, *Surf. Inter. Analys.* 19 (1992) p. 633.
- [4] J. Dhaen, C. Quaeyhaegens, G. Knuyt, M. Dolieslaeger and L.M. Stals, *Surf. Coat. Tech.* 74-75 (1995) p. 405.
- [5] S.S. Hosmani, R.E. Schacherl, L. Litynska-Dobrzynska and E.J. Mittemeijer, *Phil. Mag.* 88 (2008) p. 2411.
- [6] S.S. Hosmani, R.E. Schacherl and E.J. Mittemeijer, *Acta Mater.* 53 (2005) p. 2069.
- [7] N.E.V. Diaz, S.S. Hosmani, R.E. Schacherl and E.J. Mittemeijer, *Acta Mater.* 56 (2008) p. 4137.
- [8] A.R. Clauss, E. Bischoff, S.S. Hosmani, R.E. Schacherl and E.J. Mittemeijer, *Metall. Mater. Trans. A* 40 (2009) p. 1923.
- [9] A.R. Clauss, E. Bischoff, R.E. Schacherl and E.J. Mittemeijer, *Phil. Mag.* 89 (2009) p. 565.
- [10] K.S. Jung, R.E. Schacherl, E. Bischoff and E.J. Mittemeijer, *Surf. Coat. Tech.* 204 (2010) p. 1942.
- [11] E.J. Mittemeijer and J.T. Slycke, *Surf. Eng.* 12 (1996) p. 152.
- [12] E.J. Mittemeijer and M.A.J. Somers, *Surf. Eng.* 13 (1997) p. 483.
- [13] P.B. Friehling, F.W. Poulsen and M.A.J. Somers, *Z. Metallkd.* 92 (2001) p. 589.
- [14] E. Lehrer, *Z. Elektrochem.* 36 (1930) p. 383.
- [15] R. Hoffmann, *Härterei-Tech. Mitt.* 51 (1996) p. 5.
- [16] D. Liedtke, U. Baudis, J. Boßlet, U. Huchel, H. Klümper-Westkamp, W. Lerche and H.-J. Spies (eds.), *Wärmebehandlung von Eisenwerkstoffen – Nitrieren und Nitrocarburieren*, Expert-Verlag, Renningen-Malmsheim, 2006.
- [17] M.H. Biglari, C.M. Brakman and E.J. Mittemeijer, *Phil. Mag. A* 72 (1995) p. 1281.
- [18] E.J. Mittemeijer, M.H. Biglari, A.J. Bottger, N.M. van der Pers, W.G. Sloof and F.D. Tichelaar, *Scr. Mater.* 41 (1999) p. 625.
- [19] L.P.H. Jeurgens, Z.M. Wang and E.J. Mittemeijer, *Int. J. Mater. Res.* 100 (2009) p. 1281.
- [20] R.M. Lankreijer, M.A.J. Somers and E.J. Mittemeijer. *Kinetics of nitride precipitation in Fe-Al and Fe-Si alloys on nitriding*. In: *Proc. Inter. Conf. on high nitrogen steels*, J. Foct, A. Hendry (eds.), The institute of metals, London, Lille, France, 1989, p.108.
- [21] M.H. Biglari, C.M. Brakman, M.A.J. Somers, W.G. Sloof and E.J. Mittemeijer, *Z. Metallkd.* 84 (1993) p. 124.
- [22] JANAF Thermochemical Tables, third edition, 1985.
- [23] Springer, the Landolt-Börnstein database, 1999.
- [24] M.A.J. Somers, R.M. Lankreijer and E.J. Mittemeijer, *Phil. Mag. A* 59 (1989) p. 353.
- [25] R.E. Schacherl, P.C.J. Graat and E.J. Mittemeijer, *Metall. Mater. Trans. A* 35 (2004) p. 3387.
- [26] H.H. Podgurski, R.A. Oriani, F.N. Davis, J.C.M. Li and Y.T. Chou, *Trans. AIME.* 245 (1969) p. 1603.
- [27] H.H. Podgurski and H.E. Knechtel, *Trans. AIME.* 245 (1969) p. 1595.
- [28] H.H. Podgurski and F.N. Davis, *Acta Metall.* 29 (1981) p. 1.
- [29] S.S. Hosmani, R.E. Schacherl and E.J. Mittemeijer, *HTM J. Heat Treatm. Mat.* 63 (2008) p. 139.
- [30] S.S. Hosmani, R.E. Schacherl and E.J. Mittemeijer, *Int. J. Mater. Res.* 97 (2006) p. 1545.

- [31] P.C. van Wiggan, H.C.F. Rozendaal and E.J. Mittemeijer, *J. Mater. Sci.* 20 (1985) p. 4561.
- [32] S. Jegou, L. Barrallier and R. Kubler, *Acta Mater.* 58 (2010) p. 2666.
- [33] H. Atmani and O. Thoumire, *Bull. Mater. Sci.* 25 (2002) p. 219.
- [34] W. Roberts, K.H. Jack and P. Grieveson, *J. Iron Steel. Inst.* 210 (1972) p. 931.
- [35] P.M. Unterweiser and A.G. Gray (eds.), *Source Book on Nitriding*, ASM, Metals Park, OH, 1977.
- [36] M.H. Biglari, C.M. Brakman, E.J. Mittemeijer and S. van der Zwaag, *Phil. Mag. A* 72 (1995) p. 931.
- [37] J.S. Steenaert, M.H. Biglari, C.M. Brakman, E.J. Mittemeijer and S. van der Zwaag, *Z. Metallkd.* 86 (1995) p. 700.
- [38] M.H. Biglari, C.M. Brakman, E.J. Mittemeijer and S. van der Zwaag, *Metall. Mater. Trans. A* 26 (1995) p. 765.
- [39] W.B. Pearson, *A handbook of lattice spacings and structures of metals and alloys*, Pergamon Press, London, 1968.
- [40] M. Sennour and C. Esnouf, *Acta Mater.* 51 (2003) p. 943.
- [41] JCPDS - International Center of Diffraction Data, PCPDFWIN Ver.202, 1999.
- [42] E.J. Mittemeijer, *J. Metals* 37 (1985) p. 16.
- [43] E.J. Mittemeijer and J. Grosch (eds.), *AWT-Tagung Nitrieren und Nitrocarburieren, Arbeitsgemeinschaft Wärmebehandlung und Werkstofftechnik e.V.*, AWT-Bremen, Wiesbaden, 1991.
- [44] C.H. Knerr, T.C. Rose and J.H. Filkowski. *Gas nitriding of steels* In: ASM Handbook, Heat Treating, vol. 4, J. R. Davis, G. M. Davidson, S. R. Lampman, T. B. Zorc, J. L. Daquila, A. W. Ronke, K. L. Henninger, R. C. Uhl (eds.), ASM International, Metals Park, OH, 1991, p.387.
- [45] F. Hoffmann and H. Klümper-Westkamp (eds.), *European Conference on Heat Treatment 2010 - Nitriding and Nitrocarburising*, AWT-Bremen, Aachen, 2010.
- [46] L. Torchane, P. Bilger, J. Dulcy and M. Gantois, *Metall. Mater. Trans. A* 27 (1996) p. 1823.
- [47] M.A.J. Somers, P.F. Colijn, W.G. Sloof and E.J. Mittemeijer, *Z. Metallkd.* 81 (1990) p. 33.
- [48] N. Geerlofs, C.M. Brakman, P.F. Colijn and S. van der Zwaag, *Mater. Sci. Forum* 163-165 (1994) p. 273.
- [49] S. Meka, S.S. Hosmani, A.R. Clauss and E.J. Mittemeijer, *Int. J. Mater. Res.* 99 (2008) p. 808.
- [50] Y.M. Lakhtin, N.V. Silina and V.A. Fedchun, *Met. Sci. Heat. Treat.* 19 (1977) p. 3.
- [51] V.A. Fedchun and N.V. Silina, *Met. Sci. Heat. Treat.* 30 (1988) p. 890.
- [52] R. Chatterjee-Fischer, R. Bodenhausen, F.-W. Eysell, R. Hoffmann, D. Liedtke, H. Mallener, W. Rembges, A. Schreiner and G. Welker (eds.), *Wärmebehandlung von Eisenwerkstoffen*, Expert-Verlag, Renningen-Malmsheim, 1995.
- [53] E.J. Mittemeijer, A.B.P. Vogels and P.J. van der Schaaf, *Scr. Metall.* 14 (1980) p. 411.
- [54] P. Ferguson and K.H. Jack, *Proc. Heat Treatment '81*. The Metals Society, London. (1982) p. 158.
- [55] T. Liapina, A. Leineweber, E.J. Mittemeijer and W. Kockelmann, *Acta Mater.* 52 (2004) p. 173.
- [56] J.L. Pouchou and F. Pichoir, *Rech. Aerosp.* (1984) p. 167.
- [57] S.S. Hosmani, R.E. Schacherl and E.J. Mittemeijer, *J. Mater. Sci.* 44 (2009) p. 520.
- [58] H. Miyamura, J. Takada, H. Kuwahara and S. Kikuchi, *J. Mater. Sci.* 21 (1986) p. 2514.

- [59] J. Takada, Y. Oizumi, H. Miyamura, H. Kuwahara and S. Kikuchi, *Oxid. Met.* 26 (1986) p. 19.
- [60] Z. Nishiyama, *Science Reports of the Tohoku Imperial University* 23 (1934) p. 637.
- [61] G. Wassermann, *Arch. Eisenhütte* 6 (1933) p. 347.
- [62] X.C. Xiong, A. Redjaimia and M. Goune, *J. Mater. Sci.* 44 (2009) p. 632.
- [63] U. Dahmen, P. Ferguson and K.H. Westmacott, *Acta Metall.* 35 (1987) p. 1037.
- [64] E.C. Bain, *Trans. AIME.* 70 (1924) p. 25.
- [65] X.L. Xu, L. Wang, Z.W. Yu and Z.K. Hei, *Metall. Mater. Trans. A* 27 (1996) p. 1347.
- [66] K. Sumiyama, H. Onodera, K. Suzuki, S. Ono, K.J. Kim, K. Gemma and Y. Nishi, *J. Alloys Comp.* 282 (1999) p. 158.
- [67] E.J. Mittemeijer and U. Welzel, *Z. Kristallogr.* 223 (2008) p. 552.
- [68] A. Leineweber and E.J. Mittemeijer, *J. Appl. Crystallogr.* 43 (2010) p. 981.
- [69] L. Velterop, R. Delhez, T.H. de Keijser, E.J. Mittemeijer and D. Reefman, *J. Appl. Crystallogr.* 33 (2000) p. 296.
- [70] J.T. Norton, *Trans. AIME.* 113 (1934) p. 262.
- [71] H.H. Stadelmaier and T.S. Yun, *Z. Metallkd.* 52 (1961) p. 477.
- [72] A. Houben, J. Burghaus and R. Dronskowski, *Chem. Mater.* 21 (2009) p. 4332.
- [73] A. Houben, J. Burghaus and R. Dronskowski, *Chem. Mater.* DOI:10.1021/cm201863y.
- [74] E.J. Mittemeijer, *Fundamentals of Materials Science*, Springer-Verlag, Berlin, Heidelberg, 2010.
- [75] H.K.D.H. Bhadeshia and J.W. Christian, *Metall. Trans. A* 21 (1990) p. 767.
- [76] E. Kozeschnik and H.K.D.H. Bhadeshia, *Mater. Sci. Technol.* 24 (2008) p. 343.
- [77] S. Meka, R.E. Schacherl, E. Bischoff and E.J. Mittemeijer, *HTM J. Heat Treatm. Mat.* 66 (2011) p. 103.
- [78] H. Selg, H. Zhong, E. Bischoff, R.E. Schacherl and E.J. Mittemeijer. to be published.
- [79] G. Miyamoto, A. Yonemoto, Y. Tanaka, T. Furuhashi and T. Maki, *Acta Mater.* 54 (2006) p. 4771.
- [80] J.D. Kamminga and G.C.A.M. Janssen, *Surf. Coat. Tech.* 200 (2005) p. 909.
- [81] K.S. Jung, R.E. Schacherl, E. Bischoff and E.J. Mittemeijer, *Phil. Mag.* 91 (2011) p. 2382.
- [82] H.K.D.H. Bhadeshia, *Bainite in Steels*, Institute of Materials, London, 2001.
- [83] C.C. Liao and C.K. Hou, *J. Magn. Magn. Mater.* 322 (2010) p. 434.
- [84] G.R. Booker and J. Norbury, *Nature* 184 (1959) p. 1311.
- [85] M. Seher, J. Bill, F. Aldinger and R. Riedel, *J. Cryst. Growth* 137 (1994) p. 452.
- [86] M.F. Ashby and G.C. Smith, *J. Inst. Met.* 91 (1963) p. 182.
- [87] S.L. Cundy and P.J. Grundy, *Phil. Mag.* 14 (1966) p. 1233.
- [88] D.H. Jack and K.H. Jack, *Mater. Sci. Eng.* 11 (1973) p. 1.
- [89] W.T.M. Straver, H.C.F. Rozendaal and E.J. Mittemeijer, *Metall. Trans. A* 15 (1984) p. 627.
- [90] J.D. Fast and M.B. Verrijp, *J. Iron Steel. Inst.* 176 (1954) p. 24.
- [91] H.J. Grabke, *Ber. Bunsenges. Phys. Chem.* 72 (1968) p. 533.
- [92] H.J. Grabke, *Ber. Bunsenges. Phys. Chem.* 72 (1968) p. 541.
- [93] J. Kunze and P.O.K. Friedrich, *J. Mater. Sci. Lett.* 5 (1986) p. 815.
- [94] D.A. Leak, W.R. Thomas and G.M. Leak, *Acta Metall.* 3 (1955) p. 501.
- [95] M. Nikolussi, A. Leineweber and E.J. Mittemeijer, *Phil. Mag.* 90 (2010) p. 1105.
- [96] N.P. Goss. US patent No. 1965559. 1934.
- [97] K. Gunther, G. Abbruzzese, S. Fortunati and G. Ligi, *Steel Res. Int.* 76 (2005) p. 413.
- [98] Z.S. Xia, Y.L. Kang and Q.L. Wang, *J. Magn. Magn. Mater.* 320 (2008) p. 3229.

- [99] N. Chen, S. Zaefferer, L. Lahn, K. Gunther and D. Raabe, *Acta Mater.* 51 (2003) p. 1755.
- [100] S. Lampmann (ed.) *Introduction to surface hardening of steel. ASM Handbook: Heat Treating* ASM international, Ohio, 1991.
- [101] M.A.J. Somers and E.J. Mittemeijer, *Mater. Sci. Forum* 102 (1992) p. 223.
- [102] P.M. Hekker, H.C.F. Rozendaal and E.J. Mittemeijer, *J. Mater. Sci.* 20 (1985) p. 718.
- [103] R.E. Schacherl, P.C.J. Graat and E.J. Mittemeijer, *Z. Metallkd.* 93 (2002) p. 468.
- [104] B. Mortimer, P. Grieveson and K.H. Jack, *Scand. J. Metall.* 1 (1972) p. 203.
- [105] S.S. Hosmani, R.E. Schacherl and E.J. Mittemeijer, *Mater. Sci. Technol.* 21 (2005) p. 113.
- [106] S.S. Hosmani, R.E. Schacherl and E.J. Mittemeijer, *J. Mater. Sci.* 43 (2008) p. 2618.
- [107] W.D. Welch and S.H. Carpenter Jr, *Acta Metall.* 21 (1973) p. 1169.
- [108] A. Krawitz, *Scr. Metall.* 11 (1977) p. 117.
- [109] S.S. Hosmani, R.E. Schacherl and E.J. Mittemeijer, *Acta Mater.* 54 (2006) p. 2783.
- [110] D.H. Kirkwood, O.E. Atasoy and S.R. Keown, *Metal Sci.* 8 (1974) p. 49.
- [111] D.S. Rickerby, S. Henderson, A. Hendry and K.H. Jack, *Acta Metall.* 34 (1986) p. 1687.
- [112] D.H. Jack, *Acta Metall.* 24 (1976) p. 137.
- [113] H. Hasegawai, A. Kimura and T. Suzuki, *J. Vac. Sci. Technol. B* 18 (2000) p. 1038.
- [114] S.M. Aouadi, J.A. Chladek, F. Namavar, N. Finnegan and S.L. Rohde, *J. Vac. Sci. Technol. B* 20 (2002) p. 1967.
- [115] M.A. Baker, T.P. Mollart, P.N. Gibson and W. Gissler, *J. Vac. Sci. Technol. A* 15 (1997) p. 284.
- [116] J. Vetter, H.J. Scholl and O. Knotek, *Surf. Coat. Tech.* 74-75 (1995) p. 286.
- [117] T. Suzuki, D. Huang and Y. Ikuhara, *Surf. Coat. Tech.* 107 (1998) p. 41.
- [118] V.A. Phillips and A.U. Seybolt, *Trans. AIME.* 242 (1968) p. 2415.
- [119] R. Hoffmann, E.J. Mittemeijer and M.A.J. Somers, *HTM J. Heat Treatm. Mat.* 51 (1996) p. 162.
- [120] R. Delhez and E.J. Mittemeijer, *J. Appl. Crystallogr.* 8 (1975) p. 609.
- [121] A. Armigliato, L. Dori, A. Garulli and P. Venturi, *J. Microsc. Spect. Elec.* 7 (1982) p. 593.
- [122] Y. Massiani, P. Gravier, L. Fedrizzi and F. Marchetti, *Thin Solid Films* 261 (1995) p. 202.
- [123] P. Hones, R. Sanjines and F. Levy, *Thin Solid Films* 332 (1998) p. 240.

List of Publications

1. S. Meka, S.S. Hosmani, A.R. Clauss and E.J. Mittemeijer. **The emergence and disappearance of a high density of microcracks in nitrated Fe-4.65at.%Al alloy** *International Journal of Materials Research*, Vol. 99, 2008, p 808-814 (Chapter 2 of this thesis).
2. S. Meka, E. Bischoff, R.E. Schacherl and E.J. Mittemeijer. **Unusual nucleation and growth of γ' iron nitride upon nitriding Fe-4.75at.%Al alloy** submitted to *Philosophical Magazine* (Chapter 3 of this thesis).
3. S. Meka, K.S. Jung, E. Bischoff and E.J. Mittemeijer. **Unusual precipitation of amorphous silicon nitride upon nitriding Fe-2at.%Si alloy** submitted to *Philosophical Magazine* (Chapter 4 of this thesis).
4. K.S. Jung, S. Meka, R.E. Schacherl, E. Bischoff and E.J. Mittemeijer. **Nitride formation and excess nitrogen uptake upon nitriding ferritic Fe-Ti-Cr alloys** submitted to *Metallurgical and Materials Transactions* (Chapter 5 of this thesis).
5. S. Meka, R.E. Schacherl, E. Bischoff and E.J. Mittemeijer. **Unusual microstructural development upon gaseous nitriding of Fe-4.65at% Al alloy** *Advanced Materials Research*, Vol. 89-91, 2010, p 371-376.
6. S. Meka, R.E. Schacherl, E. Bischoff and E.J. Mittemeijer. **Ideally weak nitriding kinetics during gaseous nitriding of Fe-2at.%Si alloy** *HTM Journal of Heat Treatment and Materials*, Vol. 66, 2011, p 103-108.

Acknowledgements

The work presented in this thesis has been performed at the Max Planck Institute for Intelligent Systems (formerly Max Planck Institute for Metals Research) and at the Institute for Materials Science, University of Stuttgart.

First of all, I would like to thank my thesis supervisor Prof. Dr. E.J. Mittemeijer for introducing me to this exciting field of nitriding and providing me the opportunity to work in his department. His commitment, guidance, encouragement and his immense knowledge on the subject, were a tremendous contribution for the successful completion of this thesis. I have very much benefitted from the regular scientific discussions with him and the writing of the status reports on the ongoing research activity, which have considerably enhanced my scientific knowledge and scientific writing.

I would like to thank my daily supervisors Dr. E. Bischoff and Dr. R.E. Schacherl for their continuous cooperation and encouragement. My special thanks to Dr. E. Bischoff for German translation of the summary.

I am grateful to all friends, present and former colleagues in the department Mittemeijer for their assistance and the friendly environment which made my stay in the department pleasant and joyful. I am very grateful for all support and technical assistance I experienced from the members of the institute. I would also like to thank all my friends outside the institute for a memorable stay in Stuttgart.

Everything which I have achieved in my life is solely because of the endless love and affection of my family. I am very grateful to each member of my family for staying with me all the time.

Curriculum Vitae

Personal Data

Name Sai Ramudu Meka
Date of birth 1st June 1979
Place of Birth Kuntoji, Gangavathi, Karnataka, India
Nationality Indian

Schooling

1985 - 1995 Karnataka Secondary Education Examination Board,
Karnataka, India
1995 - 1998 Department of Pre-University Education, Karnataka, India

Higher education

1998 – 2002 Bachelor of Engineering (Metallurgy)
National Institute of Technology, Karnataka (*formerly* Karnataka
Regional Engineering College), India
2004 – 2007 Master of Technology (Materials and Metallurgical Engineering)
Indian Institute of Technology, Kanpur, India

Dissertation

Aug. 2007 - Present Ph. D. at the Max Planck Institute for Intelligent Systems (*formerly*
Max Planck Institute for Metals Research) and
Institute for Materials Science, University of Stuttgart, Germany
Title of Dissertation:
*“Nitriding of iron-based binary and ternary alloys:
microstructural development during nitride precipitation”*

Professional experience

Sep. 2002 – Dec. 2004 Junior Manager
Jindal Vijayanagara Steels Ltd. (JVSL), Bellary, India

